BROADBAND ACOUSTICAL SCATTERING IN COASTAL ENVIRONMENTS: APPLICATION TO GELATINOUS ORGANISMS AND GAS MICROBUBBLES

by

Rachel E. Kahn

B.A., Scripps College, 2017

Submitted to the Department of Mechanical Engineering
in partial fulfillment of the requirements for the degree of

Doctor of Philosophy

at the

MASSACHUSETTS INSTITUTE OF TECHNOLOGY

and the

WOODS HOLE OCEANOGRAPHIC INSTITUTION

February 2024

Authored by: Rachel E. Kahn
Joint Program in Oceanography/Applied Ocean Science and Engineering
Massachusetts Institute of Technology and Woods Hole Oceanographic Institution
January 19, 2024

Certified by: Andone C. Lavery
Senior Scientist, Woods Hole Oceanographic Institution
Thesis Supervisor

Accepted by: Alexandra H. Techet
Professor of Mechanical Engineering, Massachusetts Institute of Technology
Chair, Joint Committee for Applied Ocean Science and Engineering

Nicolas Hadjiconstantinou
Professor of Mechanical Engineering, Massachusetts Institute of Technology
Chair, Department Committee on Graduate Theses

BROADBAND ACOUSTICAL SCATTERING IN COASTAL ENVIRONMENTS: APPLICATION TO GELATINOUS ORGANISMS AND GAS MICROBUBBLES

by

Rachel E. Kahn

Submitted to the Department of Mechanical Engineering on 19 January 2024,
in partial fulfillment of the requirements for the degree of Doctor of Philosophy

Abstract

Broadband acoustical technology revolutionized our ability to explore, monitor, and operate in the ocean. While strides have been made in numerous physical and biological applications, there remain many standing scientific questions well suited to broadband approaches. Physics-based sound scattering models allow us to interpret and draw quantitative observations from measurements. Such models have been developed and used to assess the biomass of many types of marine organisms of ecological significance, but we lack rigorous scattering models for gelatinous organisms despite their possibly accounting for a significant proportion of global marine biomass. Additionally, acoustical techniques for characterizing microbubble populations have been established for decades, yet little is known about the spectral characteristics of dense microbubble clouds associated with estuarine tidal fronts. These bubbles facilitate air-sea gas exchange and could interfere with acoustical operations in coastal environments; however, the density and size distribution of the bubbles must be known to assess their impacts. This dissertation addresses these deficiencies in our application of broadband techniques. In Chapter 2, a sound scattering model for gelatinous organisms is developed based on the Distorted Wave Born Approximation. The 3-D model is applied to a species of scyphomedusa and verified with laboratory measurements of broadband backscattering from live individuals. The model predicts backscattering levels and broad spectral behavior within <2 dB. In Chapter 3, a towable instrument is developed for measuring broadband excess attenuation from bubbles from which the size distribution is inferred. The instrument is tested under breaking waves in a laboratory wave tank and then used to characterize the bubble size distribution in the Connecticut River tidal ebb plume front. In Chapter 4, broadband backscattering measurements from the Connecticut River front are used to infer the associated bubble size distribution. Spatial trends in the bubble size distribution are examined within the context of frontal kinematics. An observed disparity between the bubble size distribution measured with excess attenuation and volume backscattering is hypothesized to arise from a sampling bias caused by bubbles concentrated in the upper water column.

Thesis supervisor: Andone C. Lavery
Title: Senior Scientist, Woods Hole Oceanographic Institution

Acknowledgements

The completion of this dissertation was made possible by many sources of support that kept me afloat during my time in the Joint Program. I would like to express my sincerest gratitude to the advisors, mentors, coaches, friends, and family who supported me, believed in me, and cheered me on along the way.

First, I would like to thank my advisor, Andone Lavery. She taught me so much not just about acoustics, but also about what it takes to be an extraordinary scientist. I am grateful for her willingness to invest in me and for her patience with me through the many challenges I faced as a graduate student. I would also like to thank the members of my thesis committee: Seth Zippel, John Leonard, and Chris Bassett. They reminded me to continually look at the bigger picture of why my research matters, and they pushed me to think critically and raise the bar on my data analyses while never wavering in their encouragement. In addition to serving on my thesis committee, Chris has been an invaluable mentor to me since my first year at WHOI. I cannot overstate my appreciation for his patience and willingness to help me, teach me, and provide thoughtful feedback on my work.

There are numerous people at WHOI who I had the pleasure of working with, who contributed directly and indirectly to this dissertation. I would like to thank the scientists, staff, students, and postdocs of the WHOI Ocean Acoustics and Signals Lab for giving me a sense of community at work. OASL meetings, coffee hours, and “on-site” Wednesdays were a highlight of days at the office. Tim Stanton taught me much of what I know about the physics of scattering from bounded objects, and his life advice was just as helpful as his technical advice. Bob Petitt made my instruments work and patiently taught me how to operate them, and I am grateful to have worked so closely with him over the years. Kaitlyn Tradd helped me build confidence in my mechanical engineering skills and was a role model and friend to me. Bob, Chris, and Annette Govindarajan were valuable collaborators on my thesis chapters, and Rocky Geyer contributed his expertise on estuaries, especially in the field. I thank WHOI Academic Programs Office for their support over the years. Kris Kipp went above and beyond to make me feel welcome in the JP office at MIT.

The staff and students at MIT Grad Hillel made me feel welcome and supported during my two years based in Cambridge and well into the COVID-19 pandemic, and I am grateful for the friends I made there. Also at MIT, I would like to thank Kelli Hendrickson, Jenny Wang, and the Mechanical Engineering Grad Student Coaching Program, which had a hugely positive impact on my graduate school experience and personal development. Over the years since I joined the program, Kelli has become an invaluable coach, mentor, and friend to me, and was an especially helpful source of support while I was writing my dissertation.

I am fortunate to have many amazing friends, both from MIT/WHOI and before. I will think back fondly on all the potlucks, bonfires, seasons of The Bachelor, and adventures that got me through five years on the east coast. My friends were some of my biggest cheerleaders and I cannot thank them enough for their support and encouragement. I am also grateful for the support of the JP Applied Ocean Science &

Engineering community, both current students and alumni, for their camaraderie, advice, and support over the years.

My family has also been incredibly supportive of me throughout my life. While my research was largely a mystery to them, they made me feel loved and cared for. Opportunities to spend time with them were always a welcome reminder that there is so much more to life than school and work. My parents especially supported me in choosing this journey. My [late] dad cultivated my interest in science from an early age and showed me that learning is a life-long endeavor. The level of support that my mom provided me with throughout my graduate studies is beyond words. I also want to acknowledge our dog, Chulo, who was a remarkable source of mental health support, especially as I was writing my dissertation at home.

Finally, I would like to acknowledge the sources of funding that have supported my graduate education:

- Graduate Research Fellowship Program, National Science Foundation (1745302)
- WHOI Ocean Twilight Zone, TED Audacious Project
- WHOI Ocean Ventures Fund
- WHOI Academic Programs Office
- Graduate Student Traineeship, Office of Naval Research (N00014-22-1-2048)
- Undersea Remote Sensing (USRS) program, Office of Naval Research (N00014-16-1-2948)

Contents

List of figures

List of tables

1 Introduction

1.1 Motivation

The development of the field of acoustical oceanography revolutionized our ability to noninvasively study, explore, and operate in the ocean. Acoustical echo-sounding is widely used to assess fish populations and inform fisheries management practices (Lubis and Manik, 2017; Misund et al., 1995; Sthapit et al., 2020). Sonar imaging is used to create detailed maps of the seafloor (Annalakshmi et al., 2019; Hansen, 2019). The use of acoustics in the ocean also led to the discovery of deep scattering layers (Eyring et al., 1948), launching the effort to explore and understand the mesopelagic zone (Aksnes et al., 2017; Buesseler et al., 2007; Irigoien et al., 2014; Klevjer et al., 2016).

An important advancement in acoustical oceanography was the development broadband techniques which not only led to improvements in the spatial resolution of acoustical measurements (Lavery et al., 2017; Stanton et al., 2012), but also enabled received signals to be interpreted in frequency space for more complex analyses including discriminating between types of scatterers and obtaining additional information about the size and other physical properties of scatterers (e.g Agersted et al., 2021; Bassett et al., 2018, 2020; Benoit-Bird and Waluk, 2020; Blanluet et al., 2019; Cotter et al., 2021; Dunn et al., 2023; Forland et al., 2014; Kubilius et al., 2020; Lavery et al., 2007, 2010; Nesse et al., 2009; Stanton, 1996; Stanton et al., 1993, 1994, 1998, 2003; Stanton and Chu, 2000, 2004).

While these advancements have propelled the field forward, there remain many applications to biological and physical processes in the ocean for which broadband techniques have yet to be developed or used. Acoustics are widely used to assess the biomass of fish and some zooplankton populations using verified species-specific sound scattering models (e.g Davison et al., 2015b, 2015a; Escobar-Flores et al., 2020; Gorska et al., 2007; Irigoien et al., 2014; Jech et al., 2015; Lavery et al., 2007; Lawson et al., 2008; Proud et al., 2019), but scattering models have not yet been developed or verified for many types of zooplankton despite their abundance in marine environments, leaving estimates of their biomass poorly constrained. Gelatinous zooplankton (“jellies” or “jellyfish”) in particular have been historically understudied in part because they are difficult to survey via traditional methods like net sampling (Brierley et al., 2001; Pakhomov and Yamamura, 2021). Jellies are becoming increasingly appreciated as important and ubiquitous members of marine communities (Lynam et al., 2006; Pauly et al., 2009; Richardson et al., 2009), warranting an urgent need to understand their global biomass, population dynamics, and impact on human activities (Baliarsingh et al., 2020; Clinton et al., 2021; Pitt et al., 2018; Proud et al., 2019; Zi et al., 2020). Ecosystem-scale monitoring will require the development of efficient remote-sensing approaches for surveying jellies, such as active acoustics, and while multiple studies have employed backscattering measurements in conjunction with other sampling methods to enumerate jellies (Alvarez Colombo et al., 2008; Båmstedt et al., 2003; Brierley et al., 2001; Graham et al., 2010; Kim et al., 2016a; Yoon et al., 2019; Zi et al., 2020), little effort has been made to develop and verify rigorous scattering models that may be used to assess jelly populations with broadband backscattering. The development and verification of such models is a necessary first step toward enabling rapid, field-based monitoring of jelly populations.

Acoustics have also been used for many years to image and quantify oceanic microbubbles generated by breaking surface waves (e.g., Crawford and Farmer, 1987; Dahl, 2003; Deane, 1997; Farmer

et al., 1998, 1998; Medwin and Breitz, 1989; Terrill and Melville, 2000; Trevorrow, 2003; Vagle and Farmer, 1992), but little is known about the density and size distribution of bubbles entrained in frontal structures that form where rivers discharge into coastal oceans or how the hydrodynamics of a front drive its associated bubble population. Frontal structures entrain dense bubble clouds that have been estimated to facilitate a significant proportion of air-sea gas exchange in estuaries (Baschek et al., 2006) and have the potential to interfere with sonar system performance via scattering and absorption (Ainslie, 2005; Bassett and Lavery, 2021; Clay and Medwin, 1964; Medwin, 1977; Reeder et al., 2022; Trevorrow, 2003). An understanding of the bubble densities and size distributions in estuarine fronts is critical for constraining quantitative estimates of their role in these processes. While oceanic bubbles have been studied for many years, few studies have examined the size distributions of bubble populations in tidal fronts or how they are influenced by the hydrodynamics of fronts (Bassett et al., 2023; Marston et al., 2023; Reeder et al., 2022).

Multiple acoustical techniques have been developed over the years to measure bubble size distributions, each with distinct advantages and limitations, and many of which involve instrumentation mounted on stationary platforms (Farmer et al., 1998; Reeder et al., 2022; Terrill and Melville, 2000; Vagle and Farmer, 1992, 1998a). Broadband acoustical measurements over a wide range of frequencies permit high resolution estimates of bubble size distributions over a wide range of sizes. Ship- and vehicle-based backscattering over a wide bandwidth offer the necessary mobility for measuring frontal bubble clouds but involve the potential for excess transmission loss due to near-surface bubbles to impact measurements at certain frequencies (Bassett et al., 2023; Bassett and Lavery, 2021). The use of a towable instrument for measuring frontal bubbles in situ allows for continuous measurements with higher spatial resolution than shipboard backscattering. Employing more than one measurement method builds confidence in their accuracy and allows for a customizable sampling strategy that exploits the advantages of each method (Vagle and Farmer, 1998a). It is also important to relate the measured bubble size distribution to the hydrodynamics of the front, as understanding how currents and turbulent mixing associated with a front drive the bubble density and size distribution will lead to better understanding of the impacts of these features on gas exchange and sonar performance in estuaries.

This dissertation aims to advance the field of acoustical oceanography through contributions to the existing library of sound scattering models for marine organisms and to our understanding of microbubble populations associated with estuarine fronts. First, a sound scattering model is developed for a scyphozoan jellyfish and verified with laboratory measurements. Second, a towable acoustical bubble measurement instrument is described and used in conjunction with existing sound attenuation models for microbubbles to obtain quantitative observations of the bubble size distribution in a tidal front. Third, the bubble size distribution in a front is inferred from backscattering measurements and the impacts of front hydrodynamics are examined. This introductory chapter will briefly review topics and basic scattering principles that will be utilized and discussed further in later chapters.

1.2 Principles of acoustic scattering from bounded objects

1.2.1 Scattering from a single object

This section will review and define the key quantities of interest to acoustical studies as described by Medwin and Clay (1998), providing a foundation for the following sections. For an acoustic

wave of some pressure amplitude P_{inc}, frequency f, wavelength λ, wavenumber k, traveling at speed c, incident on a finite object, the proportion of the incident acoustic energy that will be scattered by the object is

$$P_{scat} = P_{inc}|L(\theta, \phi, f)|(10^{-\alpha R/20})/R \quad (1.1)$$

where $1/R$ represents spherical spreading loss from the object to the receiver, $10^{-\alpha R/20}$ accounts for energy absorption, and $L(\theta, \phi, f)$ is the scattering length (also referred to as "scattering amplitude") describing the ratio of incident to scattered pressure. The acoustic scattering length is a complex function at angle θ in the plane and ϕ out of the plane to the direction of the receiver. In the backscattering case, $\theta = \phi = 0$; in the forward scattering case, $\theta = \pi$ and $\phi = 0$. $L(\theta, \phi, f)$ also depends on the size, shape, orientation, density, and sound speed of the scatterer. For acoustical measurements, the differential scattering cross section is used:

$$\Delta\sigma_s(\theta, \phi, f) = |L(\theta, \phi, f)|^2. \quad (1.1)$$

For backscattering,

$$\Delta\sigma_{bs}(f) = |L_{bs}(f)|^2. \quad (1.2)$$

The total scattering cross section, σ_s, is the integral of $\Delta\sigma_s$ over 4π of solid angle, or the product of $\Delta\sigma_s$ and 4π in the case of omnidirectional scattering (e.g., a gas bubble near resonance). In addition to scattered energy, a portion of incident acoustic energy is also absorbed by the object and is described by the absorption cross section, σ_a. Together, the total scattering cross section and absorption cross section sum to yield the total extinction cross section,

$$\sigma_e = \sigma_a + \sigma_s. \quad (1.3)$$

In practice, it is common to represent measured acoustic scattering on a logarithmic scale. A quantity often used for backscattering measurements is the target strength (TS):

$$TS(f) = 10\log[\Delta\sigma_{bs}(f)] = 20\log[|L_{bs}(f)|] \text{ (dB re 1 m}^2\text{)}. \quad (1.4)$$

The TS is consequently a function of the size, shape, orientation, and material properties of the scatterer. Understanding the TS of an object provides the foundation for more complex measurements of an assemblage of objects and gives predictive power to acoustic measurements.

Multiple model formulations have been developed to predict the TS of scatterers with different properties. Modal series solutions offer complete descriptions of scattering from bounded objects, however these exact solutions to the wave equation are limited to scatterers of certain symmetries. For relatively small wavelengths ($ka \gg 1$), scattering is dominated by specular reflections off the object's boundaries and TS can be approximated via the Kirchoff method. Because the Kirchoff method ignores diffraction from the object's boundaries, it cannot accurately predict scattering from bodies with sharp edges or complex shapes. For weakly scattering objects of any size and shape, the Distorted Wave Born Approximation (DWBA) offers reasonable approximations of TS and will be discussed in a later section.

Total scattering consists of waves reflected off the front interface of the object, waves that penetrate the object and reflect off the back interface, and waves that diffract around the object. For $ka \gg 1$, scattering is dominated by specular or mirror-like reflections and is referred to as the "geometrical" regime. For $ka \ll 1$, scattering is dominated by diffraction and is referred to as the Rayleigh regime. TS in the Rayleigh regime increases linearly with ka and is independent of the shape of the scatterer, while TS in the geometrical regime is more complex due to interference between the incident and scattered waves. The location of the Rayleigh-to-geometric transition ($ka = 1$) may be used from TS measurements to infer the size of the scatterer (Lavery et al., 2010).

1.2.2 Scattering from multiple objects

In the backscattering case where multiple scatterers are present in the insonifying beam, their individual echoes are assumed add incoherently such that the backscattering cross section per unit volume, s_v, may be measured:

$$s_v = \sum^{N} \Delta\sigma_{bs,N} \tag{1.5}$$

where N is the number of scatterers in the insonified volume (Medwin and Clay, 1998). In practice, this quantity is often presented on a logarithmic scale as the volume backscattering,

$$S_v = 10\log_{10}|s_v| \text{ (dB re 1 m}^{-1}\text{)}. \tag{1.6}$$

In many field application cases, such as surveying a dense population of organisms or gas bubbles, volume backscattering is more readily measured than the TS of individual scatterers. In these cases is it crucial to have prior understanding of the TS of the type(s) of scatterers suspected to be present so that information about the population density and composition may be inferred from S_v (e.g., Lavery et al., 2007; Lawson et al., 2008; Vagle and Farmer, 1992).

The possibility of volume backscattering measurements being impacted by multiple scattering may be a concern. However, it has been shown reasonable to assume that in field settings there are generally multiple wavelengths between relatively large biological scatterers (e.g., fish) in an aggregation, so their individual target strengths sum linearly (Foote, 1982, 1983). For dense populations of other types of targets such as microbubbles, shoals of small fishes, and krill, multiple scattering may impact measurements (Andreeva and Belousov, 1996; Bassett et al., 2023).

1.2.3 Scattering from gelatinous marine organisms

From a scattering perspective, most marine organisms fall into one of three broad categories: fluid-like, elastic shelled, and gas bearing (Stanton et al., 1998). The TS spectra of organisms in these three groups varies considerably, with gas bearing organisms such as swim-bladdered fish being much stronger scatters than zooplankton falling into the elastic shelled and fluid-like categories (Fig. 1.1). This is because gas-filled swim bladders are relatively strong scatterers of sound that dominate scattering from the whole fish (Foote, 1985). Each type of scatterer warrants the use of a different TS modeling

approach to capture the relevant physics and there have been many models developed over the years for a variety of different organisms (Jech et al., 2015).

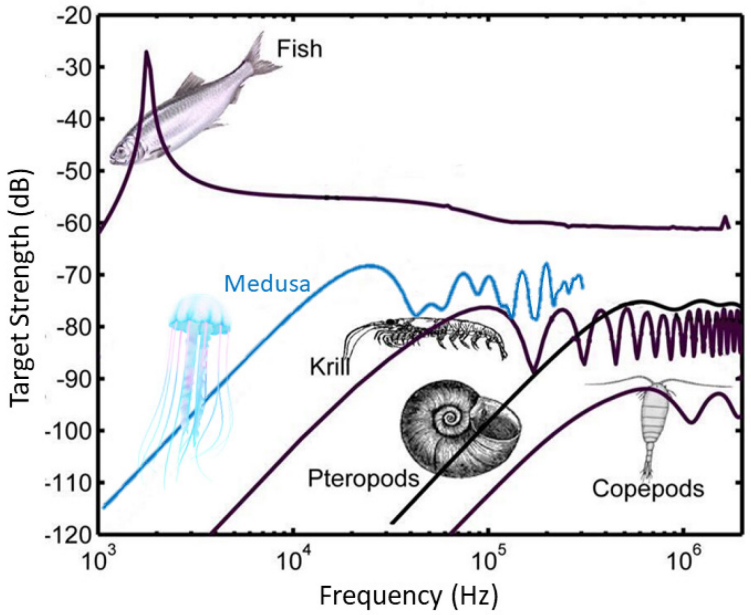

Figure 1.1 Frequency-dependent target strength (TS) [dB re 1 m^2] for several marine organisms including fluid-like (copepod, krill, medusa), elastic-shelled (pteropod), and gas-bearing (fish) animals. (Adapted from Lavery et al. (2007)).

Despite being ubiquitous members of marine ecosystems, gelatinous organisms have been vastly understudied acoustically compared to other types of organisms. Because they are difficult to sample via traditional methods (Brierley et al., 2001), acoustics offer an efficient remote sensing approach to quantify gelatinous biomass. Yet, sound scattering from gelatinous organisms is not well understood and acoustical estimates of their biomass are thus not well constrained (Alvarez Colombo et al., 2008; Lynam et al., 2006; Zi et al., 2020). Additionally, most acoustical studies of gelatinous zooplankton have utilized narrowband echosounder systems (e.g., Brierley et al., 2001, 2004; De Robertis and Taylor, 2014). The use of broadband signals to study gelatinous zooplankton may ameliorate some of the uncertainties impacting previous measurements provided that accurate and correctly parameterized sound scattering models are used to interpret the results (Lavery et al., 2010).

Gelatinous organisms fall into the fluid-like category and are therefore best modeled using a formulation based on the Distorted Wave Born Approximation (DWBA). The DWBA approximates a solution to the wave equation by assuming that the physical properties of the scatterer are sufficiently similar to the surrounding medium's that the insonifying wavenumber inside and outside the scatterer's body are equal (Stanton et al., 1998). This model formulation is explained further in Chapter 2, where a 3-D sound scattering model is developed for a gelatinous organism.

As computational technology has progressed, an increasing number of studies have employed numerical solutions to the DWBA to predict sound scattering from complex and irregular shapes. A 3-D numerical model for fluid-like krill was developed by Lavery et al. (2002) using a high-resolution computerized tomography (CT) scan of an individual. Jones et al. (2009) built upon this approach to

develop a similar model for squid that also incorporates 3-D inhomogeneities in the material properties of the animal's body. These studies found that under a wide range of conditions the 3-D numerical models outperformed analytical and semi-analytical models, which often oversimplify the shape of the organism to analytically solve one or more dimensions of a volume integral. Lee et al. (2012) found that a semi-analytical squid model with shape simplifications performs well near broadside incidence while a full 3-D model can accurately predict scattering at a wide range of orientation angles. Hence, there are some cases where simplified semi-analytical models may provide sufficient accuracy, though 3-D numerical models offer more utility in most use cases.

1.3 Introduction to estuarine fronts

Oceanic fronts have been observed for decades and were first defined by Cromwell and Reid (1956) as a band along the sea surface where the water density changes abruptly. Early explorations of fronts focused on those in deep ocean basins (e.g., Cromwell and Reid, 1956; Katz, 1969; Knauss, 1957). Later studies explored the fronts that form in many estuarine environments when river discharge is sufficiently large relative to tidal volume. For example, discharge from the Mississippi River has been observed to be bounded by strong fronts on both sides (Wright and Coleman, 1971), and the Connecticut River plume has a sharp front at its offshore boundary (Garvine, 1974). Enhanced vertical mixing at a front has important implications for estuarine circulation, productivity, sediment dynamics, and water quality (Largier, 1993). The convergence of currents at the front also enhances surface wave breaking along the front, which in turn enhances the generation of microbubbles (Baschek et al., 2006; Thomson et al., 2014).

As a known mechanism for gas exchange across the air-sea interface, in some circumstances bubbles generated at fronts may play a meaningful role in total gas exchange. For example, it has been estimated that bubbles subducted at fronts may account for ~8% of gas exchange in the Strait of Georgia (Baschek et al., 2006). The density and sizes of microbubbles must be understood to constrain estimates of aeration they facilitate, yet little is known about the bubble populations in estuarine fronts. Downwelling at a front subducts bubbles created by surface waves and forms dense and deeply penetrating plumes that have the potential to interfere with acoustic operations in estuarine environments due to their strong scattering and extinction (Bassett and Lavery, 2021; Chua et al., 2021; Preisig, 2007). For these reasons, gaining an understanding of the bubble distributions in and around fronts and how they are driven by frontal hydrodynamics is necessary to progress our understanding of estuarine systems as a whole and how to operate in them.

1.4 Scattering and extinction from gas bubbles

As opposed to fluid-like scatterers whose material properties are similar to their surrounding medium (i.e., low contrast in acoustic impedance), gas bubbles in seawater present a very strong acoustic impedance mismatch case where there is a large contrast between the physical properties inside and outside the bubble, resulting in very different scattering behavior. The following information about sound scattering from microbubbles is summarized from Medwin and Clay (1998).

1.4.1 Scattering and extinction from a single bubble

From a physics perspective, gas bubbles are treated as gas-filled spheres. A gas-filled sphere has an omnidirectional breathing-mode resonance occurring at $ka = 0.0136$ at sea level, which is obtained from the small ka limit of the spherical modal series solution (Fig. 1.2), where k is the insonifying wavenumber and a is the radius. There are higher order resonances with directional dependence as well. As the bubble's depth increases, so does the ambient pressure and interior gas pressure, effectively making the bubble "stiffer" so the bubble's resonance frequency increases with depth. The resonance frequency also depends on surface tension, the ratio of specific heats between inside and outside the bubble, and the thermal conductivity of the bubble.

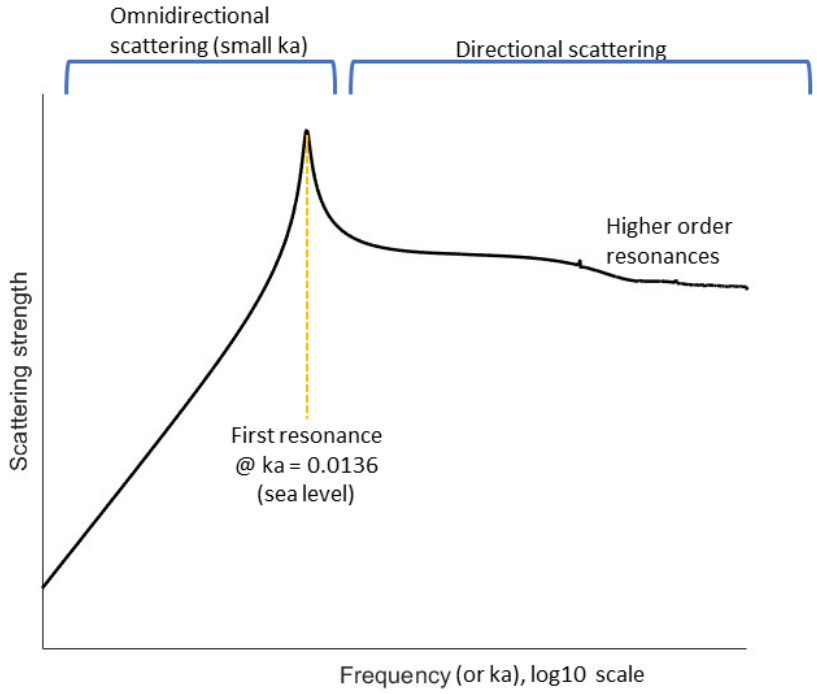

Figure 1.2 Qualitative scattering strength of a single bubble.

Three different modeling approaches have been used to predict the scattering and absorption of bubbles, each with distinct advantages and disadvantages. The first is the modal series solution, which is an exact solution to the wave equation describing scattering from a sphere. The modal solution obtains diffraction contributions to total scattering and accounts for directional dependence. Its main drawback is that it ignores damping effects on the bubble's breathing mode, which has significant ramifications for its accuracy of extinction predictions. The second approach is the harmonic resonator model, which includes damping effects but assumes omnidirectional scattering. Thus, the resonator model is only accurate for $ka \ll 1$. Third, for acoustic measurements of a population of bubbles ranging in size, it is sometimes convenient to assume that a bubble only scatters sound at its resonance frequency, leading to the Resonant Bubble Approximation (RBA) of the resonator model. The RBA is by far the fastest model to calculate but is the least accurate, as it tends to overestimate the quantity of small bubbles due to not

accounting for the off-resonance contributions of the larger bubbles, which can be sufficiently high to mask the resonant peaks of the small bubbles (Fig. 1.3).

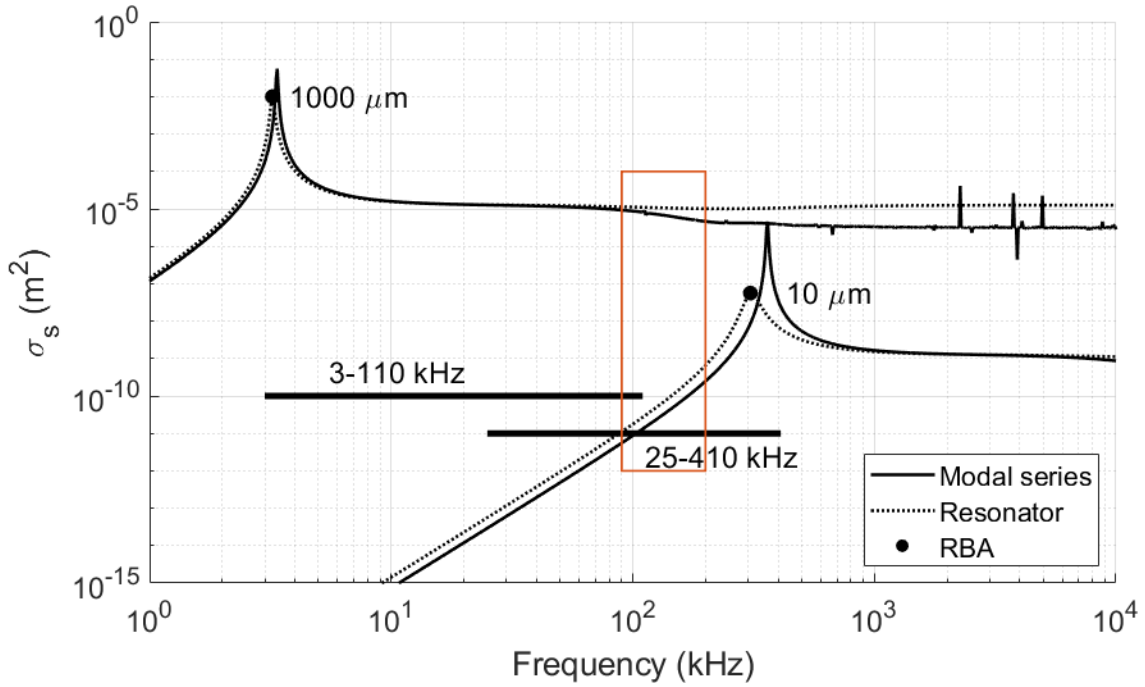

Figure 1.3 Scattering spectra for two bubbles of different sizes using all three modeling approaches. The tail of the larger bubble is a higher magnitude than the resonance peak of the smaller bubble, highlighting the importance of accounting for off-resonance contributions to total scattering and absorption from a population of bubbles. Horizontal lines indicate the ranges of frequencies used in this dissertation by two different measurements techniques (3-110 kHz in Chapter 3, 25-420 kHz in Chapter 4). The orange box indicates the region where the modal series solution diverges from the resonator model for the larger bubble and shows that this region overlaps with the frequencies used in this dissertation.

The harmonic oscillator model may be used to calculate the resonance frequency of a given bubble radius a at a given sound frequency ω:

$$f_R = \frac{1}{2\pi a}\sqrt{\frac{2\gamma b\alpha p_A}{\rho_A}} \tag{1.7a}$$

$$X = a\left(\frac{2\omega\rho_g C_{pg}}{K_g}\right)^{1/2} \tag{1.7b}$$

$$\frac{d}{b} = 3(\gamma-1)\left[\frac{X(\sinh X+\sin X)-2(\cosh X-\cos X)}{X^2(\cosh X-\cos X)+3(\gamma-1)X(\sinh X-\sin X)}\right] \tag{1.7c}$$

$$b^{-1} = \left[1 + \left(\frac{d}{b}\right)^2\right]\left[1 + \left(\frac{3\gamma - 3}{X}\right)\left(\frac{\sinh X - \sin X}{\cosh X - \cos X}\right)\right] \tag{1.7d}$$

$$\alpha = \frac{p_{int}}{p_A} = 1 + \frac{2\tau}{p_A a}\left(1 - \frac{1}{3\gamma b}\right) \tag{1.8e}$$

where definitions of physical constants are summarized in Table 1.1.

Table 1.1 Physical constants used in acoustical bubble calculations. Values are given assuming gas bubbles filled with air where z is depth in meters.

Constant	Definition	Value	Unit
$\boldsymbol{\rho_g}$	Bubble gas density	$\rho_{gA}[1 + 2\tau/(p_A a)](1 + 0.1z)$	g/cm^3
$\boldsymbol{p_A}$	Ambient pressure	$1.013 \times 10^6(1 + 0.1z)$	dynes/cm^2
$\boldsymbol{\rho_{gA}}$	Density of free gas at sea level	1.29×10^{-3}	g/cm^3
$\boldsymbol{C_{pg}}$	Specific heat at constant pressure of bubble gas	0.24	cal/(g °C)
$\boldsymbol{K_g}$	Thermal conductivity of bubble gas	5.6×10^{-5}	cal/(cm s °C)
$\boldsymbol{\gamma}$	Ratio of specific heats of bubble gas	1.4	None
$\boldsymbol{\tau}$	Surface tension at the air/water interface	75	dynes/cm

The effects of thermal conductivity and shear viscosity manifest in the harmonic resonator model as the total damping constant:

$$\delta = \delta_r + \delta_t + \delta_v \tag{1.8}$$

where $\delta_r = ka$ is reradiation (i.e., scattering) damping, δ_t is thermal damping, and δ_v is viscous damping. They are calculated as:

$$\delta_r = ka \tag{1.9a}$$

$$\delta_t = \left(\frac{d}{b}\right)\left(\frac{f_R}{f}\right)^2 \tag{1.9b}$$

$$\delta_v = \frac{4\mu}{\rho_A \omega a^2} \tag{1.9c}$$

where μ is the dynamic viscosity of water ($= 0.0014$ kg/(m s)) and ρ_A is the density of ambient seawater (1030 kg/m^3). The extinction cross section of a single bubble is given by the harmonic resonator model as

$$\sigma_e = \frac{4\pi a^2(\delta/\delta_r)}{[(f_R/f)^2 - 1]^2 + \delta^2} \tag{1.10}$$

where f is frequency and the subscript R indicates the value at resonance. The scattering cross section can be derived from the extinction cross section by

$$\frac{\sigma_e}{\sigma_s} = \frac{\delta}{\delta_r}. \tag{1.11}$$

Despite being most accurate near and below resonance, at high frequencies the harmonic resonator model for the scattering cross section converges to a value four times that of the modal series solution because it does not include higher order resonances (Fig. 1.4). Thus, for numerical calculations of predicted backscattering in this dissertation, a hybrid scattering model was generated using the resonator model for $ka < 0.1$ and the modal solution for $ka > 0.1$ (Fig. 1.4), following the approach of Lavery et al. (2007).

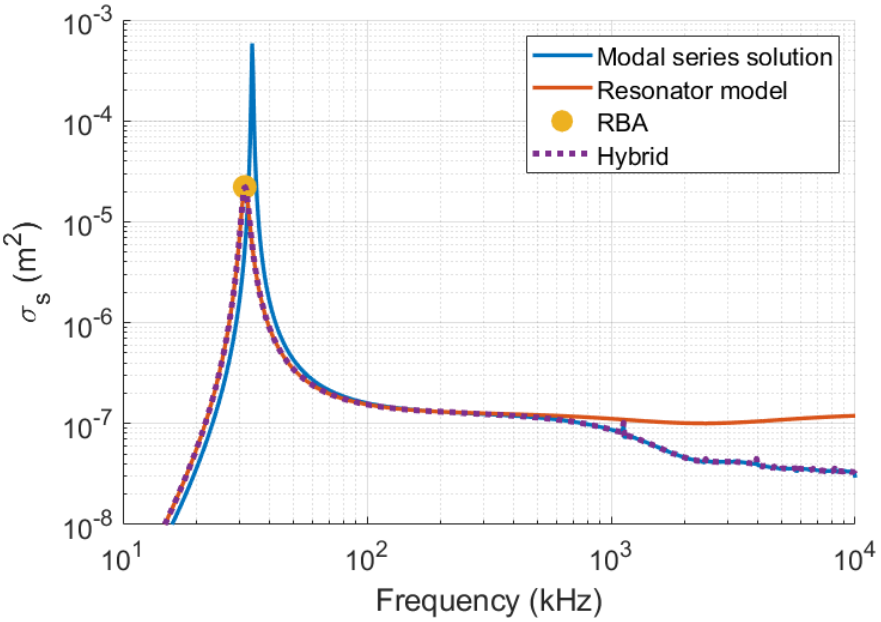

Figure 1.4 Predicted backscattering cross section for a bubble of radius 100 µm, including a hybrid model comprised of the resonator model for $ka < 0.1$ and the modal solution for $ka > 0.1$.

For predicting a bubble's extinction cross section, the modal series solution and harmonic resonator model agree reasonably well above resonance, however the modal solution overestimates extinction at resonance and underestimates extinction below resonance due to not including the damping effects of reradiation, thermal conductivity, and viscous forces (Fig. 1.5). Thus, the resonator is the all-around most accurate model to represent bubble extinction and is used throughout this dissertation.

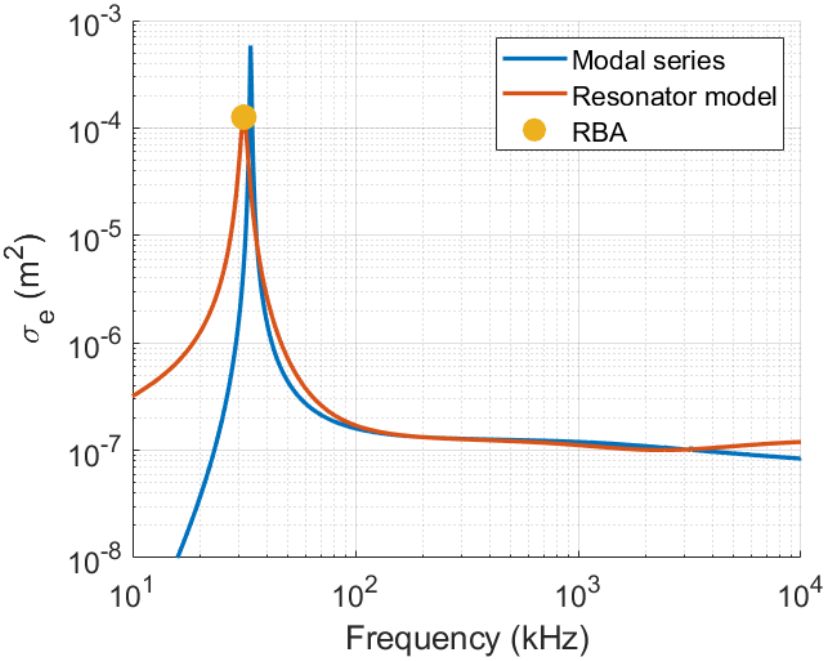

Figure 1.5 Predicted extinction cross section for a bubble of radius 100 µm.

1.4.2 Scattering and extinction from many bubbles

In practice, acoustical measurements of a population of bubbles of a range of sizes are much more likely than measurements of single, isolated bubbles. As stated in Section 1.2.2, echoes from multiple bubbles are assumed to sum incoherently. The volume backscattering coefficient for a population of oceanic bubbles following a continuous distribution of sizes is expressed via the resonator model as

$$s_v = \sum^{N} \Delta\sigma_{bs,N} = \int_a [n(a)da][\Delta\sigma_s(a,f)] = \int_a [n(a)da]\left[\frac{a^2}{[(f_R/f)^2 - 1]^2 + \delta^2(f)}\right] \quad (ka < 1) \tag{1.12}$$

where $n(a)da$ is the bubble size distribution given by the number of bubbles per unit volume, $n(a)$, of radius between a and $a + da$. A radius increment (da) of 1 µm is commonly used. This integral is straightforward to numerically integrate for a given frequency over a known bubble size distribution. However, when s_v is measured for an unknown $n(a)da$, the integral becomes ill-posed so inverting it for $n(a)da$ directly is impractical.

A straightforward way to estimate $n(a)da$ from s_v is to assume bubbles scatter sound only at their resonance frequency (i.e., the Resonant Bubble Approximation (RBA)). Besides assuming that scattering is dominated by resonant bubbles, the RBA also assumes that $n(a)da$ and $\delta(f)$ are near constant around resonance so that $n(a)$ may be factored out of the integral to obtain the RBA expression for s_v:

$$s_v \approx \frac{\pi a_R^3 n(a_R)}{2\delta_R}. \tag{1.13}$$

Likewise, the extinction cross sections of individual bubbles are assumed to sum incoherently to yield the extinction cross section per unit volume for a population of bubbles of a continuous distribution of sizes:

$$s_e = \int_0^\infty \sigma_e n(a) da = \int_0^\infty \frac{4\pi a^2 (\delta/\delta_r) n(a) da}{[(f_R/f)^2 - 1]^2 + \delta^2} \quad (ka < 1). \tag{1.14}$$

Then, the attenuation rate due to bubbles for an acoustic signal traveling through bubbly water in dB/m relative to 1 W is

$$\beta = 4.34 s_e \tag{1.15}$$

where the factor of 4.34 comes from the conversion to decibels. The RBA expression for s_e is thus

$$s_e \approx \frac{2\pi^2 a_R^3 n(a_R)}{\delta_R} \tag{1.16}$$

and the RBA expression for the excess attenuation in dB/m is

$$\beta \approx \frac{85.7 a_R^3 n(a_R)}{\delta_R}. \tag{1.17}$$

The main disadvantage of approximating $n(a)da$ from the RBA is that this approach does not account for off-resonance contributions to scattering, which could be significant in the presence of larger bubbles (Fig. 1.3), potentially leading to overestimates of the density of smaller bubbles (Fig. 1.6).

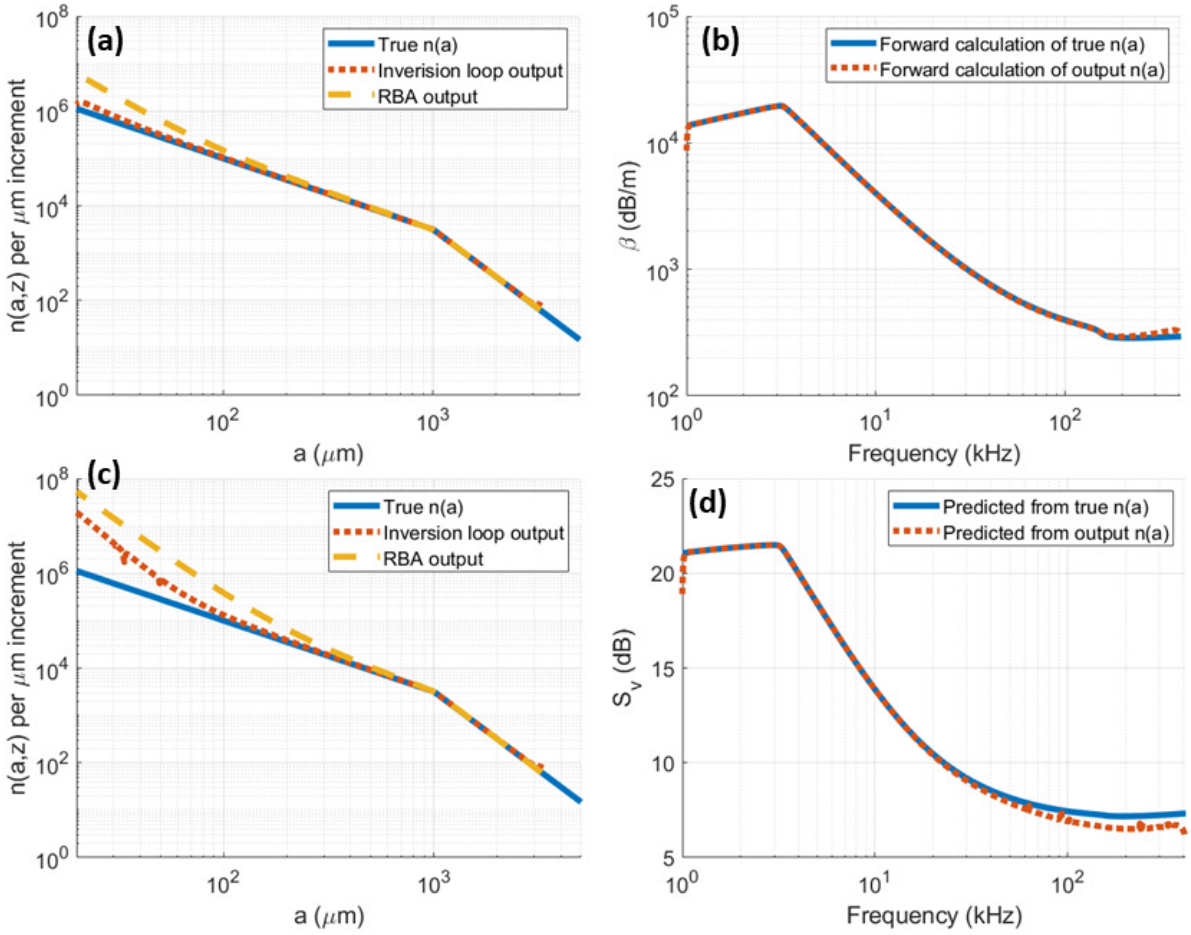

Figure 1.6 Comparison of bubble size distribution inversion results from (b) attenuation and (d) volume backscattering for a model bubble distribution ((a), (c)) based on observations under breaking waves (Baschek et al., 2006; Deane and Stokes, 2002). $n(a) = A_1 a^{-3/2}$ for $a \leq 1000\ \mu m$ and $n(a) = A_2 a^{-10/3}$ for $a > 1000\ \mu m$, where $A_1 = 10^5$ and $A_2 = A_1 \times (1000\ \mu m)^{-3/2}/(1000\ \mu m)^{-10/3}$. b) Eq. (1.17) was used to calculate a predicted β [dB/m re 1 W] for the "true" $n(a)$ in (a), which was then fed into the inversion loop method described by Caruthers et al. (1999) and the RBA. An additional β was calculated from the inversion loop output to demonstrate its accuracy. In this example the RBA overestimates the density of smaller bubbles due to neglecting off-resonance contributions to extinction. The process is repeated in (c) and (d) for volume backscattering from the same $n(a)$ and is discussed further in Chapter 4. The RBA estimates a higher density of smaller bubbles than the inversion does, however both calculation methods overestimate $n(a)$ from volume backscattering for the model bubble size distribution, which may include larger bubbles than expected in a field setting.

Several approaches have been developed to estimate $n(a)da$ from s_v and β while accounting for off-resonance contributions. Commander and McDonald (1991) described a rather involved finite-element approach that has been used in several studies with narrowband measurements (Farmer et al., 1998; Terrill and Melville, 2000). Caruthers et al. (1999) developed a simpler, broadband approach that starts with the RBA and then employs an iterative loop to correct for off-resonance contributions. Another broadband approach developed by Czerski (2012) converts the problem into a straightforward

matrix inversion, though the results appear to be less accurate than the Caruthers et al. (1999) approach. The iterative loop method described by Caruthers et al. (1999) for inverting broadband attenuation is used in Chapter 3 to obtain $n(a)da$ estimates (e.g.,, Fig. 1.6). This method was also adapted to obtain $n(a)da$ estimates from broadband backscatter measurements in Chapter 4.

As a modeling exercise, a hypothetical depth-dependent bubble size distribution was generated using the observed power laws and Hinze scale from Deane and Stokes (2002) and the depth dependence given by Baschek et al. (2006) for a wave with 1 m amplitude (See Fig. 1.6 caption):

$$n(a,z) = \beta_0 a^{\alpha} e^{z/\delta} \tag{1.18}$$

where $n(a,z)$ is the bubble density per unit volume for bubble radius $a = 20$ to 5000 μm at depth z, $\beta_0 = 1 \times 10^5$ is an arbitrary scaling factor, $\alpha = [-3/2, -10/3]$ is the power law slope, and δ is the bubble entrainment depth equal to 1/4 of the wave amplitude (Fig. 1.7).

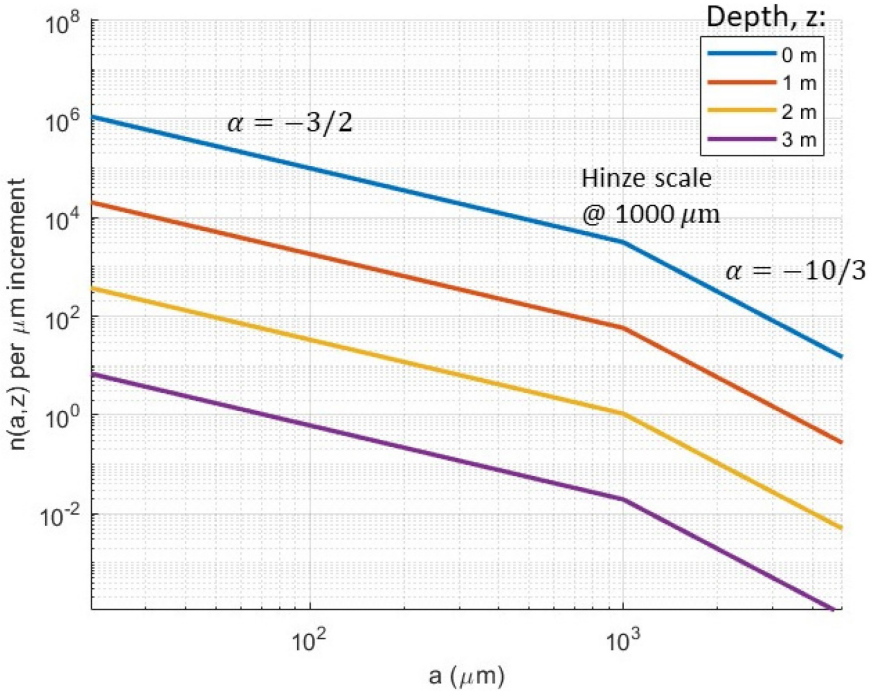

Figure 1.7 Model depth-dependent bubble size distribution generated from Deane and Stokes (2002) and Baschek et al. (2006). Same formulation of $n(a)$ as in Figure 1.6 with an added factor of $e^{-z/\delta}$, where z is depth [m] and $\delta = 1/4$.

The frequency-dependent attenuation, β [dB/m re 1 W], was predicted for $n(a,z)$ using the RBA, resonator model, and modal series solution (Fig. 1.8). Whether β was calculated using the physical properties of seawater or freshwater did not significantly impact the result. The forward attenuation calculation demonstrates where the RBA falls short, as by not including off-resonance contributions it predicts too little attenuation at the higher frequencies corresponding to smaller bubbles. The resonator model and modal series solution agree reasonably well despite the modal solution underestimating

extinction below resonance, highlighting the relative importance of accurately predicting extinction at and above resonance.

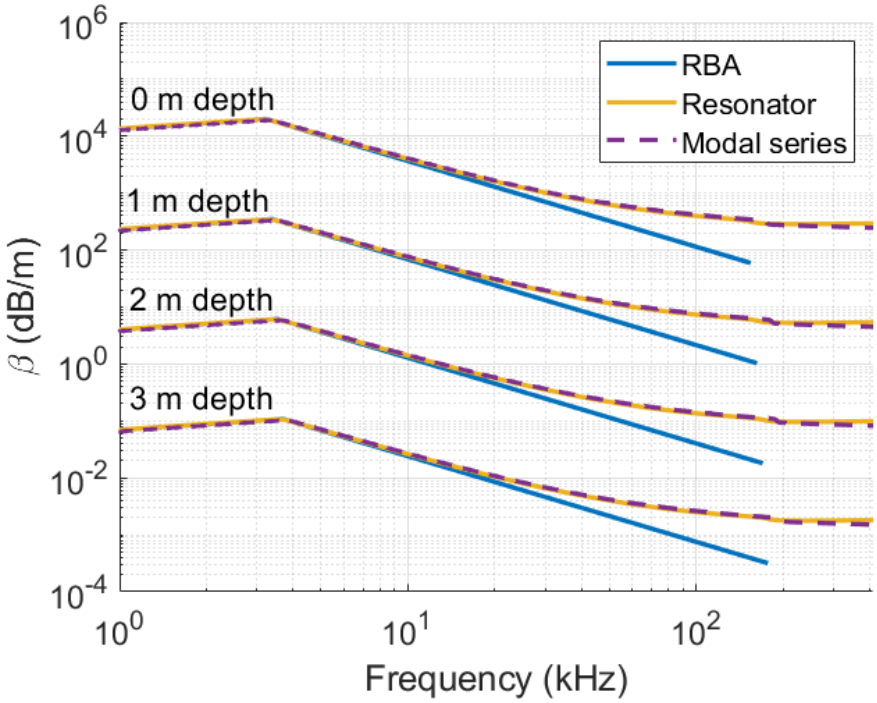

Figure 1.8 Modeled attenuation [dB/m re 1 W] for a depth-dependent bubble size distribution using the Resonant Bubble Approximation (RBA), resonator model, and modal series solution.

The frequency-dependent volume backscattering coefficient, S_v, was also predicted for $n(a, z)$ using the RBA, resonator, modal series solution, and the hybrid resonator-modal series models described in Section 1.4.1 (Fig. 1.9). Like the forward attenuation calculation, the forward backscattering calculation shows where the RBA underestimates volume backscattering due to ignoring off-resonance contributions at higher frequencies. The modal series solution overestimates volume backscattering because its ignorance of damping effects causes it to overshoot the magnitude of backscattering at resonance. At higher frequencies, the resonator model overestimates volume backscattering due to not accounting for higher order resonances. The hybrid model offers the most accurate prediction of volume backscattering across the widest range of frequencies (Fig. 1.9).

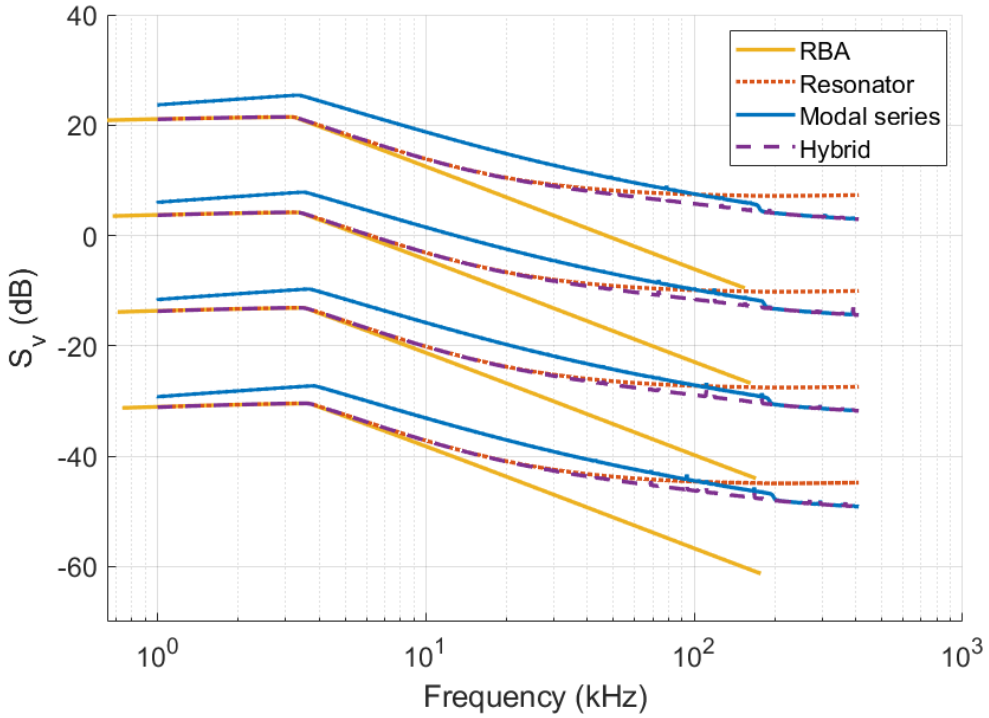

Figure 1.9 Modeled volume backscattering spectra [dB re 1 m^{-1}] vs. frequency for a depth-dependent bubble size distribution using the Resonant Bubble Approximation (RBA), resonator model, modal series solution, and a hybrid resonator-modal series model.

In practice, volume backscattering measurements would be subject to extra transmission loss as the signal travels through bubbly water, so S_v was additionally predicted for $n(a, z)$ accounting for estimated excess transmission loss with $\beta_0 = 1 \times 10^3$ (Fig. 1.10). Provided that the bubble distribution varies with depth, the excess transmission loss was estimated at each depth by integrating over the predicted attenuation across shallower depths, then subtracting two times the predicted attenuation from the uncorrected volume backscattering spectrum to account for the signal's two-way travel (Fig. 1.10). Excess transmission loss has the greatest impact at lower frequencies which correspond to larger bubbles. The RBA still underestimates volume backscattering strength with excess transmission accounted for (Fig. 1.10).

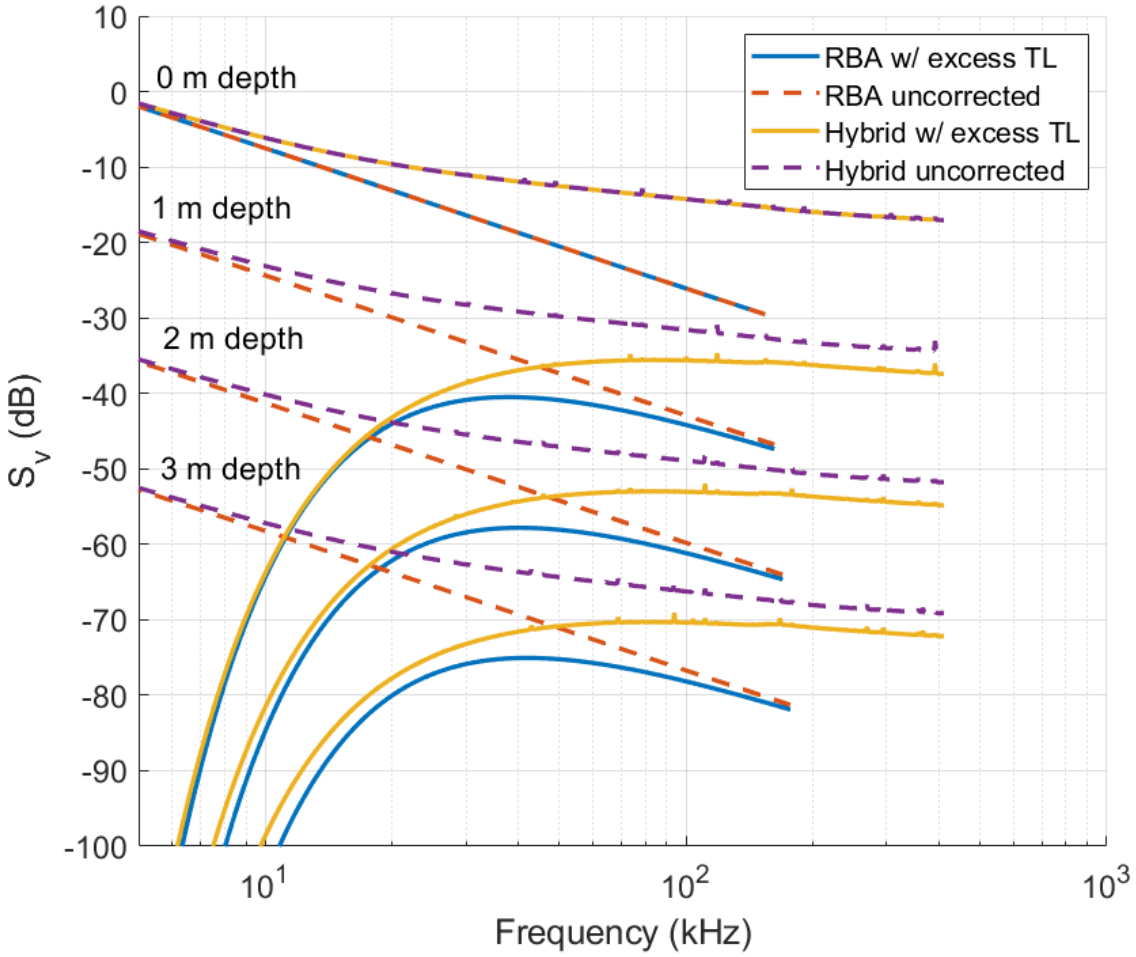

Figure 1.10 Modeled volume backscattering spectra [dB re 1 m^{-1}] vs. frequency for a depth-dependent bubble size distribution and accounting for estimated excess transmission loss accumulated over two-way travel from the surface. The $n(a)$ used in this calculation was equivalent to that in Figure 1.6-9 but with $A_1 = 10^3$.

1.4.3 Sensitivity of inversion calculation

Because the overall spectral behavior of attenuation from bubbles is similar to that of backscattering, the following exercises exploring the sensitivity of the inversion calculation were calculated using the attenuation inversion on the model $n(a, z = 0)$ described in the previous section and it is assumed that the volume backscattering inversion would yield comparable results. It is also important to note that for all inversion results reported in Chapters 3 and 4, the yielded estimate of $n(a)$ has been plugged back into the forward calculation to ensure that the measured attenuation/volume backscatter is recovered with reasonable accuracy.

First, let us explore whether the bandwidth of the acoustical measurement has a significant impact on the inversion result. To simulate measurements of different bandwidths, $n(a)$ was plugged

into the forward attenuation calculation to obtain $\beta(f)$ over a specified frequency band, and this result was then plugged into the inversion to yield the estimated $n(a)$ obtained from a "measurement" over that frequency band. The larger bubbles significantly influence attenuation and scattering from the entire bubble population and these bubbles are detected with lower frequencies, so a series of inversions were calculated while varying the minimum frequency in the band (Fig. 1.11). The choice of maximum frequency (410 kHz) does not significantly impact the inversion results because the corresponding smaller bubbles have little impact on the attenuation spectrum, so only the minimum frequency was varied. The results from this exercise suggest that the lower the minimum measurement frequency, the more accurate the inversion result (Fig. 1.11). This highlights the importance of detecting the larger bubbles, as failing to capture them may lead to overestimates of the density of the smaller bubbles.

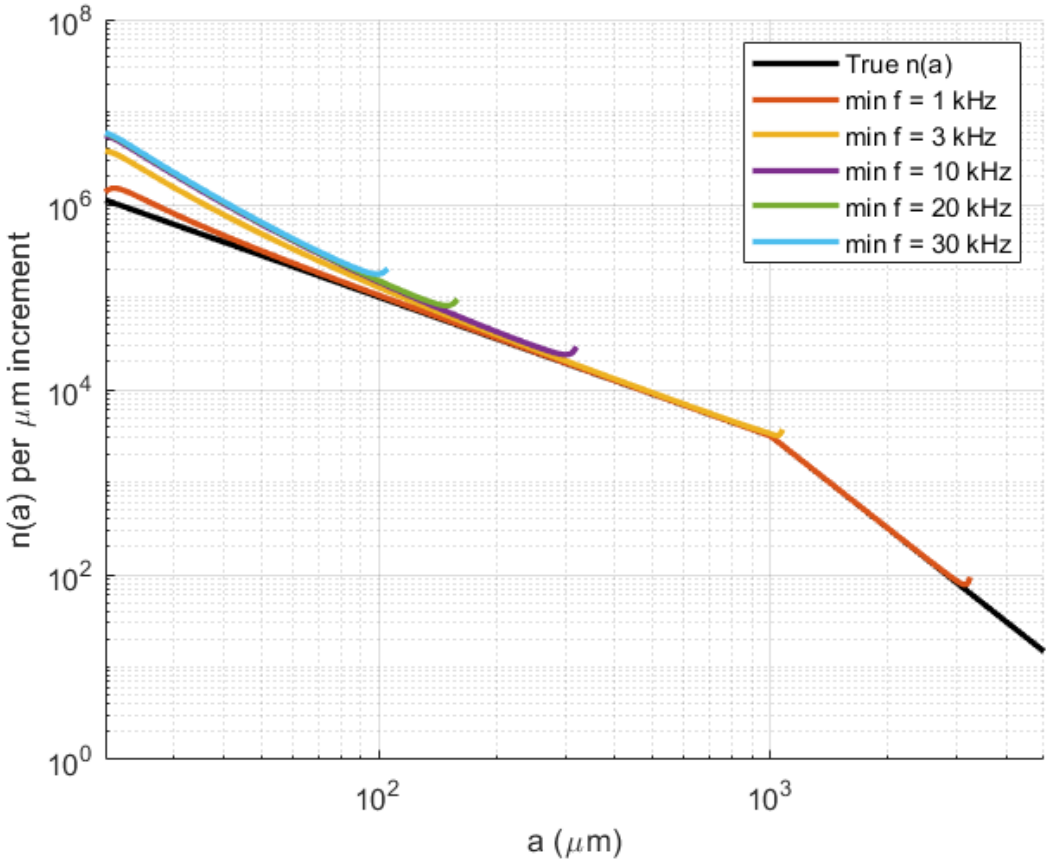

Figure 1.11 Estimated bubble size distribution from simulated attenuation measurements using frequency bands with a maximum frequency of 410 kHz and varying minimum frequency. Agreement with the "True $n(a)$" indicates accuracy.

Next, let us consider the frequency ranges used in this dissertation. Chapter 3 uses a measurement frequency range of 3-110 kHz for attenuation while Chapter 4 uses a range of 25-410 kHz for volume backscattering. Measurements of β were simulated for both frequency bands and plugged

into the inversion as described in the preceding paragraph to examine whether one frequency band would yield more accurate $n(a)$ estimates than the other (Fig. 1.12.a). Disagreement between the two frequency bands would suggest that the two measurement methods are not comparable, however the results from this exercise show reasonably good agreement in the estimated bubble size distribution for both frequency bands (Fig. 1.12.a). While neither frequency band yields an accurate bubble size distribution below a bubble radius of 10^2 μm, they at least agree with one another well enough that measurements using both frequency bands may be compared.

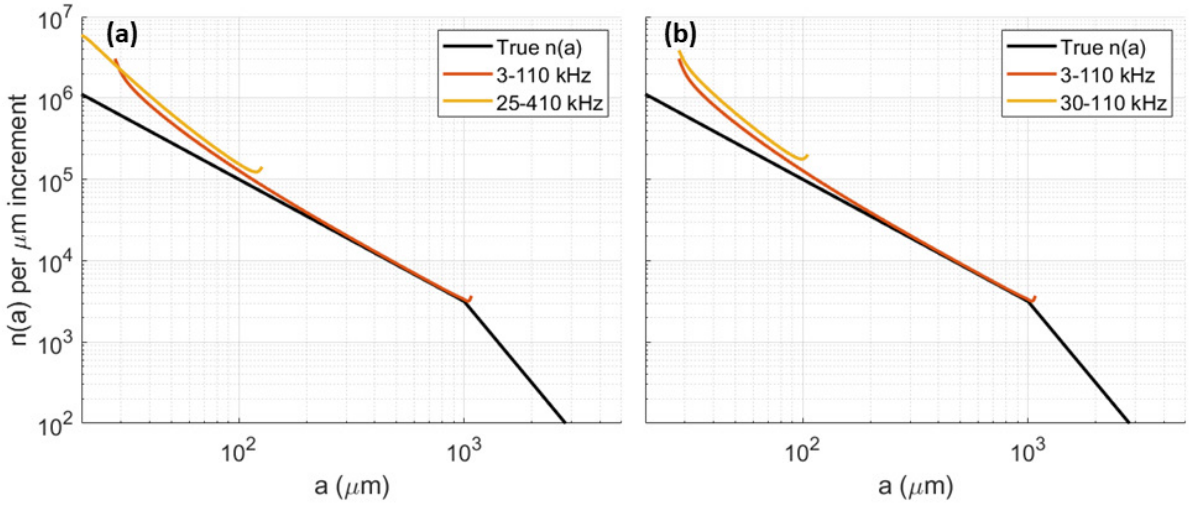

Figure 1.12 Estimated bubble size distributions from simulated attenuation measurements over the frequency bands used in this dissertation. a) Inversion results over 3-110 kHz (Chapter 3) and 25-410 kHz (Chapter 4). b) Inversion results over 3-110 kHz (full band used in Chapter 3) and 30-110 kHz (partial band omitting saturated 3-30 kHz signal in Chapter 3 field measurements).

Another concern with the measurements presented in Chapter 3 is that the 3-30 kHz portion of the transmitted 3-110 kHz frequency band was saturated in the field, yielding a usable attenuation measurement band of 30-110 kHz. To examine the potential impact of omitting the saturated section of the frequency band, inversions were calculated using simulated measurements over the full 3-110 kHz band and over the truncated 30-110 kHz band (Fig. 1.12.b). Although limited to a much smaller range of bubble sizes, the truncated frequency band predicted $n(a)$ with comparable accuracy to the full band, alleviating concerns about the saturated signal yielding significantly less accurate inversion results. However, none of the frequency bands used in this dissertation appear to accurately recover the true $n(a)$ for radii smaller than 10^2 μm (Fig 1.12), which raises the question of whether we actually expect to observe the range of bubble sizes modeled here.

Last, let us examine the impact of the range of bubble sizes present on inversion accuracy. The range of radii in a bubble cloud changes as bubbles rise to the surface or dissolve, and the loss of larger bubbles particularly impacts acoustical measurements. To vary the range of radii in the bubble size distribution, $n(a)$ was generated using just the specified range of radii and the predicted attenuation was calculated for 3-110 kHz, then fed into the inversion calculation (Fig. 1.13). Like how the high-frequency cutoff had little impact on inversion results, the choice of minimum bubble radius also had little impact on the inversion result so was fixed at 20 μm while the maximum radius was varied. The

results from this exercise suggest that the inversion is reasonably accurate when the maximum radius is below the Hinze scale (i.e., all bubbles are smaller than 1000 μm radius). The presence of bubbles larger than the Hinze scale yields overestimates of the density of smaller bubbles (Fig. 1.13). Therefore, for measurements of real bubble populations, it would be prudent to estimate the largest bubble size expected to be present in the measurement volume to gain a sense of uncertainty in the estimated bubble size distribution. For example, simulated measurements over a bubble size distribution of 20-500 μm (Fig. 1.14) yield more accurate inversion results than simulated measurements over a bubble size distribution 20-5000 μm (Fig. 1.12.a).

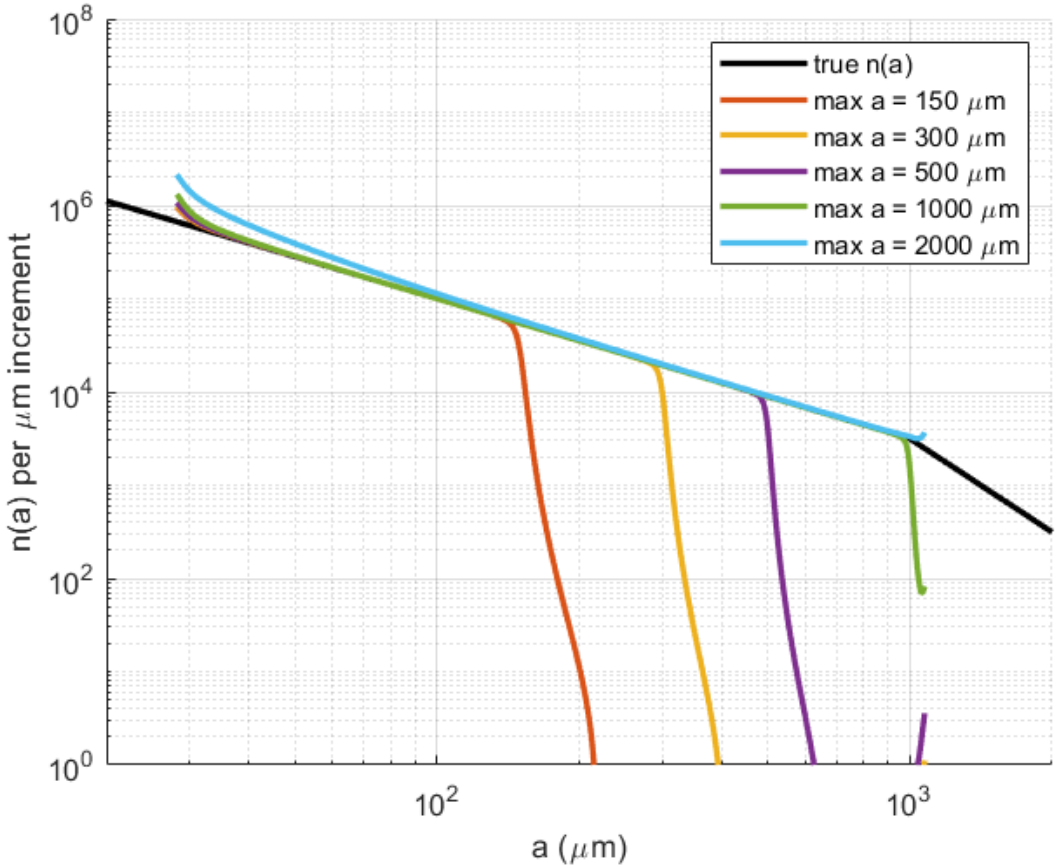

Figure 1.13 Estimated bubble size distribution from simulated attenuation measurements of a model bubble size distribution with a minimum radius of 20 μm and varying maximum radius. Agreement with the "True $n(a)$" indicates accuracy.

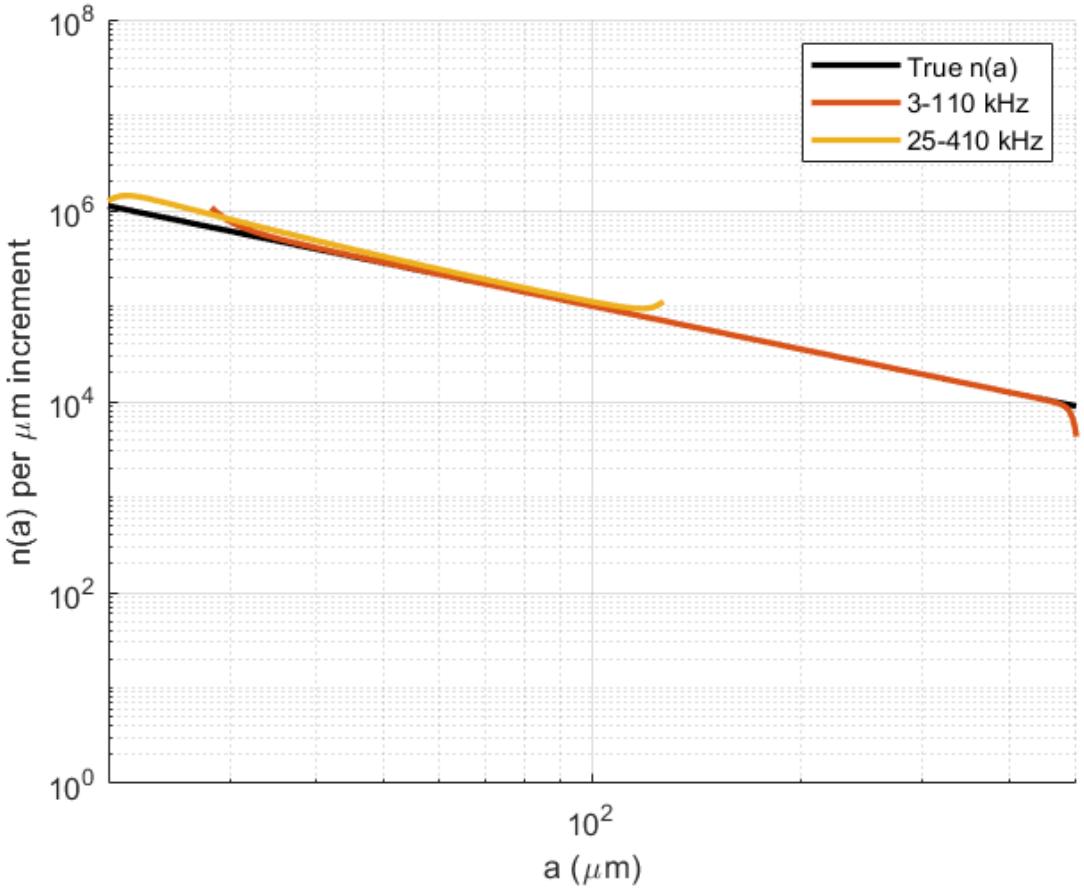

Figure 1.14 Estimated bubble size distributions from simulated attenuation measurements over the frequency bands used in this dissertation. The "True $n(a)$" includes bubbles of radii 20-500 μm.

1.5 Dissertation overview and contributions

Drawing meaningful insights from acoustic data requires an understanding of the underlying physical principles governing how acoustic signals interact with objects of interest. This understanding may then be applied to a broad range of problems. This dissertation combines laboratory experiments, field observations, and theoretical scattering model development to address topics related to scattering from both very weak scatterers and very strong scatterers, representing two extremes on the spectrum of scattering from bounded objects.

Chapter 2 explores the process of developing a physics-based sound scattering model for a common species of scyphozoan jellyfish using the Distorted Wave Born Approximation (DWBA), which describes scattering from fluid-like objects. The jellyfish sound scattering model is built using the approximate shape of a jelly's bell and can be adjusted to represent each flexion state of the jelly's swimming pulsations, ranging from a fully contracted bell to fully relaxed. The model is then validated with controlled, laboratory target strength (TS) measurements of live jellies.

Chapters 3 and 4 apply existing sound scattering models to examine gas bubbles associated with estuarine tidal fronts. While bubble size distributions under breaking waves in the lab and open ocean have been extensively studied, little is known about the densities and size distributions of bubbles entrained in fronts. Yet, tidal fronts facilitate air-sea gas exchange in coastal environments and have the potential to interfere with acoustic communications and sonar performance in these environments. The aim of these chapters is to develop some understanding of the bubble size distribution and its driving physical mechanisms in a frontal system. Specifically, Chapter 3 describes a towable instrument developed to measure broadband excess attenuation from bubbles in the field, from which the bubble size distribution is inferred using existing scattering models. The instrument was tested in a laboratory wave tank and its performance was validated with existing measurements of bubbles under breaking waves. Then, the bubble size distribution was estimated from measurements of the Connecticut River tidal ebb plume front. This chapter presents estimates of the bubble size distribution in a tidal front inferred from attenuation measured by this towed instrument.

Chapter 4 considers the relationship between bubbles entrained in a front and the influence of kinematics on the bubble density and size distribution. This chapter uses measurements of broadband volume backscattering from which the bubble size distribution is inferred using existing scattering models. The bubble size distribution was examined with varying depth in the convergence zone of the front where it is subject to a strong downwelling current, as well as with varying distance away from the front where small bubbles subducted at the front are then advected. This chapter presents observations of spatial trends in the bubble size distribution associated with the Connecticut River front and speculates about how these trends might be driven by kinematics of the front.

Chapter 5 contains closing comments summarizing the contributions of this dissertation to the field of acoustical oceanography. The significance and broader impacts of the work presented are discussed as well as recommendations for future studies.

2 Broadband backscattering from scyphozoan jellyfish

Reproduced from Rachel E. Kahn, Andone C. Lavery, Annette F. Govindarajan; Broadband backscattering from scyphozoan jellyfish. *J. Acoust. Soc. Am.* 1 May 2023; 153 (5): 3075-. https://doi.org/10.1121/10.0019577, with the permission of the Acoustical Society of America.

2.1 Introduction

Jellyfish populations and bloom occurrences have been observed to increase globally over the past several decades (Brotz et al., 2012; Duarte et al., 2013; Mills, 2001). This increase could be due in part to extra habitat for benthic jellyfish polyps associated with artificial structures in coastal areas (Duarte et al., 2013). It could also be due to other seasonal and anthropogenic factors that permit jellyfish to flourish in environments where other pelagic species are unable to sustain their populations (Richardson et al., 2009 and references therein), including overfished ecosystems (Lynam et al., 2006). However, there is little evidence to support claims that jellyfish blooms are exacerbated by anthropogenic stressors (Pitt et al., 2018), indicating a need to better understand and monitor their populations. Jellyfish abundance and biomass could be an indicator of ecosystem health and productivity, especially as their role in marine ecosystems as both predator and prey is becoming better understood (Pauly et al., 2009), as well as their impact on human activities like tourism, aquaculture, and power plant operations (Baliarsingh et al., 2020; Clinton et al., 2021; Zi et al., 2020).

While estimates of jellyfish biomass and distribution would permit better understanding of their population dynamics, they are challenging to survey by traditional methods as their gelatinous bodies are either easily damaged by sampling nets or occur in such high abundance that they clog and burst the nets (Brierley et al., 2001). Optical sensing and aerial surveys provide other means for studying jellyfish in situ, however the high attenuation of light in water permits a relatively small sampling volume, rendering optical methods inefficient and relatively uncertain for large-scale abundance estimates (Båmstedt et al., 2003; Graham et al., 2003; Houghton et al., 2006). Acoustic surveys provide a means of surveying jellyfish on a larger scale and have been used in multiple studies, in conjunction with other sampling methods such as trawls and video footage, to enumerate jellyfish and characterize their distributions (Alvarez Colombo et al., 2008; Båmstedt et al., 2003; Brierley et al., 2001; Graham et al., 2010; Kim et al., 2016b; Yoon et al., 2019; Zi et al., 2020).

This investigation focused on modeling the acoustic target strength (TS) of a medusoid jellyfish (Cnidaria: Scyphozoa) and verifying the TS with controlled, broadband laboratory measurements. TS is a complex function of size, morphology, orientation, and material properties (i.e., the density and sound speed of an organism's tissue (Stanton et al., 1994)). Jellies are acoustically classified as fluid-like, weakly scattering organisms (Stanton, 1996), so the Distorted Wave Born Approximation (DWBA) was used to formulate the scattering model. An approximate 3-D medusa shape was developed and digitized to calculate a medusa's predicted target strength. To reflect the diversity of different species of medusae as well as swimming-related cyclical changes in shape, the parameters of the model can be tuned to reflect various morphologies and material properties. This study presents data and modeling results obtained

for live individuals of a species of sea nettle, Chrysaora chesapeakei, representing a common morphology of medusa.

A known TS for medusae is crucial for making accurate abundance estimates from measurements of volume scattering. Most acoustic studies on jellies have focused on measuring TS at multiple narrowband frequencies commonplace for fisheries applications. A broadly used method of measuring medusa TS is by analyzing in situ backscattering measurements, by detecting single targets (Alvarez Colombo et al., 2008; Brierley et al., 2004; Cimino et al., 2018; De Robertis and Taylor, 2014; Kim et al., 2016b; Yoon et al., 2012) and/or by a combination of echo integration and trawls/video to obtain a relationship between echo intensity and numerical density (Båmstedt et al., 2003; Brierley et al., 2001). A handful of studies have obtained ex situ TS measurements in either a controlled laboratory setting or a semi-controlled open water enclosure (Hirose et al., 2005, 2009; Kang et al., 2014; Monger et al., 1998; Mutlu, 1996; Yoon et al., 2015, 2010). Cyclical oscillations in TS of magnitudes up to 15 dB have been observed due to a medusa's swimming pulsations (Brierley et al., 2004), however the use of narrowband signals limits the amount of information available related to variations in size and shape.

TS is determined by multiple animal parameters, so an accurate medusa scattering model is essential to verify and give predictive power to measurements. Few studies have attempted to model backscattering from medusae. The first medusa scattering model was developed by Monger et al. (1998) and used a ray-based approximation to predict backscattering at broadside incidence. Their ellipsoid-based model shape was later reformulated into a DWBA-based model (Graham et al., 2010). Other studies employing DWBA-based scattering models utilized the outer shape of the medusa's bell, obtained from side-angle images and assuming radial symmetry (Lee and Hwang, 2009; Shin et al., 2019; Yoon et al., 2019).

Acoustic scattering models based on simple shapes are useful for predicting the TS of biological organisms, however oversimplification results in inaccuracies. Balancing ease of use and accuracy are the primary drivers for these physics-based scattering models. In this paper, I approximate the medusa shape with two partial spherical caps to construct the oral and aboral surfaces of the bell and vary the width-height aspect ratio to predict changes in TS from swimming pulsations. Much of the physics can be captured by accurately representing the outer boundaries of the organism, assuming small internal inhomogeneities are insignificant contributors to scattering.

Broadband techniques have been widely used for both laboratory and field measurements of organisms (Jones et al., 2009; Lavery et al., 2002, 2010; Stanton, 1996). Previous work employing broadband signals to detect jellies took place in a laboratory setting and utilized a frequency band centered at 1 MHz (Vasile et al., 2016), a much shorter wavelength with higher attenuation than what is practical for field deployments. This study presents broadband backscattering measurements of individual medusae collected with a system suitable for field operations and frequency range used commonly for fisheries (52-161 kHz) and compares them with model predictions.

2.2 Experimental methods

2.2.1 System description

The echosounders used to collect TS measurements consisted of two Kongsberg Simrad split-beam, broadband, transducers (ES70-7CD and ES120-7CD), a Simrad Wide Band Transceiver (WBT) Tube

(Simrad, Egersund, Norway), and a data acquisition laptop running Windows 10 with the Simrad EK80 software application for data acquisition. The split-beam transducers allowed for the localization of a target in the beam and correction of off-axis beam parameters as appropriate. A video camera (Sony SNC-VB770 with Sony SEL35F28Z lens) was mounted in a pressure housing adjacent to the transducers to collect coincident video and still images of the jellies. The Simrad EK80 data acquisition software for acoustic data and VLC media player for video footage collection were run simultaneously on the single data acquisition laptop to ensure that time was synced between the video and acoustics. A custom acoustical-optical data mounting platform was designed using an existing stainless steel frame (Lavery et al., 2010) and a laser-cut PVC base-plate, where the two broadband transducers were mounted in a downward-looking orientation. The Simrad WBT Tube was attached vertically in the frame. The video camera and Tube were powered from the same power supply.

Experimental trials were conducted in August-September 2021 in a cylindrical test tank about 3 m wide and 3 m deep. The tank was filled with filtered seawater, and the temperature and salinity were measured to determine the sound speed of water in the tank. The data acquisition system was lowered into the tank via an overhead crane system.

2.2.2 Acoustic calibration

A laboratory calibration was performed in August 2021. The echosounders were calibrated in the tank using a spherical, 38.1-mm-diameter, tungsten carbide with 6% cobalt standard target, which was tethered on fishing line approximately 2.5 m below the transducers. The EK80 standard calibration software was used to collect data in all four sectors and the center of each split-beam transducer. Calibration curves for both transducers were calculated from the matched filter output following the method of Lavery et al. (2017), and it was determined that the ES70 had a usable frequency band of 52-90 kHz and the ES120 had a usable band of 93-161 kHz (Fig. 2.1). A consistent set of operational parameters for the echosounders was used for the entire duration of this study (Table 2.1). A calibration for the video camera was unnecessary and thus not performed.

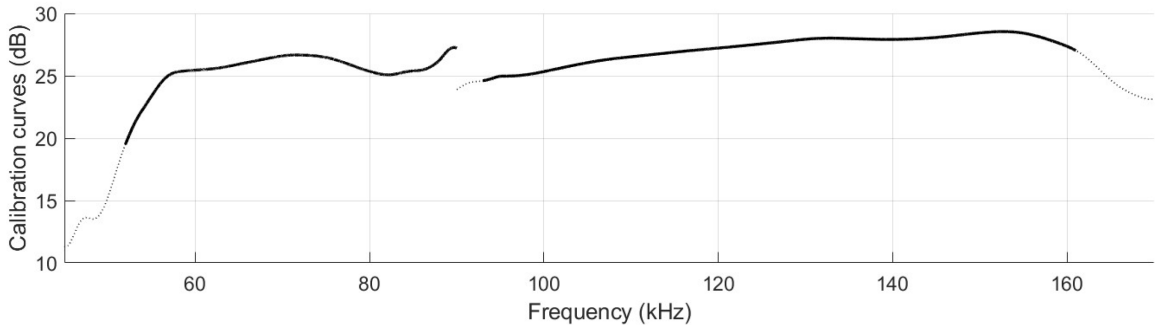

Figure 2.1 Calibration curves for ES70 and ES120 transducers [dB re 1 m^2]. Solid black sections of the curves indicate the frequency bands included in analyses. Dotted sections indicate tails of the frequency bands not included in analyses.

Table 2.1 Operational parameters for the echosounders used in this study.

	ES70-7CD	ES120-7CD
Pulse Duration (ms)	0.512	0.512
Decimated Sampling Frequency (ms)	0.016	0.008
Start Frequency (kHz)	45	90
End Frequency (kHz)	90	170
Power (W)	500	400
Ping Rate (Hz)	10	10

2.2.3 TS measurements of live jellies

Experimental measurements of live medusae were performed in August-September 2021. Nine sea nettles (each referred to as "Jelly #") were collected locally in Woods Hole, MA (41° 31' 26.136" N, 70° 40' 15.821" W). Buckets were used to scoop the medusae from beside a dock or from a boat. Because different species co-occur and identification is challenging (Bayha et al., 2017), DNA barcoding was conducted to confirm the identity of my specimens as *Chrysaora chesapeakei*[2]. The medusae were stored in buckets of seawater for up to 2 days in the lab, though acoustical measurements were taken either the same day the medusae were collected or the following day. Care was taken throughout the experiment to keep them fully submerged in seawater until after TS measurements were collected to avoid trapping air bubbles, which can contaminate acoustical measurements with their relatively strong scattering.

The medusae were too buoyant and motile to allow for free swimming measurements to be taken, so they were tethered in place and measurements were collected on just one individual at a time while fixed near the center of each transducer beam. The tether consisted of a piece of fishing line, which was strung on a needle and threaded through the central oral-aboral axis of the medusa. A steel shackle was tied to the end of the line to weigh it down such that the medusa would be oriented aboral (bell top) side up. The aboral end of the line was tied to the bottom of a ~2-m long loop of fishing line attached to the data acquisition system. Another piece of fishing line was tied to each side of the loop and was pulled and anchored to opposite sides of the tank, creating a wide "V" shape that acted as a barrier for the medusa as it pulsed upward (Fig. 2.2). This configuration of fishing lines and shackle allowed the medusa to remain stationary while pulsing and did not appear to affect its movements (see https://doi.org/10.1121/10.0019577 for example footage of a tethered, pulsing medusa in the test tank), and the two side-anchor lines were used to manipulate the position of the medusa. A 2'x2' piece of

black PVC was placed on the bottom of the tank as a background for the medusa to enhance visibility in the video footage. Acoustic TS measurements were collected using the single target detection tool in EK80 to verify that the medusa was located within around 2.5 degrees of the center of the beam. Corresponding down-looking video footage was collected simultaneously. Measurements were collected continuously for ~10 minutes per transducer while the medusa was pulsing at a rate of ~0.6 Hz (verified from video footage) to ensure that a sufficient number of echoes were recorded for the different flexion states of the animal.

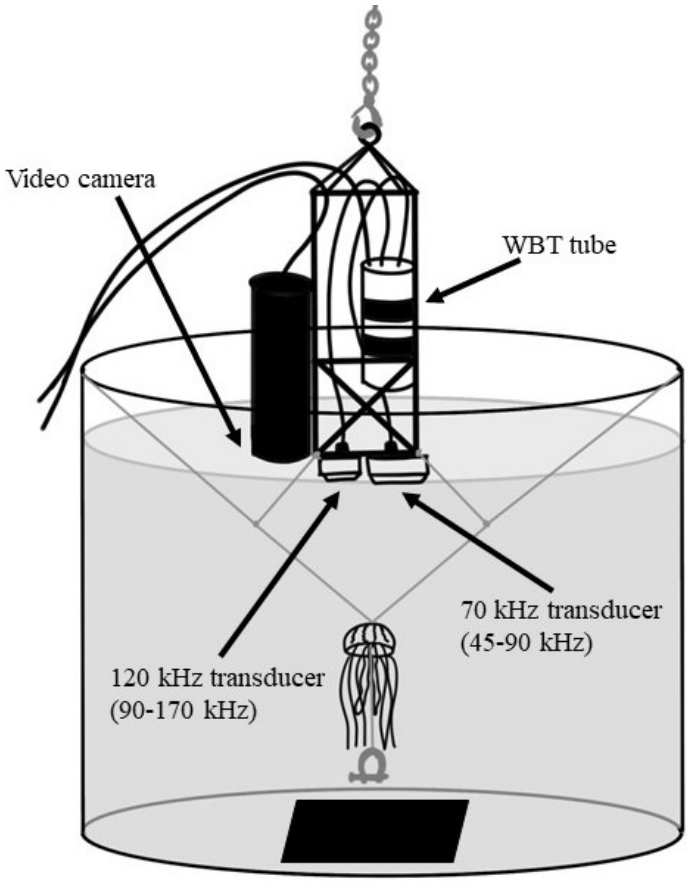

Figure 2.2 Schematic of experimental setup. The video camera and WBT Tube are connected to a power supply and the data acquisition laptop is located on a nearby lab bench. A medusa was tethered on a single strand of monofilament line, which was weighed down by a shackle. The line containing the medusa was tied to the bottom of a loop of line, which was tied to the data acquisition system. An additional piece of line was tied to each side of the loop and pulled and anchored to the sides of the tank to create a wide "V" that stopped the medusa from moving upward as it pulsed. The anchored lines were repositioned as necessary around the tank to center the medusa under each transducer. A rectangular sheet of opaque black PVC was placed at the bottom of the tank to serve as a high-contrast background for video footage.

2.2.4 Other measurements

The fineness ratio (ratio of bell height to bell diameter) was used to determine the relative dimensions of the medusa scattering model shape and was assumed to be consistent across all individual *C. chesapeakei.* A handheld GoPro was used to film a single medusa swimming, and frames where the organism was in its fully expanded and fully contracted positions were then imported to a photogrammetry software (ImageJ) and used to measure the diameter of the base of the bell and the height from the base to top of the bell for both swimming positions. This process was performed over a couple of swimming cycles and the average fineness ratios for each position were used to create the expanded and contracted medusa model shapes.

Size and material property measurements of the captured medusae were collected after acoustical measurements (Table 2.2). For Jellies #4-9, after acoustical measurements were collected, each medusa was removed from its tether, placed on a flat surface so its bell was fully expanded, and photographed next to a measuring tape. The photographs were imported to ImageJ and, because most of the individuals had an oval shape, the effective diameter was determined by averaging the major and minor axis lengths. The medusae were then transferred to the lab, where they were scooped out of their buckets with a soup ladle and drained of excess water, then placed flat in a clear container where they were photographed from the side with a ruler for scale. The images were imported to ImageJ and the bell thickness was measured digitally. The organisms were then weighed on a digital balance and transferred to a graduated cylinder to measure their volume, from which their tissue density was calculated. For Jellies #1-3, bell thickness was estimated using the best fit curve for thickness vs. diameter measured for Jellies #6-9.

Table 2.2 Size and material property parameters obtained for live jellies used in this study. The term 'ka' refers to the product of the product of the insonifying wavenumber, k, and the medusa's effective radius, a.

Jelly #	Diameter (cm)	Thickness (cm)	Frequency where ka = 1 (kHz)	g	h[a]
1	11.6	1.7[b]	4.2	-	1.026
3	11.7	1.8[b]	4.2	-	1.007
4	14.1	1.3	3.5	1.045	1.031
6	9.7	1.8	5.0	0.861	1.009
7	11.8	2.2	4.1	1.016	1.007
8	9.9	1.9	4.9	1.001	1.004
9	11.9	1.7	4.1	1.156	1.007

[a] Estimated by minimizing the sum of squares of the residuals between the measured and predicted TS over a range of values of h for other species of scyphomedusae (Table III).

[b] Estimated value using thickness vs. diameter best fit curve of other jellies.

A small clipping of tissue was taken for DNA barcoding (see supplementary material at https://doi.org/10.1121/10.0019577 for information regarding the DNA barcoding results), and the medusae were then archived in a -80°C freezer. Out of the nine individuals caught and measured, only seven were used in the analyses presented because Jelly #2 was damaged and Jelly #5 was contaminated with an air bubble under its bell during the acoustic measurements.

2.3 Data analysis

Raw voltage data from the transducers were pulse compressed (Lavery et al., 2010) and output as calibrated echograms. The pulse compressed data were averaged ping-by-ping over a 0.5-m interval containing the echo from the medusa and plotted as a function of time so that cyclical variations in TS were visible (Fig. 2.3.b). It was determined by cross-referencing time stamps in the acoustic data with video footage that peaks in the TS corresponded to the medusa's expanded position; smaller peaks ("subpeaks") were assumed to correlated with the contracted position (Fig. 2.3.a). Peaks and subpeaks across ~500 pings per individual were identified and converted to frequency spectra via the Fast Fourier Transform (FFT) of the corresponding pulse compressed pings (Fig. 2.3.c). FFT window lengths varied from 0.1-0.6 m depending on the duration of the medusa's echo in each frequency band, timing of echoes from the sides of the tank, and distance from the shackle weight below. For the expanded and contracted swimming positions, the calculated spectra, TS(f), were averaged in linear space to obtain a mean measured spectrum for comparison to model results.

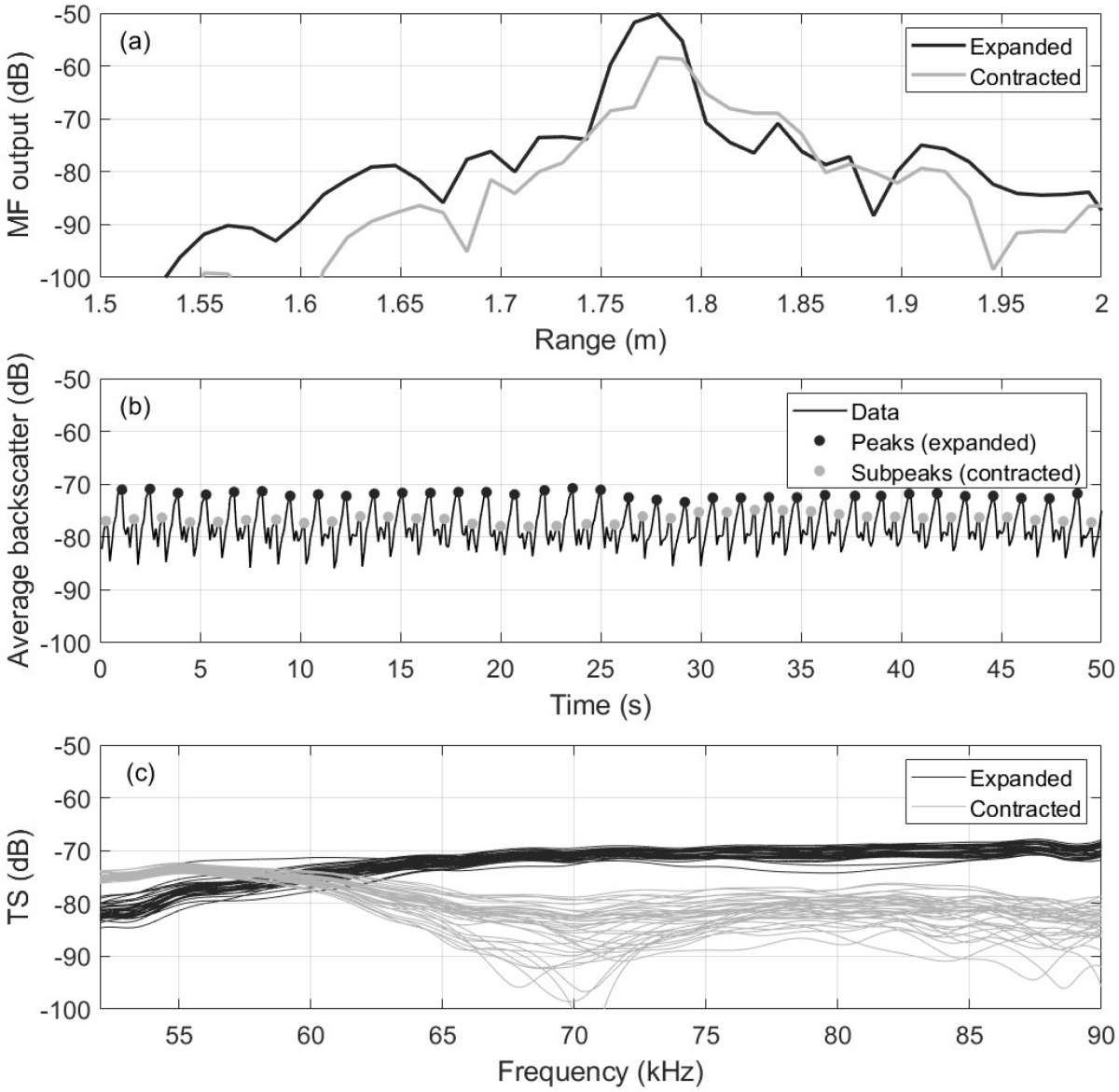

Figure 2.3 a) Calibrated matched filter (MF) output of echoes from Jelly #6 in the expanded and contracted bell positions at 70 kHz. b) Time series of averaged backscattering strength for Jelly #6, averaged from 1.5-2 m range in log space to aid in peak finding by enhancing differences between expanded and contracted positions. “Peaks” where the medusa’s bell was expanded, and “Subpeaks” where the bell was contracted, are indicated with black and gray dots, respectively. c) TS(f) spectra for the 52-90 kHz band for the expanded and contracted bell position, calculated from individual pings corresponding to the “Peaks” and “Subpeaks” identified in (b). All units are dB relative to 1 m^2.

2.4 Model theory

2.4.1 DWBA formulation

The scattering amplitude of an organism is a complex function of it size, shape, orientation, and material properties (density, ρ, and sound speed, c), as well as the incident wavelength. In cases where the organism's material properties are close to those of the surrounding medium, its scattering in the far field can be modeled using the Born approximation (Morse and Ingard, 1986). For the backscattering case (i.e., the present study), scattered energy is represented by the backscattering amplitude, L_{bs}, given by

$$L_{bs} = \frac{k_1^2}{4\pi} \iiint_{V'} (\gamma_\kappa - \gamma_\rho) e^{2i\vec{k}_{2i}\cdot\vec{r}'} dV' \tag{2.1}$$

where V' is the volume of the organism's body k_1 is the acoustic wavenumber of the incident wave ($k = 2\pi/\lambda$, where λ is the incident wavelength), $\vec{k}_{2i}$ is the incident wave vector evaluated inside the volume, and $\vec{r}'$ is the position vector for any volume element dV'. The material properties of the organism are reflected in the terms $\gamma_\kappa = (\kappa_2 - \kappa_1)/\kappa_1 = (1 - gh^2)/gh^2$ and $\gamma_\rho = (\rho_2 - \rho_{1)}/\rho_2 = (1 - g)/g$, where $\kappa_1 = 1/(\rho_1 c_1^2)$ and $\kappa_2 = 1/(\rho_2 c_2^2)$ are the compressibility of the surrounding medium's and organism's body, respectively; $g = \rho_2/\rho_1$ and $h = c_2/c_1$ are the density and sound speed contrasts. The material properties of the medusae in this study were assumed to be uniform, so these terms are constants and factored out of the integral. The evaluation of the volume integral over the wavenumber inside the organism ($\vec{k}_{2i}$ rather than $\vec{k}_{1i}$) is a modification of the Born Approximation referred to as the Distorted Wave Born Approximation (DWBA; Stanton et al., 1998).

Throughout this work, the far-field backscattered energy is expressed as the target strength (TS), given by

$$\mathrm{TS} = 10\log|L_{bs}|^2 \tag{2.2}$$

which has units of decibels (dB) relative to 1 m^2 (Urick, 1983). To compare scattering from multiple individuals, assuming similar morphologies and proportions, the TS was normalized by the unit area of the medusa's bell and thus expressed by the reduced target strength (RTS), given by

$$\mathrm{RTS} = 10\log\frac{|L_{bs}|^2}{\pi a^2} = 10\log|L_{bs}|^2 - 10\log\pi a^2. \tag{2.3}$$

The RTS is plotted against the product of the acoustic wavenumber and bell radius, 'ka', a dimensionless quantity representing the ratio of the characteristic size of an organism to the insonifying wavelength. The presentation of RTS as a function of ka allows for direct comparison of physical scattering processes irrespective of the actual target size or frequency used.

2.4.2 Scattering models for simple shapes

As part of the development of a novel scattering model shape to represent a medusa, DWBA models for simpler shapes were considered to determine what geometrical aspects would be important

to the overall scattering behavior of the medusa. For shapes with certain symmetries, Eq. (2.1) may be evaluated analytically or semi-analytically assuming homogeneous material properties and following the approach of Stanton and Chu (2000) to obtain an exact solution. Variations of weakly scattering spheres and finite cylinders were considered, as their solutions have been used as benchmarks for other scattering models for organisms (Jech et al., 2015). Evaluating Eq. (2.1) over a spherical geometry yields the closed-form backscattering amplitude of a fluid sphere:

$$L_{bs,sphere} = \frac{1}{8k_1}\left(\gamma_\kappa - \gamma_\rho\right) * [-2k_{2i}a\cos(2k_{2i}a) + \sin(2k_{2i}a)]. \tag{2.4}$$

A hemisphere consisting of one rounded face and one flat face was also derived. Evaluating Eq. (2.1) over half a sphere with an incident insonifying wave normal to the flat face of the hemisphere leads to the closed-form backscattering amplitude:

$$L_{bs,hemisphere} = \frac{\mathrm{k}_1}{4i}\left(\gamma_\kappa - \gamma_\rho\right) * \left[\frac{a^2}{2} + \frac{1}{4k_{2i}^2} + e^{-i2k_{2i}a}\left(\frac{a}{i2k_{2i}} - \frac{1}{4k_{2i}^2}\right)\right]. \tag{2.5}$$

Lastly, a thick disk or "puck" shape with two flat faces was considered. The puck is treated mathematically as an axially symmetric cylinder, so the result obtained by Stanton et al. (1998) was simplified for an end-on incident insonifying wave to obtain the backscattering amplitude:

$$L_{bs,puck} = \frac{k_1 a}{4}(\gamma_\kappa - \gamma_\rho)\int_{-\frac{L}{2}}^{\frac{L}{2}} e^{-i2k_{2i}l}dl \tag{2.6}$$

where the integral is evaluated computationally over the length of the cylinder, L. Comparisons between these three scattering models and the medusa model developed in this paper are discussed in the following section.

2.4.3 Medusa model shape

Certain symmetries (e.g., sphere, cylinder) give rise to a closed-form or reduced dimensionality integral expression for the DWBA formulation of f_{bs}. These analytical or semi-analytical solutions are convenient when it is reasonable to approximate the geometry of the organism with a simpler shape (e.g., Stanton et al., 1998). One must be cautious when making shape approximations, as over-approximating the shape of an organism could result in a loss of important scattering physics characteristics of that organism. For my target jellyfish species *C. chesapeakei,* an approximate medusa shape was created by stacking two partial spherical caps with different curvature, resulting in a radially symmetric volume with two interfaces (Fig. 2.4.a). The curvature of the faces was adjusted depending on the swimming position while conserving total volume. Scattering from the oral arms and tentacles was assumed to be negligible at the frequencies used in this study, so these appendages were not included in the model shape.

Because it has been observed that medusa TS varies cyclically with its swimming pulsations (Brierley et al., 2004), the shape of the model was tuned to reflect the width/height (W/H_{top}) ratio, or

fineness ratio, of the medusa's bell (Fig. 2.4.b). The mean fineness ratios for *C. chesapeakei* in its fully expanded and fully contracted positions (3.012 and 1.705, respectively) were obtained from side-angle video footage of a single individual swimming in the test tank, as well as the ratio of widths between the expanded and contracted positions ($W_e/W_c = 1.303$, obtained from video footage). All individuals of the same species were assumed to exhibit the same fineness ratios.

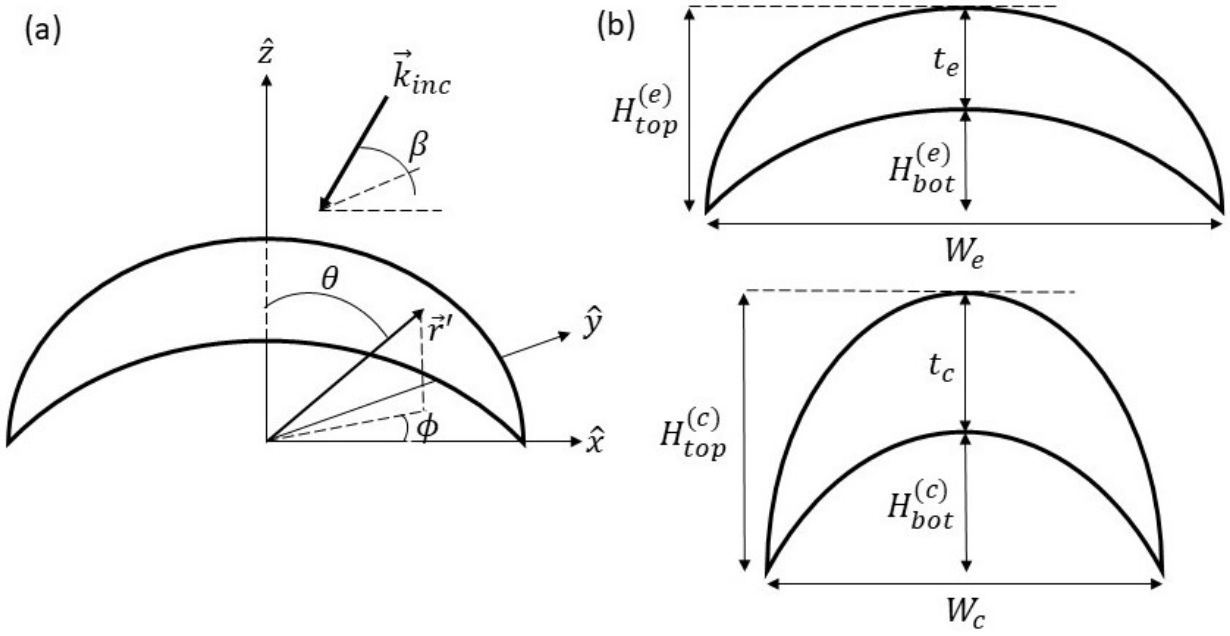

Figure 2.4 a) Scattering geometry used in the medusa scattering model. The $\hat{z}$ axis runs through the center of the bell. The bell is radially symmetric in the $\hat{x}$-$\hat{y}$ (ϕ) plane and the circular curves outline a two-dimensional cross-section in a constant ϕ plane. Broadside incidence corresponds to $\theta = 0°$, $\beta = 90°$, and $\beta = 270°$. b) Size parameters for expanded (upper) and contracted (lower) bell positions. Each arc forming the top/bottom (aboral/oral) face of the bell is a spherical cap.

The subscript 'e' and superscript '(e)' refer to the medusa's fully expanded position, while 'c' and '(c)' refer to the contracted position. For this study, the medusa's expanded bell diameter, W_e, and bell thickness, t_e, were measured directly, and the expanded fineness ratio and geometry of the shape were then used to estimate the heights of the top and bottom faces of the stacked spherical caps, $H_{top}^{(e)}$ and $H_{bot}^{(e)}$. From these values, the radius of curvature for each face was calculated and used to obtain the volume of the bell. The bell volume, contracted fineness ratio, and W_e/W_c ratio were then used to calculate the remaining size parameters for its fully contracted position (see Appendix A). For each swimming position, a numerically integrable 3-D model was constructed in MATLAB as a 3-D binary matrix with a pixel size of $W_e/200$, which could then be implemented in Eq. (2.1) to compute f_{bs} (See supplementary material at https://doi.org/10.1121/10.0019577 for medusa DWBA model MATLAB code).

2.4.4 Averages

Following the approach of Lavery et al. (2002) for predicting backscattering from krill, and because the live medusa TS measurements were averaged across multiple pings over multiple swimming cycles, the medusa scattering model was averaged over a normal distribution of bell thickness with the mean equal to the bell thickness measured from images and standard deviation set at 16% of the measured thickness. This standard deviation was selected after examining the relationship between the measured bell diameter and thickness, and then calculating the standard deviation of the residuals between the thickness predicted by this relationship and the actual measured thickness values.

Density measurements were averaged across Jellies #4-9 (no density measurements were taken for Jellies #1-3) to obtain an average value of the density contrast, g, for the scattering model. Measurements of the sound speed inside the medusae were not taken during the present study, so the sound speed contrast, h, was estimated for each individual by calculating the sum of squares of the residuals between the measured TS and predicted TS from a single realization of the scattering model at the measured bell thickness using a range of values of h previously measured for other species of scyphomedusae (Table 2.3). The h value corresponding to the minimum of the sum of squares was obtained from each individual and were averaged to obtain a mean h of 1.013.

Table 2.3 Material properties measured for scyphomedusae.

Species	g	h	Reference
Aurelia aurita	0.9808 0.989	1.0005 1.0001	Kang et al. (2012) Hirose et al. (2009)
Cyanea nozakii	1.073	1.038	Hirose et al. (2009)
Nemopilema nomurai	1.004	1.0008	Hirose et al. (2009)
Cyanea capillata	1.009	1.0004	Warren and Smith (2007)
Chysaora chesapeakei	1.0028[a]	1.013[b]	This study

[a] Average.

[b] Average estimate.

To examine the potential utility of this medusa scattering model for field-based volume scattering measurements of dense populations of medusae swimming randomly, the model was additionally averaged over a uniform distribution of fineness ratios ranging from fully expanded to fully contracted swimming positions and compared with measured TS across ~500 consecutive pings per individual. No averages were performed over swimming orientation because it was not a variable in the present study, however orientation dependence of scattering from medusae should be considered in future work. Following standard practice at the frequencies used in this study, only single scattering was assumed.

2.5 Results

2.5.1 Model predictions

Scattering predicted by the stacked spherical cap medusa model is considerably lower than that of the volume-equivalent sphere, hemisphere, and puck (Fig. 2.5). Scattering from the hemisphere and puck increases with frequency due to the presence of flat faces, which intercept an increasing proportion of incident energy with decreasing wavelength. Curved faces, on the other hand, direct a greater proportion of scattered energy away from the receiver, resulting in relatively flat scattering spectra as exhibited by the sphere and medusa (stacked spherical caps) models.

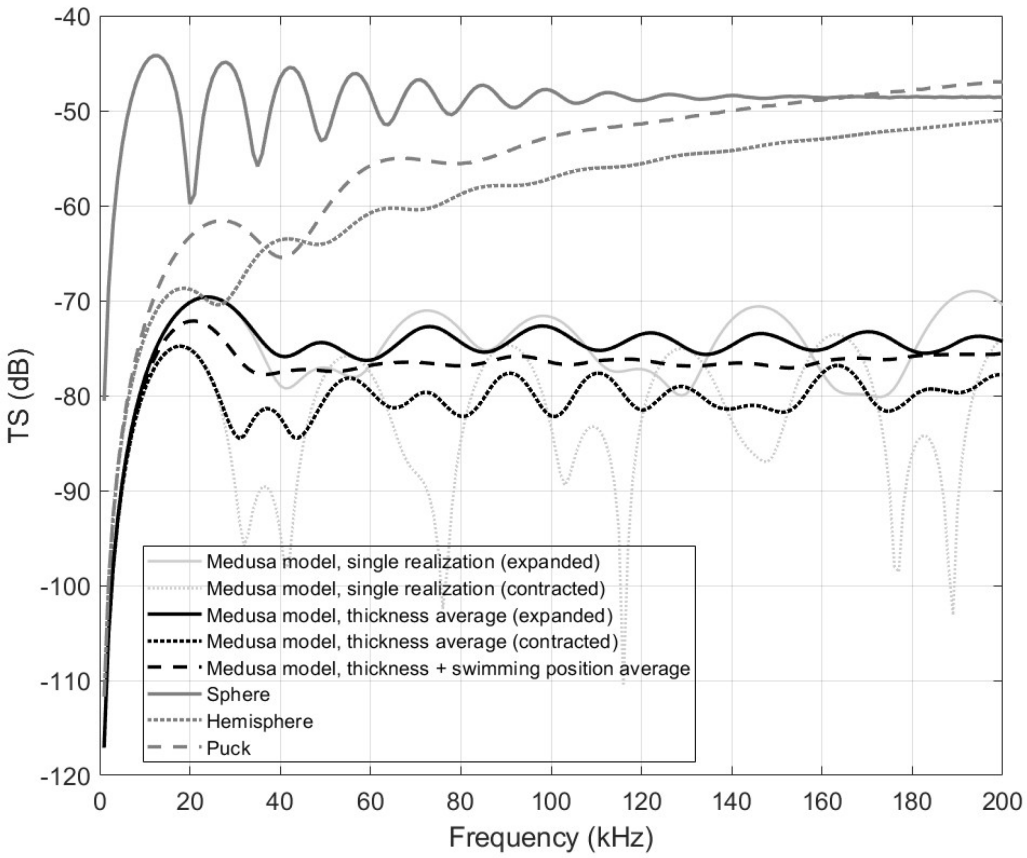

Figure 2.5 Predicted TS spectra for Jelly #6 for a single realization in both fully expanded and fully contracted swimming positions (expanded case has deep nulls) and an average of predicted TS over a normal distribution of bell thicknesses (mean 1.8 cm, standard deviation 0.29 cm) for both positions. Dashed black curve represents TS predicted over an average of thickness, plus an average over a uniform distribution of swimming positions ranging from fully expanded to fully contracted. TS spectra for a sphere, hemisphere, and puck (thick disk) shape have been averaged over the volume-equivalent size

distributions. The thickness of the puck shape is set to equal that of the medusa model and its corresponding radius is obtained from volume conservation.

In general, the medusa model predicts stronger scattering from the expanded position than from the contracted position. The TS spectrum peaks at the Rayleigh-geometric scattering transition (~18-22 kHz) and evens out in the geometric regime apart from null structure. Averaging over bell thickness has the effect of smoothing out some of the null structure in the model output, especially for the medusa's contracted position (Fig. 2.5). Additionally, averaging over a range of swimming positions further smooths the spectral null structure.

Although orientation dependence was not investigated experimentally in this study, the medusa scattering model predicts that scattering levels are dependent on the angle of incidence and that this relationship changes depending on the medusa's swimming position (Fig. 2.6). In the expanded position, scattering levels are relatively even up to incident angles ~18 degrees off broadside and drop off steeply at increasing angles. Scattering from the contracted position is maximized around 40 degrees off broadside and does not drop off at higher angles other than at nulls. Scattering from the expanded position is stronger than the contracted position near broadside; from ~30-60 degrees off broadside, both swimming positions exhibit similar scattering strengths. Above ~60 degrees off broadside, the contracted position exhibits stronger scattering.

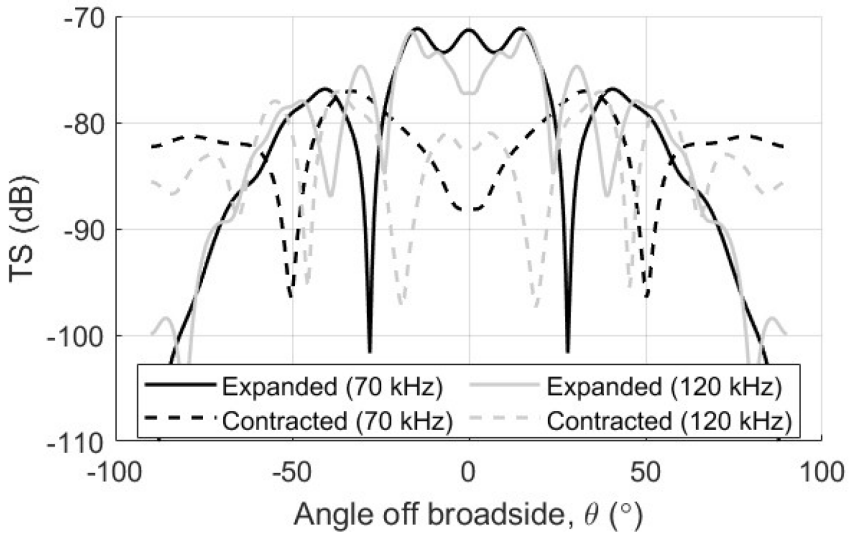

Figure 2.6 Predicted orientation dependence (TS vs. θ) for Jelly #6 over single model realizations (i.e., no averaging) of both its expanded and contracted positions. TS was calculated at 70 kHz and 120 kHz, the nominal center frequencies of the transducers used in the experimental portion of this study.

2.5.2 Model and data comparisons

Backscattering from seven individuals was measured in the present study. Despite all individuals being *C. chesapeakei*, RTS varied among individuals (Fig. 2.7), likely driven by variability in their material

properties. While the density contrast, g, was measured directly in this study, the value of h was inferred from the best fit between model and data. Average scattering levels predicted and measured in this investigation are well within the range of values in the literature for other species of scyphomedusae (Table 2.3), suggesting that the values of g and h obtained in this study for *C. chesapeakei* (Table 2.2) are reasonable and consistent with the material properties of other species of a similar body type (Fig. 2.8). However, there is still a high degree of variability between species and individuals.

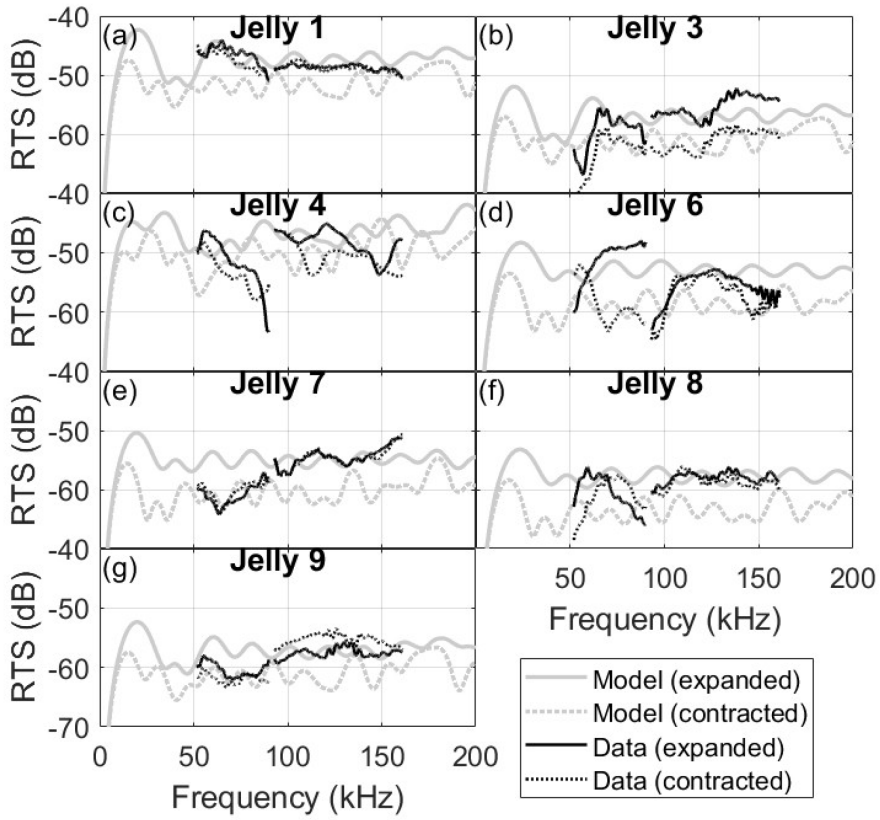

Figure 2.7 Comparison between model prediction and data for reduced TS vs frequency for all medusae measured, including both expanded and contracted swimming positions. Model has been averaged over a normal distribution of thicknesses; data have been averaged over pings identified as “Peaks” and “Subpeaks”, as described in the Data Analysis section. Breaks in the data occur between the 70 kHz and 120 kHz bands.

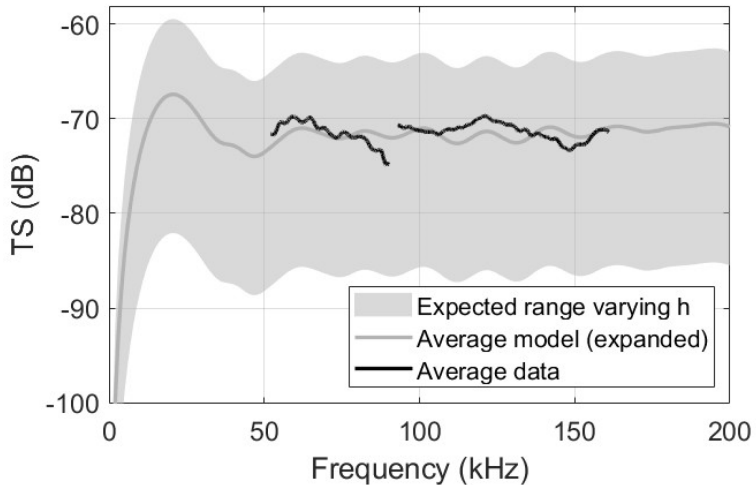

Figure 2.8 Comparison between predicted TS vs. frequency averaged across all seven live medusae (black curve) and model output averaged across all seven medusae (gray curve). Shaded region indicates a range of predicted possible scattering levels based on published values of h for other species (Table III).

Measured scattering from both the expanded and contracted swimming positions was similar, with scattering from the contracted position slightly lower in most cases (Fig 2.7). With the model averaged over thickness, position-dependent behavior of the scattering spectrum agreed better in the 70-kHz frequency band, especially for Jelly #6 (Fig. 2.7.d). Overall scattering levels were similar to those predicted by the model.

When averaged over both bell thickness and a uniform distribution of swimming positions, scattering levels predicted by the model agreed well with the data to within <2 dB except around nulls in the data (Fig. 2.9). In general, averages over swimming position smoothed out much of the null structure present in single realizations and thickness-averaged model predictions.

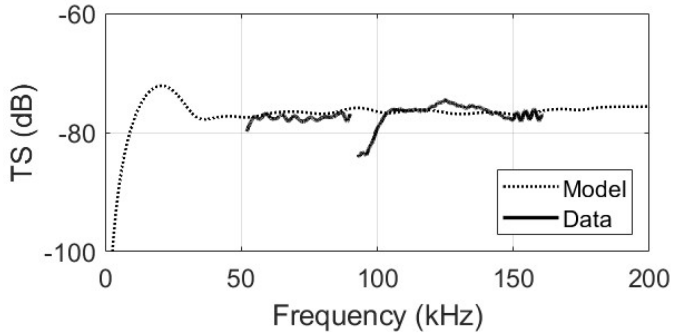

Figure 2.9 Comparison between model and data for TS vs. frequency for Jelly #6, averaged over swimming position. Model output was averaged over a normal distribution of thickness and a uniform

distribution of swimming position (i.e., fineness ratio) ranging from fully expanded to fully contracted. Data output has been averaged over all pings in a 50-second interval, capturing the full range of swimming positions. Roll-off below 102 kHz is due to the presence of a null in the data at the low end of the 120 kHz frequency band.

2.6 Discussion

2.6.1 Comparison with published data

A primary finding of the modeling portion of this study is that the spectral behavior of broadband scattering is significantly impacted by the position of its bell during its swimming pulsations, and this is supported particularly by observed scattering in the 70 kHz band. Furthermore, scattering levels are higher overall in the bell's expanded position than its contracted position. This makes sense because the greater curvature in the bell in its contracted state would direct a greater proportion of scattered energy away from the direction of the receiver. Swimming-dependent scattering behavior in the data was more pronounced in the 70 kHz band than in the 120 kHz band, possibly since smaller wavelengths are more sensitive to roughness and fine-scale structure inside the medusa's bell, and their scattering processes are consequently more complex than scattering of larger wavelengths, which are less impacted by small-scale contributions. On the other hand, higher frequencies would be more sensitive to the curvature of the top face of the bell, complicating the interpretation. Investigation of swimming pulsation effects on scattering in the Rayleigh regime would require use of frequencies lower than those used commonly for oceanographic applications (Table 2.2).

Another finding from this study is that there is a prominent peak in the modeled TS as the scattering regime transitions from Rayleigh to geometric, around 20 kHz (a bit higher for the expanded swimming position and lower for the contracted position due to the contracted bell being thicker than the expanded bell). This corresponds to a wavelength of ~7.5 cm, or a quarter wavelength of ~1.9 cm. This is close to the measured thickness of the live medusa's bell (Table 2.2), and where the first peak in TS would be expected to occur due to constructive interference between reflections off the aboral and oral (i.e., top and bottom, respectively) faces of the bell. The range of frequencies used in this study were too high to verify this result experimentally; future studies might add 18 and 38 kHz transducers to capture this peak, especially as these frequencies are routine for fisheries applications. A larger test tank would be needed for lower frequencies to remain in the far-field and minimize interference from the surface and sides of the tank.

The average TS of *C. chesapeakei* measured in this study is well within previously observed (narrowband) scattering levels for scyphomedusae (Fig. 2.10). It is important to note that RTS – essentially a measure of scattering strength per unit projected surface area of the bell – varies vastly between studies, indicating that more subtle differences in species shape and material properties could have significant impacts on scattering levels. Material properties are encapsulated in density and sound speed contrasts (g and h, respectively), which need to be determined experimentally. Measurements of g may be obtained using commonplace laboratory equipment, though with some uncertainty; h is more difficult to measure directly and requires a specialized lab setup to measure the speed of sound through animal tissue. Observed variability in scattering strength highlights the need for species-specific

measurements of these parameters, and potentially more complex representations that account for variation in material properties between different types of tissues in a single organism.

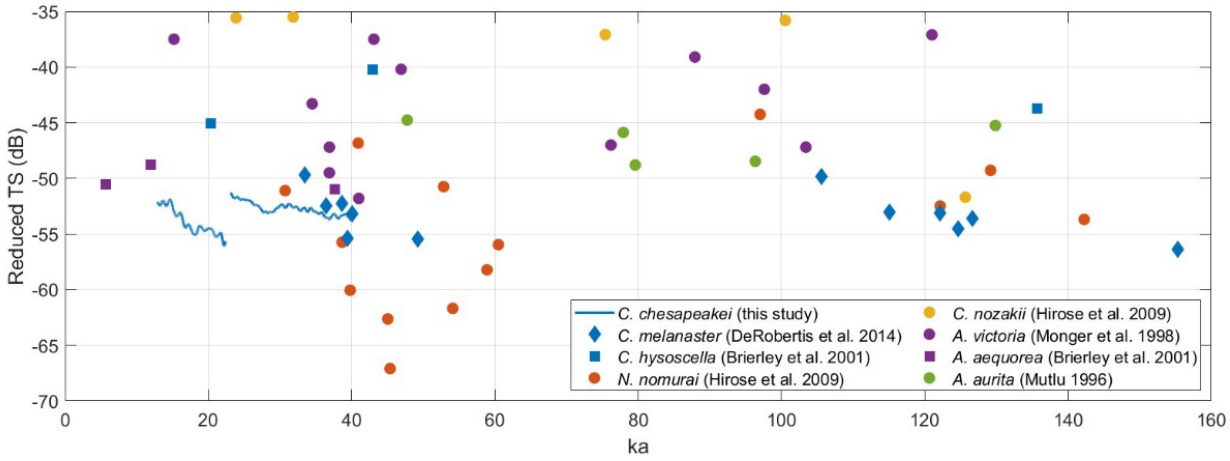

Figure 2.10 Reduced TS vs. ka data from this study (averaged over all seven live medusae) and previous studies on other species. Because physical properties vary between species, data points are colored by genus to aid in comparison. Notably, species belonging to the genus *Chrysaora* are in blue for comparison with results of the present study.

Within this study, a wide range of TS levels were measured across individual medusae (Fig. 2.7), even after normalizing for size. This shows that individuals even within a single species might vary in their material properties, and/or that *C. chesapeakei* vary in their body proportions. The material and morphological properties of *C. chesapeakei* may also change throughout the life cycle as individuals grow and mature (Bayha et al., 2017). A larger sample size would be needed to investigate both potential sources in TS variability between individuals. Compared to TS measurements for species of the same genus (*Chrysaora*; blue in Fig. 2.10), the average measurements presented in this study agree well, especially with the published measurements for *Chrysaora melanaster* (De Robertis and Taylor, 2014), suggesting that a single model might be used to represent more than one species within a limited scope, provided that the model is averaged over thickness and swimming position.

2.6.2 Recommendations for field applications

As mentioned above, the measurements presented in this study were taken at frequencies in the geometric scattering regime of these medusae. Thus, one cannot expect that TS will scale linearly with body size and consequently cannot directly infer biomass from backscattering measurements at these frequencies. The frequency dependence of TS must be known in order to obtain quantitative estimates from volume scattering from a population of medusae, and future studies should consider the effects of size and maturity of medusae on TS.

The model predicted that at incident angles near broadside, TS predictions were relatively stable, but TS fell off steeply off-broadside in the expanded swimming position. Both the expanded and contracted positions exhibited deep null structure in their orientation dependence. Given uncertainties in the swimming orientation of medusae in the field, it is important that future studies experimentally examine the effect of orientation on scattering strength and include averages over orientation in model predictions when orientation cannot be directly observed. Assuming all medusae in a swarm do not pulse in sync and are thus in random swimming positions at a given moment, it is also critical that model predictions for field-based studies incorporate averages over swimming positions.

2.7 Conclusion

In summary, a scattering model for medusae has been developed based on the Distorted Wave Born Approximation and an approximate medusa bell shape formed by two stacked spherical caps and a homogeneous volume. This model was applied to a species of sea nettle, *C. chesapeakei*, representing a common morphology of scyphomedusae. Controlled, broadband TS measurements of live individuals were obtained and compared to model predictions averaged over bell thickness. Overall scattering levels agreed reasonably between the model and data. Both the model and data exhibited differences in spectral scattering behavior depending on changes in bell shape throughout the medusa's swimming pulsations, with scattering levels maximized in the bell's fully expanded state. When averaged over swimming position, TS measurements and TS predictions were in good agreement, indicating that the medusa model more accurately captures the relevant scattering physics than the simpler models based on canonical shapes. Even though the sphere, hemisphere, and puck shapes are significantly less computationally expensive than the full 3-D DWBA model, these shapes resulted in prediction errors of up to ~30 dB at the frequencies used in this study, while the DWBA model more closely described the scattering levels observed in the experimental measurements.

There remains uncertainty in the material properties of *C. chesapeakei*, as its sound speed was not measured directly in this study. Backscattering strength of live medusae measured in this experiment exhibited a high degree of variability between individuals, suggesting that there may not be such thing as a "one size fits all" medusa scattering model. This highlights the importance of averaging model predictions to reflect natural variability in the field. Averages could be fine-tuned in a future field-based study by collecting measurements of bell size parameters in addition to backscattering when *C. chesapeakei* is abundant in the late summer.

One of the main advantages of the model presented here is that it can be easily tuned to reflect the size, shape, and material properties of other species. The DWBA framework is a powerful tool for developing scattering models for gelatinous organisms. Further development on this and similar models is a crucial step toward being able to quantify jellies rapidly and remotely in the ocean, both for ecosystem monitoring purposes and for gaining a better understanding of the global distribution of gelatinous biomass.

3 Measuring the bubble size distribution in an estuarine front via broadband excess attenuation

3.1 Introduction

Where river discharge and ambient coastal waters meet, relatively strong surface salinity and velocity gradients are common. These frontal features give rise to sustained downwelling currents (Marmorino and Trump, 1996; O'Donnell et al., 1998) that play a role in enhanced localized surface wave breaking and the generation of bubbles (Baschek et al., 2006; Thomson et al., 2014). Foam lines associated with frontal features are a commonly observed surface expression associated with these processes. The role of fronts in air-sea gas exchange is not well understood, however observations by Baschek et al. (2006) suggest that frontal features in the Strait of Georgia, BC, Canada, an environment with strong bathymetric forcing, are responsible for a significant portion of the aeration of coastal waters. The influence of fronts on other estuarine environments is far more uncertain, and the ability to quantify oceanic bubble densities and size distributions is crucial for understanding their role in air-sea gas exchange (Baschek et al., 2006).

While the open ocean impacts of bubbles have been considered, the same cannot be said for coastal systems where frontal dynamics cultivate dense, but highly localized, bubble plumes. Acoustics, both in echosounders and ADCPs, have been used for decades to image fronts (Kilcher and Nash, 2010; Marmorino and Trump, 1996; Marston et al., 2023; Nash and Moum, 2005; Sarabun, 1993), but the impacts of frontal features on size, spatial, and temporal distributions of bubbles are not well-studied. Near-surface bubbles can interfere with the propagation of acoustic signals due to their high extinction and bubble-induced sound speed variability (Dahl et al., 2008). These issues are expected to be significant at frequencies below 120 kHz based on estuarine and open ocean observations (Bassett and Lavery, 2021; Trevorrow, 2003). While these studies suggest that bubble plumes impact acoustic propagation in the presence of near-surface bubble clouds, others suggest positive impacts as the bubble clouds can ameliorate the rapidly varying acoustic focusing and reverberation effects introduced by the curvature of surface wave crests, thereby effectively shielding signals of certain frequencies from the complications of rough surface scattering (Deane et al., 2013; Preisig and Deane, 2004). Less is known about the distributions of bubbles in nearshore and estuarine environments, and the impact of entrained bubbles on acoustic communications and sonar performance is poorly constrained. Nonetheless, studies by Bassett and Lavery (2021) and Preisig (2007; and references therein) suggest that bubbles generated by breaking waves at the sea surface can contribute to acoustic transmission loss in coastal environments. The impact of bubbles on transmission loss cannot be predicted without first understanding the bubble populations in these environments. This study aims to acoustically quantify the density and size distribution of bubbles associated with the frontal boundary of the Connecticut River tidal ebb plume.

Breaking waves inject small bubbles into the upper ocean. In the absence of downwelling currents (i.e., open ocean), these bubbles form plumes that extend to depths ranging from 2-15 m for

durations ranging from 20-90 seconds (Trevorrow, 2003), and the density of bubbles decays exponentially with depth (Baldy and Bourguel, 1985; Crawford and Farmer, 1987; Medwin, 1970). Following a wave breaking event, the bubble plume will persist locally while bubbles dissolve or rise to the surface (Chua et al., 2021). Deeper plumes and stronger sound scattering are associated with higher wind speeds (Dahl, 2003; Thorpe, 1984). In contrast to the open ocean, even on a calm day with little wind-driven surface wave action, a front can generate an acoustically significant population of bubbles (Baschek et al., 2006; Bassett and Lavery, 2021). Additionally, localized downwelling in a front provides a mechanism by which bubbles can be entrained to much greater depths than they would be due to wave breaking alone. Baschek et al. (2006) provide one such example in a coastal front associated with strong bathymetric forcing entraining bubbles to 105 m depth. In environments with strong currents, as is often the case with estuarine fronts, bubbles injected into the upper water column and subsequently entrained to greater depths by downwelling are then advected (Bassett et al., 2023). These processes can create relatively dense plumes of bubbles extending farther from the front than the narrow foam lines on the surface indicate (Baschek et al., 2006; Bassett and Lavery, 2021; Kilcher and Nash, 2010). The currents driving the bubble distribution at the Connecticut River frontal boundary were described by Garvine (1977) and Garvine and Monk (1974; Fig. 3.1).

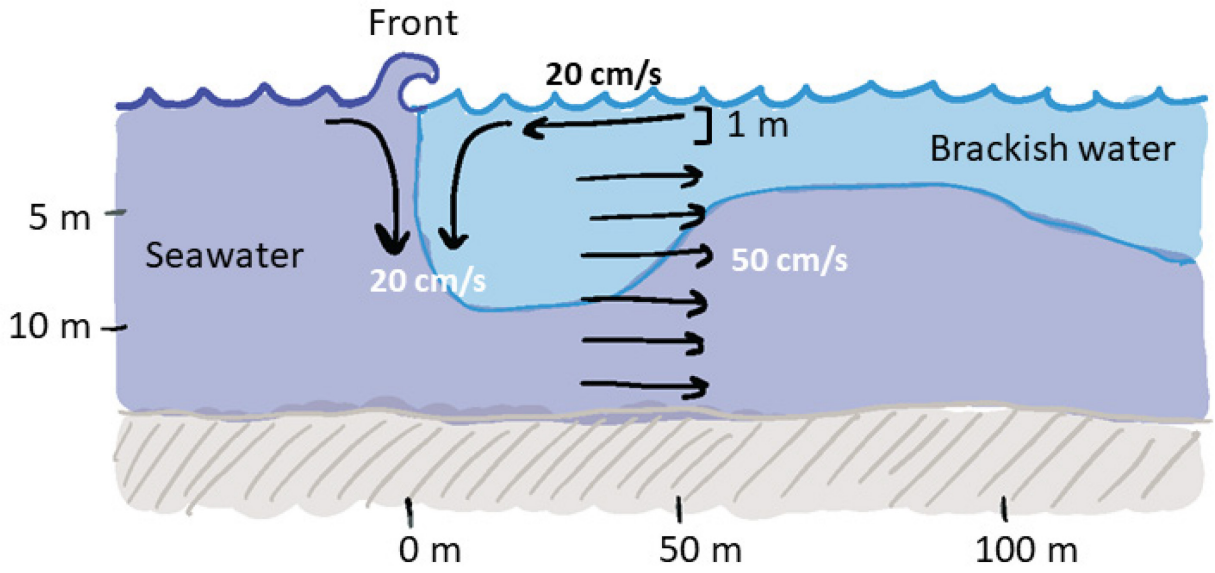

Figure 3.1 Conceptual schematic the frontal boundary of the Connecticut River plume during the ebb portion of the tidal cycle. Horizontal distances are relative to the front. Synthesized from observations of Garvine (1977) and Garvine and Monk (1974).

The frontal structure and turbulent mixing of the Connecticut River plume were described in detail by Delatolas et al. (2023). The internal structure of the front resembles a density-driven gravity current, and there is strong downwelling at the front with a rotating cell ~10 m wide. They also observed a buoyant layer at the surface accelerating toward the front, similar to observations by Garvine (1977)

and Garvine and Monk (1974) as well as frontal circulation patterns observed in the Leschenault estuary (Luketina and Imberger, 1987) and the Chesapeake Bay estuary (Marmorino and Trump, 2000). The authors' observations suggest that turbulence in the frontal head consisting of the downwelling zone and rotating cell is primarily driven by convective instabilities, and that this turbulence is isotropic and strong compared to elsewhere relative to the front. Beyond the frontal head up to 100 m away is a mixing layer driven by Kelvin-Helmholtz instabilities at the interface between the brackish river outflow and ambient seawater. Turbulence diminished beyond 100 m where stratification was stable enough to suppress the formation of instabilities (Delatolas et al., 2023). Bubbles entrained by downwelling at the front are subject to the hydrodynamics driving flow at and near the front. While Delatolas et al. (2023) did not attempt to characterize the bubble population associated with the front, their observations provide important context for understanding what drives the bubble size distribution.

Baschek et al. (2006) estimated that frontal features in the Fraser River estuary (BC, Canada) contribute ~8% of air-sea gas exchange in the area, with a single tidal front at Boundary Pass contributing 3%. While this dissertation does not attempt to estimate the proportion of gas exchange facilitated by the ebb plume front of the Connecticut River, it is important to note that the two locations provide very different contexts for estimating bubble size distributions; quantitative estimates for the Fraser River estuary may not translate directly to processes in the Connecticut River estuary. The Boundary Pass front is a bathymetrically forced system formed by flow over a sill, while the Connecticut River front is formed by the ebb plume expanding over denser ambient seawater. Consequently, the Boundary Pass front has associated downwelling currents with velocities up to 0.75 m/s carrying bubbles to depths up to 160 m (Baschek et al., 2006), while the Connecticut River front has downwelling velocities around 0.2 m/s carrying bubbles to depths up to nearly 4 m (Marston et al., 2023). The Boundary Pass front is larger and more strongly forced, potentially resulting in more bubbles dissolved and facilitating a higher proportion of air-sea gas exchange than the Connecticut River front. Thus, comparisons between the two environments must be made with caution.

Since scattering from bubbles is characterized by a strong resonance peak (Medwin and Clay, 1998), acoustical techniques often seek to exploit this feature over multiple frequencies to obtain estimates of bubble size distributions and densities. This investigation focused on a) the development of a broadband bubble measurement system that uses excess attenuation to infer bubble size distributions, b) characterizing the performance of the system by measuring bubble size distributions in a laboratory environment, and c) measuring a tidal front bubble size distribution in the field. The measurement system was based on the system developed by Terrill & Melville (2000) and built on a towable frame for field deployments. To obtain observations of bubbles in a laboratory setting, the system was deployed in a wave tank. Measurements of broadband excess attenuation were inverted using an iterative method (Caruthers et al., 1999) to obtain estimates of bubble size distributions. The lab measurements were then used as a basis for the analysis and interpretation of field measurements, where the system was towed beside a research vessel. This chapter describes the towable bubble measurement system and observations of the evolution of a bubble size distribution in the lab as well as in a tidal front.

Past studies have used a wide variety of acoustical and optical techniques to quantify bubbles of sizes ranging from microns to centimeters (Fig. 3.2) , many of which employed more than one technique simultaneously to account for their different advantages and capabilities (Vagle and Farmer, 1998a). Early work to measure bubbles optically include the photographic approach of Johnson & Cooke (1979), which produced some of the first widely accepted measurements of bubble size distributions under breaking waves. Baldy and Bourguel (1985) iterated on those measurements using a laser-based single-

particle scattering technique. More recent developments in optical bubble measurements include the use of holographic imaging (Liu et al., 2013; Tian et al., 2010) and the use of fiber-optic probes (Blenkinsopp and Chaplin, 2010; Rojas and Loewen, 2007). Acoustical techniques typically infer information about bubbles via scattering and attenuation measurements. Vagle and Farmer (1992) described a backscatter technique for measuring bubbles using up-looking transducers to obtain vertical profiles of bubble size distributions in the open ocean. Farmer et al. (1998) later developed a free-flooding acoustical resonator for bubble measurements with a metric for data quality, followed by the development of a sound velocimeter by Terrill and Melville (2000), which measured attenuation and dispersion of a broadband signal that can be inverted to obtain information about bubbles in the propagation path. These acoustical studies used either a series of narrow-band signals or a broadband signal that was processed in narrow-band sections using the method of Commander and McDonald (1991).

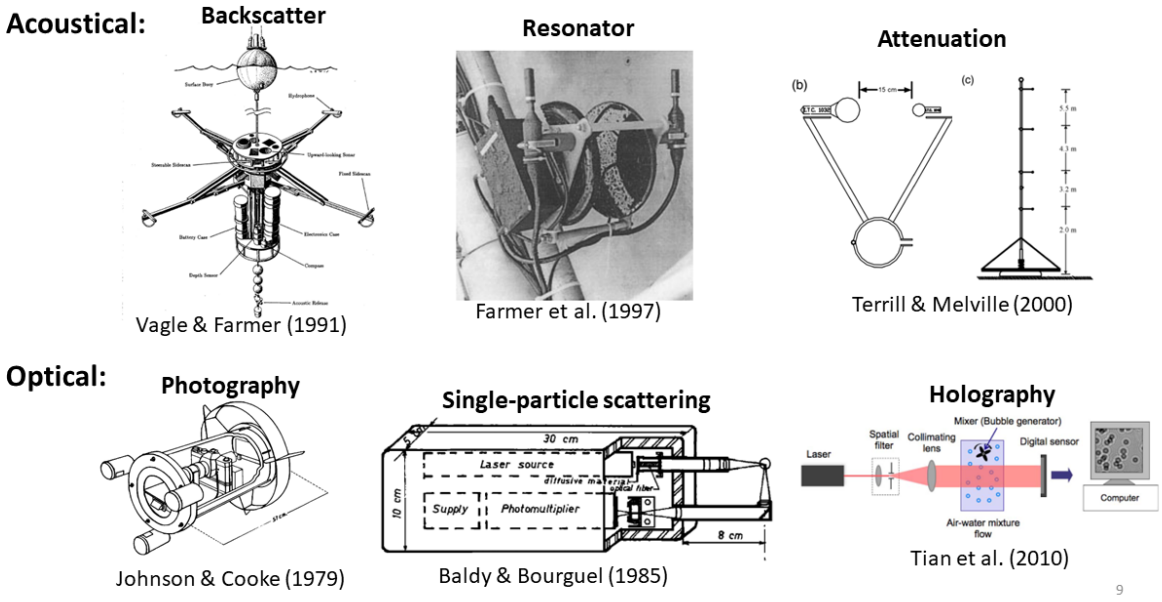

Figure 3.2 Examples of acoustical and optical instruments developed to measure bubble size distributions.

Oceanic bubble size distributions generally follow a power law with a slope steepening above a value called the Hinze scale, which divides bubbles large enough to fragment in turbulent flow from bubbles small enough to be stabilized by surface tension (Hinze, 1955). The Hinze scale for saltwater bubbles under breaking waves depends on the turbulent dissipation rate within the breaking wave crest and has been reported to be ~1 mm radius (Deane and Stokes, 2002). The value where the power law steepens decreases with time as larger bubbles rise to the surface (Harb and Foroutan, 2019). Despite bubble entrainment accounting for 30 to 50% of the total energy dissipated by a breaking wave, 95% of initially entrained air volume is lost within one wave period of the breaking event (Lamarre, 1993). For plunging breakers 10 cm in height in seawater, the life of a wave-generated bubble plume consists of an

approximately 2-second long acoustically active phase when bubbles are generated and fragmented, followed by an acoustically quiescent phase where the bubbles are subject to processes over a wide range of timescales including turbulent diffusion, advection, dissolution, and rising due to buoyancy (Deane and Stokes, 2002).

Multiple studies have reported quiescent bubble size distributions under breaking waves in the lab and in the open ocean (see references two paragraphs earlier) yet there have been few attempts to describe the bubble size distributions in estuarine tidal fronts (Baschek et al., 2006; Bassett and Lavery, 2021; Reeder et al., 2022). In addition to the different hydrodynamics driving the distribution of bubbles in a front versus under breaking waves, there are uncertainties in the frontal bubble size distribution due to the sharp salinity gradient. Salinity has a significant impact on the density of submillimeter bubbles generated by breaking waves, with densities in saltwater exceeding those in freshwater by up to an order of magnitude (Cartmill and Yang Su, 1993; Harb and Foroutan, 2019).

Here I present estimates of the bubble size distribution obtained from measurements of broadband excess attenuation collected by a towed instrument. First, I describe a controlled laboratory experiment where bubbles generated by a single breaking wave in a tank filled with artificial seawater were measured. Then, I present bubble size distributions observed in the Connecticut River ebb plume front at a couple of depths. There were some key differences between the laboratory tank and field settings that may have impacted the observed bubble size distributions in each setting. Bubbles in the wave tank were not subject to ambient currents or circulation, so the bubble size distribution changed predictably as larger bubbles were lost to buoyant degassing, whereas in the field there were sustained downwelling and turbulence associated with the front that deepened the bubble cloud and may have kept bubbles entrained for a longer period. Also, each replicate of the laboratory experiment consisted of a single wave breaking event followed by a rest period to let the bubbles dissipate, while the field measurements were taken in windy conditions with continuously breaking waves at the surface injecting new bubbles into a sustained bubble cloud. Additionally, the physical properties of the water in the laboratory tank were homogeneous, while the front is in a highly stratified environment with a combination of seawater and brackish water driving the bubble population.

3.2 Relevant theory

Excess attenuation is defined as the attenuation of an acoustic signal due solely to scattering and absorption from bubbles and is obtained by taking the difference in log space between the measured attenuation of a signal in a bubble-free medium with the attenuation of the same signal propagating through a bubbly medium. The excess attenuation of a bubble population is straightforward to measure, however converting a measurement to a bubble size distribution can be complicated. The relevant theory for estimating bubble size distributions from excess attenuation is explained by Caruthers et al. (1999; and references therein) and is briefly summarized as follows.

The predicted attenuation for a given bubble size distribution is expressed as

$$\beta_{thoery}(\omega) = \frac{2\pi c_0}{\omega} \int_0^\infty \frac{a\ \delta\ n(a) da}{(\omega_R^2/\omega^2 - 1)^2 + \delta^2} \tag{3.1}$$

where the attenuation coefficient $\beta_{theory}(\omega)$ is in nepers per meter, c_0 is the sound speed of bubble-free seawater, ω is the angular frequency of the transmitted pulse, a is the bubble radius, δ is the damping parameter (Eq. (9-19) in Vagle and Farmer, 1992), $n(a)da$ is the number of bubbles per unit volume $n(a)$ within a radius increment da, and ω_R is the resonance frequency of a bubble with radius a. This expression for the excess attenuation due to bubbles is referred to as the "formal theory." Given that $\omega = 2\pi f$, the resonance frequency of a bubble of radius a_R (in meters) is approximately

$$f_R \approx \frac{1}{2\pi a_R}\left(\frac{3\kappa\bar{p}\left(1+\frac{2\sigma}{\bar{p}a_R}\right)}{\rho} - \frac{2\sigma}{\rho a_R}\right)^{\frac{1}{2}} \tag{3.2}$$

where $\bar{p} = p_0 + \rho g|d|$ is the seawater pressure at the depth d of the bubble, p_0 is atmospheric pressure, g is gravitational acceleration, ρ is the seawater density, $\kappa \approx 1.4$ is the polytropic index of air, and σ is the surface tension (Deane et al., 2013).

Attempting to solve Eq. (3.1) for $n(a)$ leads to an ill-conditioned problem, so the following assumptions are made: 1) the total damping parameter δ – which depends on thermal conductivity, sheer viscosity, and surface tension – is set constant at its value at resonance (Medwin, 1977), 2) only bubbles insonified by their resonance frequency contribute significantly to attenuation (i.e., $\omega_R^2/\omega^2 = 1$), and 3) the bubble distribution changes slowly about the resonant radius (i.e., $n(a) = n(a_R)$ = constant). These assumptions lead to a simplified version of Eq. 3.1 that can be inverted to obtain $n(a)$:

$$n(a) \approx (1+0.1z)^{-1} 4.6 \times 10^{-6} f^3 \alpha_{meas}(f) \tag{3.3}$$

where z is the depth of measurement in meters (accounting for the pressure-dependent relationship between bubble radius and resonant frequency), f is the resonance frequency for bubbles of radius a, and $\alpha_{meas}(f)$ is the measured excess attenuation in dB/m. This simplified relationship between attenuation and bubble size distribution is referred to as the Resonant Bubble Approximation (RBA). The RBA can be applied to bubble distributions that follow a power law, but it must be used with caution because its negligence of off-resonance contributions to attenuation can result in overestimations of small bubbles.

Caruthers et al. (1999) describes an iterative method for obtaining $n(a)$ from the measured $\alpha_{meas}(f)$. For a single iteration, Eq. (3.3) is used to calculate an estimated bubble distribution. This distribution is then fed into Eq. (3.1) to obtain the predicted excess attenuation coefficient, which differs from $\alpha_{meas}(f)$ by an error. This attenuation error is then fed into Eq. (3.3) to yield an error in the bubble distribution, which is then added to the estimated bubble distribution to yield a first-order corrected bubble distribution, thus completing one iteration. The corrected bubble distribution may then be fed back into Eq. (3.1) to obtain a new predicted excess attenuation coefficient, the error is calculated between the new predicted excess attenuation and $\alpha_{meas}(f)$, and the process is repeated as the predicted excess attenuation converges on $\alpha_{meas}(f)$. In this study, multiple iterations were needed to get a solution that had good agreement with $\alpha_{meas}(f)$ but with minimal enhancement of artifacts and discontinuities in the corresponding $n(a)$.

3.3 System description

The measurement system consisted of a low-frequency (3-30 kHz) omnidirectional source (Gavial ITC-1001), a mid-frequency (30-110 kHz) omnidirectional source (Gavial ITC-1042), and two omnidirectional receiving hydrophones (Teledyne/Reason TC4014-5). All four components were mounted inline on a custom aluminum frame with the two hydrophones approximately evenly spaced in between the two sources with ~20 cm distance between each component (Fig. 3.3.a). This configuration was originally chosen to provide greater flexibility and dynamic range between the sources and receivers as multiple transmission paths could be probed. However, the quality of measurements using this configuration is limited to the appropriate spacing between sources and receivers and balance with transmitted power for the anticipated attenuation from the sampling volume. In my applications, SNR was maximized at each signal's arrival at its closest hydrophone, as these received signals were subject to the least transmission loss. During field deployment (Section 3.7), the received mid-frequency signal was saturated due to the transmitted power being too high.

The sources were connected to a dual channel power amplifier (Pioneer GM-A5702), then an 8-channel audio interface (National Instruments USB-6366; 8 analog inputs, 2 analog outputs). The hydrophones were each connected to a 1 kHz high-pass filter (Thorlabs EF111) and then to the same audio interface (Fig. 3.3.b). When deployed in shallow water, changes in the depth of the instrument due to surface waves resulted in strong, low-frequency pressure signals associated with the phase of the waves, and these were found to saturate measured acoustic signals. The high-pass filter was included to reduce these pressure signals. The audio interface was then connected via USB to a control and logging computer (SimplyNUC LLM1V8SQ) running a MATLAB script to operate the system. The hydrophones and power amplifier were powered by a single 12 V power supply (BK Precision 1902B), which was connected to 120 VAC power along with the audio interface and logging computer. The instrument's sampling abilities were limited by the writing speed of the data acquisition laptop, and different sampling methods were used in the laboratory and field experiments.

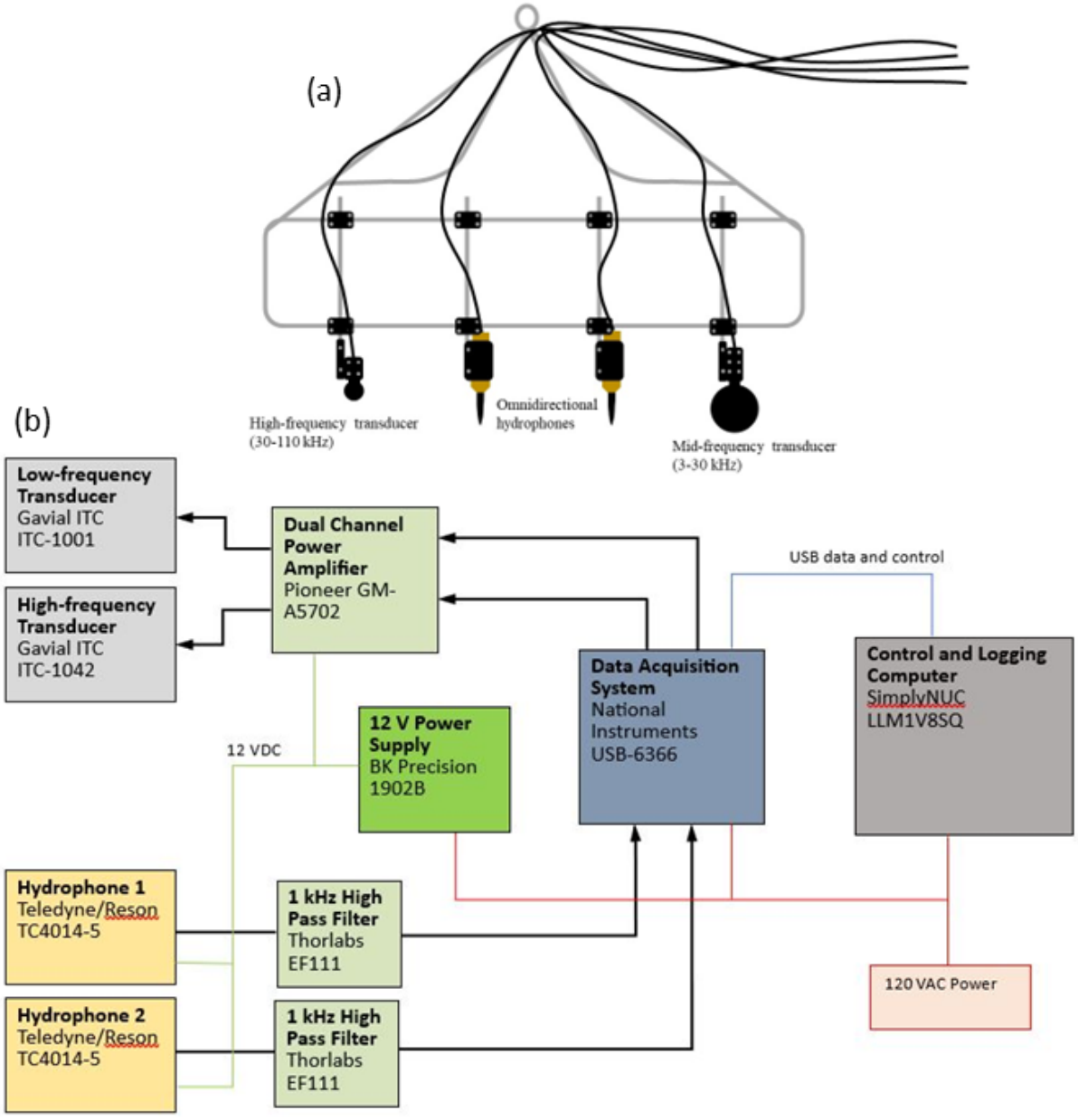

Figure 3.3 a) Diagram of the arrangement of two omnidirectional sources and two identical receiving hydrophones mounted ~20 cm apart on a custom aluminum frame. Stabilizing fins were fixed to the frame during field deployments. b) Schematic of bubble measurement system electronics.

3.4 Laboratory measurement methods

The experiment took place from 8-12 August 2022 in the Large Wave Flume at the O.H. Hinsdale Wave Research Laboratory of Oregon State University in Corvallis, OR, USA. The wave tank was 104 m long and 3.7 m wide with a water depth of 2.5 m. It contained freshwater with 750 mL of Triton X-100

surfactant added (1 mg/L) to lower the surface tension and facilitate the generation of more bubbles. The temperature of the water in the tank was consistent throughout the period of the experiment (Table 3.1). For each replicate of the experiment, a soliton wave with a height of ~1 m was generated and propagated along the tank. A custom ramp structure was built to trigger the wave to break around the halfway point.

Table 3.1 Relevant physical properties of the water in the test tank.

Property	**Value**
Temperature (°C)	19.6
STP pressure (Pa)	100e3
Surface tension of water, σ (N/m)	0.07
Water viscosity, μ (Pa·s)	8.9e-4
Water density, ρ (g/L)	1000
Triton X-100 (surfactant) concentration (mg/L)	1

On 10 August 2022, the bubble measurement acquisition system was fixed with the sources and receivers submerged 0.2 m below the surface and collocated with a CTD. The system was fixed at a different horizontal position along the tank on each day of the experiment, though only data from 10 August 2022 are presented here as this was when the system was in closest proximity to the wave break.

The transmitted signal for the tank experiment consisted of alternating linear chirps emitted from the mid- and high-frequency sources (4-28 and 30-100 kHz, respectively; 1 ms duration) delayed by 62 ms. This sequence was transmitted at a 4 Hz repetition rate. The chirps were amplitude modulated to offset the frequency responses of the sources, resulting in transmitted signals with relatively flat spectra (Fig. 3.4). Data were collected continuously by the receiving hydrophones at a 1 MHz sample rate. Data collection paused every 120 seconds to allow the system to write the data to a file on the acquisition laptop hard drive, resulting in 2-3 data files per wave replicate. Care was taken to begin data collection before the wave approached the system to obtain some baseline bubble-free data, and the replicates were spaced 10-15 minutes apart to allow the tank to return to rest in between wave breaks.

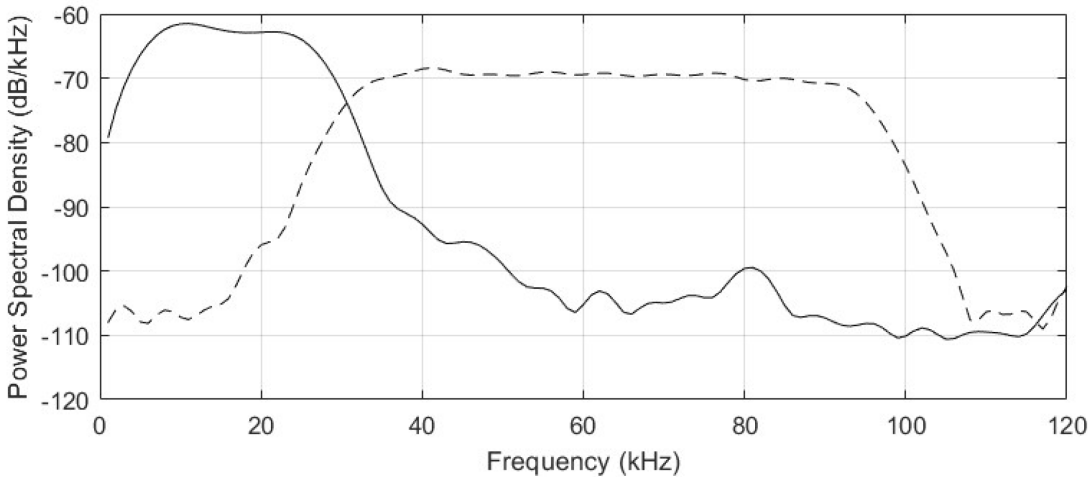

Figure 3.4 Power spectral densities [dB/kHz re 1 W] of the amplitude-modulated transmitted chirps (solid curve is mid-frequency, dashed curve is high-frequency).

3.5 Data processing

A mid-frequency and high-frequency replica signal received in bubble-free water at the closest hydrophone to each source was used to perform the matched filters. The bubble attenuation data from each hydrophone were then post-processed as follows.

First, the raw time-series data from each hydrophone was divided into 1.7 ms-long sections corresponding to the low- and mid- frequency categories. This omitted null periods between pings, reducing data size. Then, a bandpass filter was applied to each ping (2-33 kHz for the mid-frequency band and 10-120 kHz for the high-frequency band) as well as a Tukey window with a cosine fraction of 0.05.

Next, a matched filter was applied to each ping using the bubble-free received chirps as the replica signals. The envelope of the matched filter output contained two dominant peaks, the first being the direct arrival from the source to the hydrophone and the second being a closely following surface echo (Fig. 3.5). Care was taken to only analyze pings with clear separation between the direct and surface arrival. The peak and associated side lobes for the direct arrival were isolated, multiplied by a Tukey window of cosine fraction 0.05, and the Fast Fourier Transform (FFT) was calculated, squared, and converted to a logarithmic scale (i.e., $10\log_{10}|\mathrm{FFT}|^2$) to yield a power spectrum in frequency space. Data collected in the field were processed using a similar method, however since interference from surface echoes was not a concern, the matched filter peaks were used to locate the direct arrivals and the Welch Power Spectral Density (PSD) of the raw received signals was calculated instead of the power spectrum.

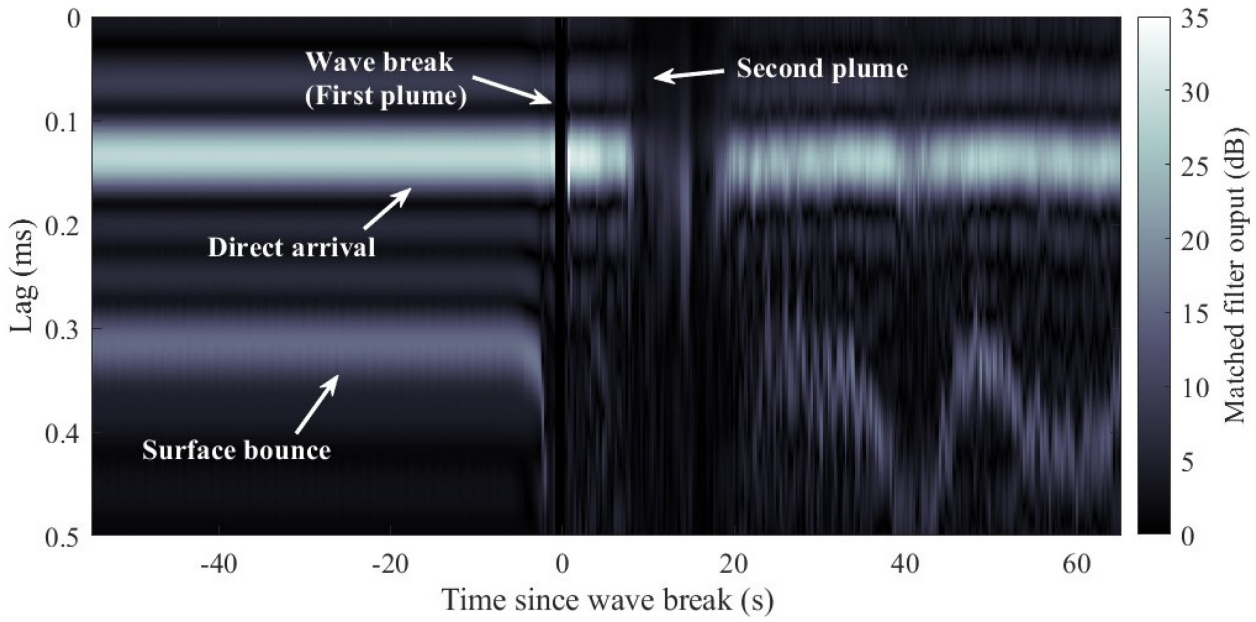

Figure 3.5 Echogram showing matched filter output [dB re 1 V^2] from the bubble measurement system on 8/10/2022. Two arrivals are visible: a direct arrival from source to receiver, and a second arrival of the surface bounce.

The excess attenuation in log space due to bubbles was calculated as the difference between the spectrum of the signal in bubble-free water and the spectrum of the signal with bubbles present, divided by the distance between source and receiver (estimated from the travel time of the signal), which yields $\alpha_{meas}(f)$ in dB/m. The bubble-free spectrum was obtained by averaging over the power spectra in linear space of 30 pings in the wave tank in still water, before the wave arrived (Fig. 3.6). Pings after the wave broke were averaged in groups of 4 consecutive pings (spanning 1 second) to obtain spectra with bubbles present. To estimate the noise floor in the tank, 50-ms sections of time-series data in between pings were extracted and processed exactly like the received pings. Noise in the tank oscillated with a regular pattern and the signal-to-noise ratio remained >30 dB (Fig. 3.6).

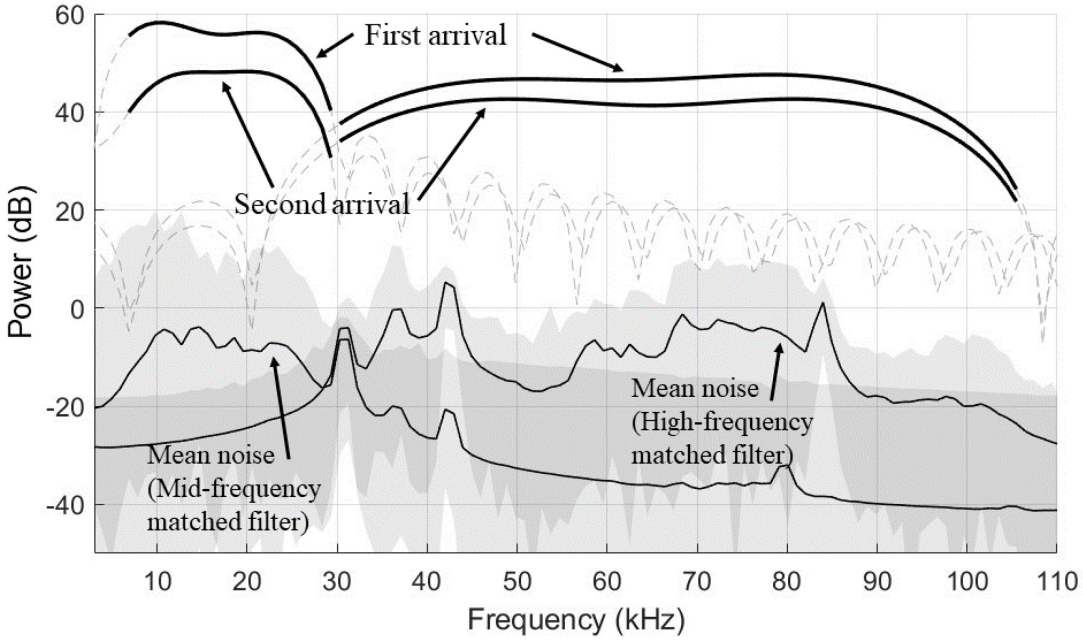

Figure 3.6 Bubble-free power spectra measured in the tank before the wave was generated [dB re 1 V^2]. The thick black curves labeled “First arrival” and “Second arrival” indicate the sections of the power spectra used in analyses of each signal’s arrival at its closer hydrophone and farther hydrophone, respectively. Dashed gray lines indicate the sections of the spectra omitted from analyses. The thin black lines in the lower half of the plot show the mean noise in the tank measured by the system, matched filtered with both the mid- and high-frequency transmitted chirps to parallel the processing of the signals. Shaded gray area indicates the range of noise observed as it oscillated. The signal-to-noise ratio in the tank was consistently above 30 dB.

The attenuation between each source and its closest hydrophone was used for the analyses presented here. The attenuation between the two hydrophones was also considered, however due to the longer path lengths involved there was less data available after the wave break where the signal was not fully attenuated by the bubble plume. It is important to note that basing bubble distribution estimates on the attenuation between each source and its closest hydrophone meant that each frequency band captured a different volume of the water column, so this method relied on the assumption that the bubble distribution in the direction parallel to the wave crest was uniform.

3.6 Laboratory observations

Each breaking wave replicate in the test tank was characterized by one initial dense bubble plume generated by the wave front followed by a second bubble plume that is a characteristic of plunging breakers (van der A et al., 2017; Ting and Kirby, 1995). Two distinct signal arrivals were detected by each hydrophone: a first arrival directly from the source to receiver, and a second arrival of a surface

bounce (Fig. 3.5). As the wave propagated throughout the tank, the timing of the second arrival varied based on wave-induced changes in the surface height while the timing of the direct arrival varied only slightly due to bubble-induced changes in sound speed. When the breaking wave front passed over the measurement system, excess attenuation due to bubbles was sufficiently high to completely attenuate the received signal, making observations of bubble size distributions impossible for the first couple seconds after the wave broke and intermittently for the first ~ 10 seconds after the second plume passed over the measurement system.

The measured bubble size distributions show that bubbles of radii greater than ~ 200 µm are lost within the first 30 seconds after the wave breaks (Fig. 3.7). Given that bubbles of this size should have terminal rise velocities around 4 cm/s (Lewis and Schwartz, 2004) and the bubble plume in the tank extended about 1-1.5 m deep, it would be reasonable to assume that these larger bubbles disappear around 30 s after the wave break because they have risen to the surface. Additionally, bubbles of radius ~ 100 µm should have terminal rise velocities of approximately 2 cm/s (Lewis and Schwartz, 2004), which could explain the decrease in bubbles of radii > 100 µm by 50 s after the wave break. The buoyancy of smaller bubbles may not exceed the turbulent forces associated with the wave, which could explain why bubbles of radii < 100 µm still remain beyond 50 s. I observed that very small bubbles remained entrained for great lengths of time; at 170 s after the wave break there was still a considerable population of bubbles with radii smaller than 100 µm, demonstrating the long-term persistence of bubbles small enough to remain entrained. Microbubbles in the tank were still visible up to 15 minutes after the wave break event.

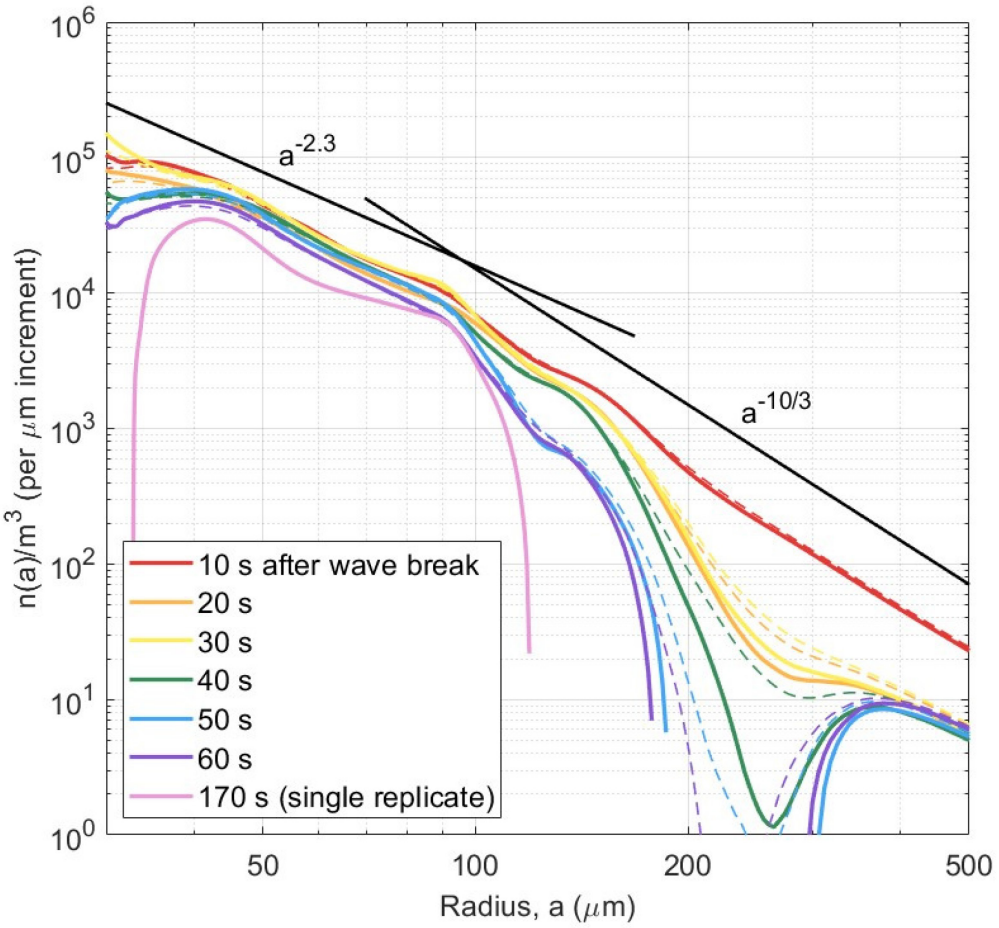

Figure 3.7 Acoustically measured mean bubble size distributions at 10-second intervals up to a minute after the wave break event, plus an additional mean bubble size distribution 170 s after the wave break event to demonstrate longer-term behavior. Each curve is an ensemble average over the bubble size distribution measured from six replicates of the wave break, except for the curve at 170 s obtained from a single replicate. Gaps in the curves occur where no attenuation or negative attenuation occurred. Dashed lines for all but 170 s indicate mean bubble size distributions estimated from just the Resonant Bubble Approximation. The black lines are the theoretical -2.3 and -10/3 power laws for quiescent bubbles smaller than the Hinze scale and acoustically active bubbles greater than the Hinze scale, respectively (Deane and Stokes, 2002).

Compared with the bubble size distributions observed by Deane & Stokes (2002), the bubble size distributions observed in this study at radii < 100 µm agree reasonably well with the $a^{-2.3}$ power law reported for quiescent bubbles smaller than the Hinze scale, and the overall density of bubbles was similar. The distributions of bubbles larger than 100 µm radius are challenging to compare with other studies because many of the larger bubbles have already risen to the surface in the time scales considered here. At 10 s after the wave break, the distribution of bubbles greater than 100 µm agree

best with the $a^{-10/3}$ power law observed by Deane and Stokes (2002) for bubbles greater than the Hinze scale during the acoustically active phase. This would be unexpected since all bubbles measured in this study are quiescent and smaller than the Hinze scale, however Cartmill and Yang Su (1993) observed a similar a^{-3} power law for bubbles with radii in the 100-1200 µm range. Given that Cartmill and Yang Su (1993) conducted their measurements in the same wave tank used in the present study, the discrepancy between the bubble distributions measured here and by Deane and Stokes (2002) might arise in part due to differences in laboratory setup, but is more likely related to the dispersive nature of the bubbles when unforced. Harb and Foroutan (2019) examined the evolution of the bubble size distribution in the first 5 seconds after a laboratory wave breaking event and observed significant drooping of the density of larger bubbles that effectively lowered the Hinze scale with time. Given the longer time scales investigated in this study, the change of slope of the bubble size distribution observed at 100 µm may reflect that the Hinze scale has decreased by the time of the first measurement at 10 s post-breaking.

Previous research has shown that bubble densities under breaking waves increases with increasing salinity while the slope of the size distribution stays constant (Cartmill and Yang Su, 1993; Harb and Foroutan, 2019). Surfactants may also influence bubble distributions. Winkel et al. (2004) observed a decrease in mean bubble size with increasing salt and Triton X-100 concentrations for bubbles generated by an air injector rather than a plunging breaker. The addition of the Triton X-100 lowers the surface tension of the tank water (Ullah et al., 2019), though the impact on surface tension at the concentration used in this study would be small.

3.7 Field observations

The observations and data processing routines developed for the wave tank experiment served as a basis for the interpretation of field measurements of bubbles in an estuarine tidal front. The field campaign took place on 19-21 October 2021 in the Connecticut River estuary off Old Saybrook, Connecticut, USA (41.262139 °N, -72.341132 °W), where a tidal ebb plume front forms outside the mouth of the river (Garvine, 1977). The bubble measurement system was suspended from the starboard davit on the 60-ft coastal research vessel R/V *Tioga*, lowered into the water beside the boat, and towed back and forth across the same section of the front at a range of depths while collecting data. Shipboard broadband echosounders were operating at 38, 70, 120, 200, and 333 kHz throughout the campaign to aid in locating the frontal bubble plume.

During the field deployment, 20 pairs of high- and mid-frequency chirps were written to each file, yielding a data collection rate of ~1 file/second. The hardware high-pass filter was not integrated in the bubble measurement system at the time of the field deployment, so a software high-pass filter was applied as the first step of post-processing to remove low-frequency noise introduced in the field setting. It was discovered during post-processing that the mid-frequency signal was saturated in bubble-free water, leading to underestimates in excess attenuation below 30 kHz and consequent underestimates of bubble density for radii larger than 100 µm. Thus, only inversion results for the high-frequency signal are presented (Fig. 3.8). Based on the modeling results in Section 1.4.3, inverting just the high frequency signal should still yield reasonably accurate estimates of the bubble size distribution. The parameters in Table 3.1 were used in the inversion calculation for the field measurements with just temperature changed to the value measured in situ by a CTD, as the other properties for salt versus fresh water had an insignificant impact on predicted bubble attenuation (Section 1.4.2). Estimates of bubble size

distributions were obtained in the front on 19 October 2021 at depths from 0.4-1.5 and 3.0-3.8 m (Fig. 3.8). The wind speed on this day was ~10 m/s.

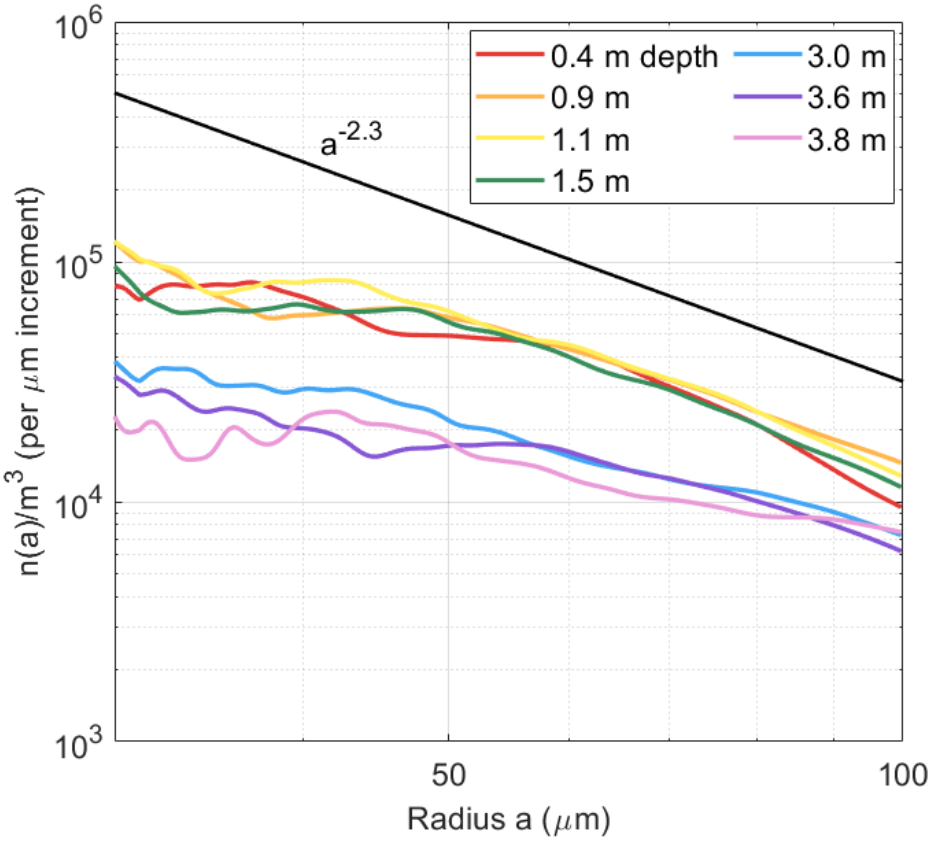

Figure 3.8 Acoustically measured bubble size distributions at a range of depths in the Connecticut River Estuary tidal front. Each curve is an average of over 20 pings spanning a 0.1-second interval and has been smoothed with a moving average to reduce noise. The black line is the theoretical -2.3 power law for quiescent bubbles smaller than the Hinze scale (Deane and Stokes, 2002).

Compared to the bubble size distributions observed by Deane and Stokes (2002), the bubble size distributions observed in the front at radii < 100 µm are overall slightly shallower than the $a^{-2.3}$ power law reported for quiescent bubbles smaller than the Hinze scale, though they do appear to steepen slightly with increasing bubble size and perhaps would agree better if the bubbles larger than 100 µm were not underestimated due to the saturated mid-frequency signal. It is reasonable to expect this slope in the front, where bubbles are entrained for long periods beyond their active phase. The density of bubbles observed in this study is comparable to previous measurements under breaking waves in the open ocean at similar wind speeds (Farmer et al., 1998; Leighton et al., 2004; Trevorrow, 2003). The overall density of bubbles in the front decreases with depth but to a lesser extent than a bubble plume under breaking waves (Farmer et al., 1998; Terrill et al., 2001), suggesting that many bubbles are entrained by downwelling at the front. The maximum near-surface downwelling at the Connecticut River front has been observed to be 0.2 m/s (O'Donnell et al., 1998), which would entrain bubbles of radii

smaller than ~ 1300 µm (Lewis and Schwartz, 2004). The slope of the bubble size distribution also appears slightly shallower at deeper depths, which could be driven by dissolution (Garrett et al., 2000).

3.8 Conclusion

While acoustical techniques have been used for years to measure bubble densities and size distributions under breaking waves, the bubble distributions in estuarine tidal fronts remain poorly understood. In this study, a towable bubble measurement system was developed to measure broadband excess attenuation from which bubble size distributions could be inferred. Future studies using excess attenuation to probe bubble distributions in the field might consider additional testing of different combinations of source power levels and distances between sources and hydrophones to optimize the amount of usable data. The measurement system was used to measure quiescent bubbles generated by breaking waves in a laboratory setting and the resulting bubble densities and size distributions were similar to previous measurements. The system was also used to measure bubbles entrained in the Connecticut River ebb plume at a range of depths. The bubble size distribution in the front resembled that of quiescent, sub-Hinze scale bubbles under breaking waves, with overall bubble density decreasing with depth but to a lesser extent. Questions remain around how the bubble distribution changes spatially along the front and behind the front, how the bubble plume evolves over the lifetime of the front, and what can be inferred about the hydrodynamics at play in the front. Gaining an increased understanding of bubbles in tidal fronts and their associated processes will allow for better understanding of their role in air-sea exchange and the operational considerations relevant to acoustic communications and sonar performance in estuarine environments.

4 Spatial trends of the bubble size distribution in an estuarine front

4.1 Introduction

The goal of this chapter is to use measurements of bubble size distributions in an estuarine front to gain some understanding of how the front's hydrodynamics drive the entrained bubble distribution. The convergence of river outflow with the surrounding ocean has been found to enhance surface wave breaking at the front, resulting in a relatively high density of persistent microbubbles (Baschek et al., 2006; Thomson et al., 2014), even on a calm day with little wind-driven surface wave action (Bassett and Lavery, 2021). Downwelling at the front subducts these bubble plumes to much deeper depths than plumes formed in open water by wave breaking alone (Baschek et al., 2006), where they are then advected by strong horizontal currents (Bassett et al., 2023). These processes can form dense bubble plumes that extend much farther than indicated by the foam lines formed at the surface (Baschek et al., 2006; Bassett and Lavery, 2021; Kilcher and Nash, 2010). Developing an understanding of how the size, spatial, and temporal distributions of bubbles are impacted by frontal features is therefore important for acoustical operations in these coastal environments as well as for constraining estimates of bubble-mediated aeration of surrounding water.

Inferring bubble size distributions from backscattering strength is one of several acoustical techniques developed to quantify microbubbles but has not been as widely used as other acoustical and optical techniques. A backscattering approach was first described by Vagle and Farmer (1992), who measured backscatter from bubbles at multiple frequencies using up-looking transducers. They tried multiple methods for inverting the backscattering measurements to obtain estimates of bubble size distributions, including an iterative technique that starts with an initial guess of $n(a)$ and adjusts with each iteration, a matrix representation of the inversion that led to inaccuracies, and a simplified direct inversion that ignores contributions to scattering above resonance and fails at frequencies above 400 kHz. Compared to other techniques for measuring bubble size distributions, backscattering measurements may be hindered by excess attenuation from dense bubble clouds and high air fractions near the surface (Bassett and Lavery, 2021; Vagle and Farmer, 1998b). However, remote sensing of bubbles via backscattering offers unique advantages over other techniques such as providing vertical profiles of bubble densities and measurements of relatively low bubble densities (Vagle and Farmer, 1998b).

In this chapter, broadband measurements of volume backscattering strength are inverted to obtain estimates of the bubble size distribution at a range of locations relative to the Connecticut River front. The dependence of the bubble distribution on depth at the front and distance away from the front are examined within the context of the front's hydrodynamics.

4.2 Methods

4.2.1 Set-up and transducer calibrations

This chapter is focused on the dynamics of the Connecticut River tidal ebb plume front, which forms at the boundary between brackish river outflow and denser ambient seawater (Fig. 4.1). Field observations took place on 19-21 October 2021 in the Connecticut River Estuary off Old Saybrook, Connecticut, USA (41.262139 °N, -72.341132 °W). Broadband echosounders with nominal center frequencies of 38, 70, 120, 200, and 333 kHz for a total band of 25-410 kHz (Table 4.1) were mounted to a pole fixed to the side of the 60-ft coastal research vessel R/V *Tioga* and lowered to a depth of 0.79 m below the sea surface. The 38 kHz transducer was an Airmar M192-38 and the rest were manufactured by Kongsberg (Table 4.1). The transducers were connected to two Kongberg WBT Tube transceivers, which were connected to a data acquisition laptop running the EK80 software for Windows. The echosounders operated continuously throughout the field campaign while the research vessel made repeated transects over the front, with each transducer accounting for one "channel".

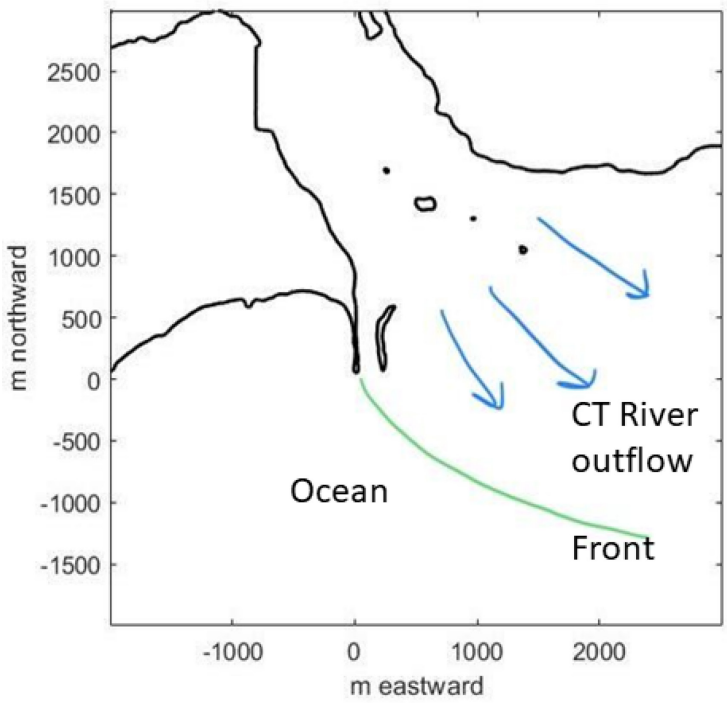

Figure 4.1 Map of the study area. During ebb tide, a front forms at the offshore boundary of the Connecticut River outflow and evolves throughout the 6-hour tidal cycle (Garvine, 1977).

A calibration was performed on 30 September 2021 in a testing well off the dock at the Woods Hole Oceanographic Institution in Woods Hole, Massachusetts, USA, following the method of Lavery et al. (2010), which is based off established protocols (Demer et al., 2017; Foote and MacLennan, 1984; Vagle et al., 1996). The echosounders were calibrated in the well using a spherical, 38.1-mm-diameter (21.2-mm-diameter for the 38 kHz transducer), tungsten carbide with 6% cobalt standard target, which was tethered on a monofilament line approximately 6 m (38.1-mm target) and 8 m (21.2-mm target) below the transducers. The EK80 standard calibration software was used to collect data in all four sectors

and the center of each transducer operating in split-beam mode (Demer et al., 2017). For the transducers operating in single beam mode, the target was moved around under the transducers while pinging and the echoes with the top 10% target strength (TS) magnitude, which were presumed to be the most centered, were averaged and used to calculate a calibration curve. To ensure optimum calibration accuracy for the single-beam transducers, the measured TS was also fit to beampattern corrections for a range of off-axis angles following the method of (Lavery et al., 2017) and adjusted accordingly for the best-fit off-axis angle. A calibration curve for each transducer was calculated as the difference between the measured TS of the standard target and the theoretical TS predicted for the target (Fig. 4.2). The usable frequency band for each transducer was determined by visual inspection (Table 4.1).

Table 4.1 Operational parameters for the echosounders used in this study.

	M192-38	ES70-7CD	ES120-7CD	ES200	ES333
Single or split beam	Single	Split	Single	Split	Split
Pulse duration (ms)	1.024	1.024	1.024	1.024	1.024
Decimated sampling frequency (kHz)	31	50	91	200	200
Start frequency (kHz)	25	53	95	160	280
End frequency (kHz)	45	90	160	260	420
Used frequency band (kHz)	25-38	53-90	100-140	170-255	288-410
Power (W)	100	150	250	90	45
Ping rate (Hz)	2.5	2.5	2.5	2.5	2.5

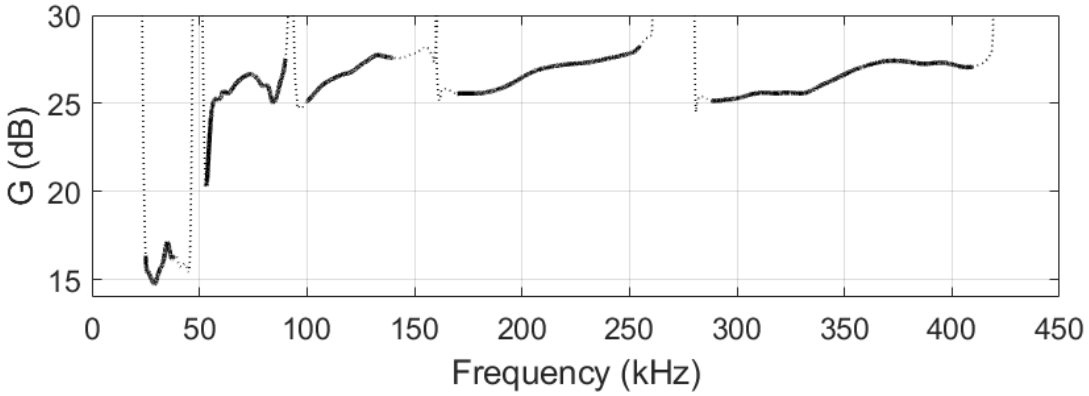

Figure 4.2 Calibration curves for all five transducers used in this study [dB re 1 m^2]. Solid line indicates used portion.

4.2.2 Study environment

The currents associated with the front were described by Garvine (1977) and Garvine and Monk (1974). Surface water flows toward the front at 20 cm/s and is accompanied by downwelling at the front, also at 20 cm/s. From 1 m depth to the seafloor there is a uniform current flowing shoreward and normal to the front at 50 cm/s (Fig. 3.1). Small bubbles generated at the front are carried by these currents and entrained until they rise to the surface or dissolve (Fig. 4.3). Salinity changes abruptly at the front where brackish water meets seawater, and the spatial distribution of bubbles is strongly correlated with the resultant density stratification (Fig. 4.4). Turbulence is highest in the 10-m wide convergence zone, behind which is a transition zone where turbulent mixing occurs with decreasing turbulent kinetic energy rates extending to about 100 m out, followed by a region of stable stratification (Delatolas et al., 2023).

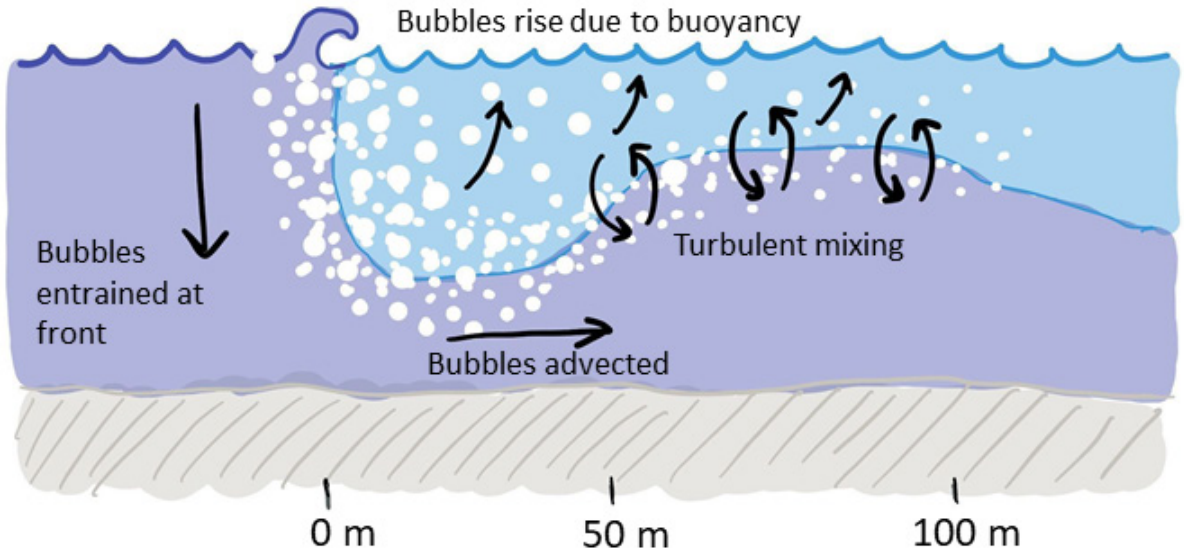

Figure 4.3 Conceptual model for a frontal bubble plume.

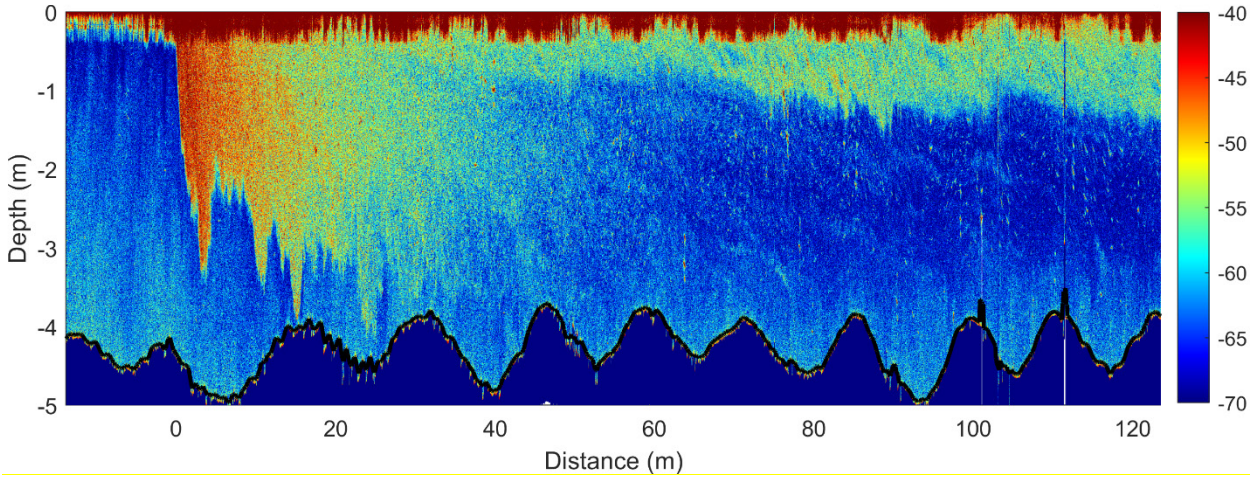

Figure 4.4 Echogram of volume backscattering strength [dB re 1 m^{-1}] collected in 2017 showing a bubble plume in the Connecticut River ebb plume front in calm conditions. The front is indicated by the strongly scattering edge of the bubble plume at 0 m distance.

4.2.3 Estimating maximum bubble size

To predict maximum bubble sizes at various locations near the front, consider the relationship between bubble radius and rise velocity for "dirty bubbles," which are affected by a surface-active material such that the "no slip" boundary condition applies (Fig. 4.5):

$$v_{rise} = \frac{33a^2}{(a + 0.37)^2} \tag{4.1}$$

where a is the bubble radius in mm and the rise velocity v_{rise} is in cm/s (Lewis and Schwartz, 2004). A series of simple calculations can lead to rough estimates of maximum bubble size. For example, if I am measuring the bubble size distribution at the surface 100 m behind the front and the bubble plume at the front extends down to 5 m deep, the largest bubble would rise 5 m in the amount of time it takes to travel a horizontal distance of 100 m at 50 cm/s, which would imply a 2.5 cm/s rise velocity. Inverting Eq. (4.1) leads to an estimated maximum bubble radius of 141 µm. While this is an overly simplified estimate, it is useful to check against measured bubble size distributions in the field.

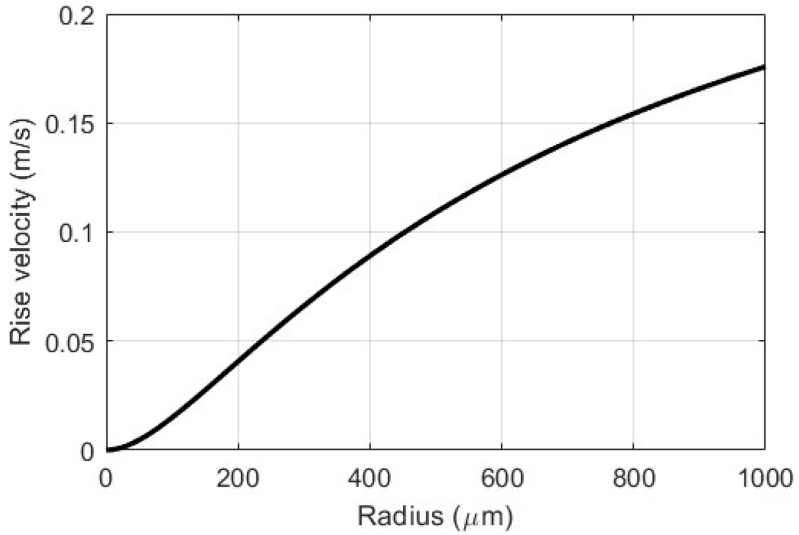

Figure 4.5 Bubble terminal rise velocity vs. radius.

4.2.4 Data processing

Although multiple transects over the front were made during the field experiment, windy weather conditions negatively impacted the quality of the backscatter measurements as there were frequent signal dropouts. Thus, only three transects where the full bubble plume structure was clearly visible in the echogram were analyzed for this chapter (Fig. 4.6.b-d). The replicates are referred to as Front 1, Front 2, and Front 3. While the bubble clouds associated with Fronts 1 and 3 similarly extend to about 100 m behind the front, the bubbles in Front 2 extend to around 200 m, demonstrating some of the variability observed between transects. Additionally, a section of backscatter data collected away from the front, in just seawater, were analyzed as a baseline for bubble-free water and bubbles under surface breaking waves (Fig. 4.6.a).

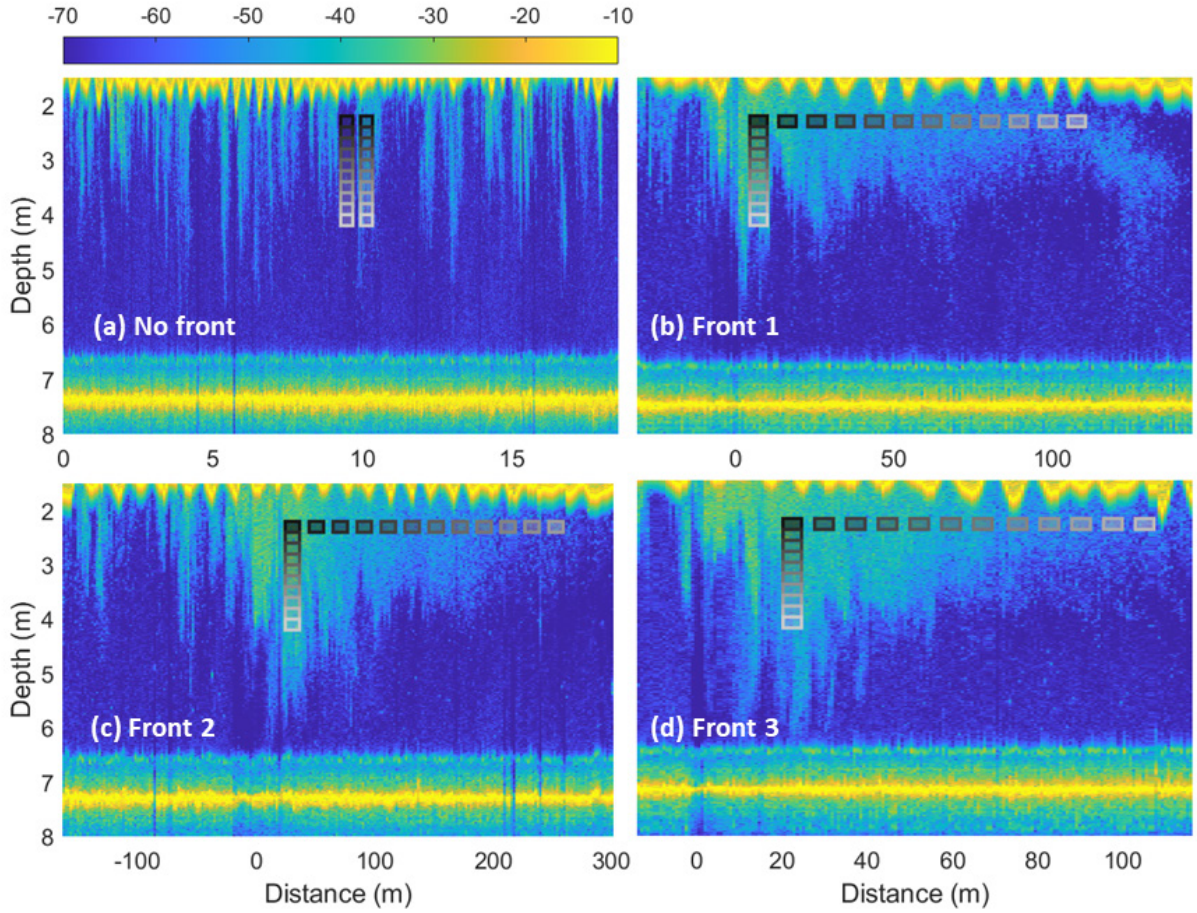

Figure 4.6 Echograms of volume backscattering [dB re 1 m^{-1}] at 120 kHz showing a) an area away from the front in Long Island Sound, b) Front 1, c) Front 2, and d) Front 3. Grayscale rectangles indicate the 20-cm-by-6-ping bins where mean S_v was calculated.

Raw echosounder data were pulse compressed following the method of Andersen et al. (2021) for split- and single-beam transducers. For the split-beam transducers, the compressed voltage was averaged across all sectors. Following Andersen et al. (2021), the volume scattering strength $S_v(t)$ (uppercase S denotes log space) was calculated in the time domain to generate echograms for each channel. The maximum S_v of the seafloor was obtained from each ping so that the effect of excess attenuation due to near-surface bubbles at the front could be estimated from the seafloor scattering strength (Bassett and Lavery, 2021). Bins of data 20 cm tall were selected and used in calculations of volume backscattering spectra, $S_v(f)$, for each channel also following Andersen et al. (2021), and averaged across 6 consecutive pings for each region of interest (Fig. 4.6). The location of the bins was selected to avoid pings that were significantly impacted by excess transmission loss from bubbles in the upper water column (Bassett and Lavery, 2021), as indicated by a drop in the scattering strength of the seafloor in the 38 kHz band (Fig. 4.7). Excess transmission loss away from these areas was assumed to be small and was therefore not estimated or incorporated into S_v calculations.

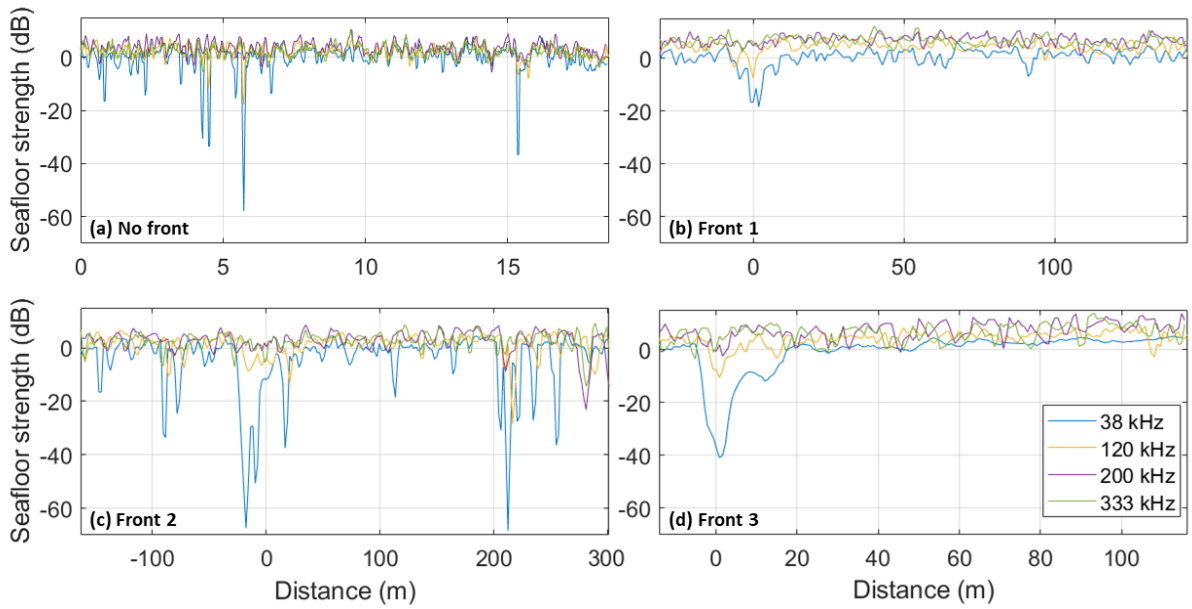

Figure 4.7 Seafloor scattering strength [dB re 1 m^{-1}] a) in seawater away from the front, b) Front 1, c) Front 2, and d) Front 3 plotted as a function of distance from the front. The seafloor scattering strength was obtained as the maximum value of the volume backscattering strength within the 7-8 m depth range. Each frequency channel is plotted as its own curve. Dense bubble populations are indicated by a drop in the seafloor scattering strength in the 38 kHz band.

A smooth, continuous S_v spectrum was needed for the inversion to bubble size distribution (Fig. 4.8). The spectra of all five channels were stitched together via linear interpolation and smoothed with a 20-point moving average. In post-processing, the ES70 was discovered to be malfunctional, so its spectrum was removed and linearly interpolated over before applying the smoothing function. For additional smoothing to reduce nulls in the $n(a)$ inversion output, the section of each S_v curve corresponding to frequency ≥ 150 kHz was then fit and replaced with a 4th order logistic function ('logistic4' in MATLAB 2023b's "fit" function), and that section of S_v was replaced with the fitted curve. Finally, the entire S_v curve was fit and replaced with a 9th degree polynomial ('poly9' in MATLAB 2023b's "fit" function), and this final curve was fed into the inversion calculation described in the following section. Curve fitting was calculated in log space to minimize small bumps in S_v that become discontinuities once inverted for $n(a)$, and the functions used for fitting were selected by trial-and-error to capture the general shape of S_v without adding extra artifacts to the tails of the curve. Assuming the true $n(a)$ follows a power law (Deane and Stokes, 2002), such an aggressive smoothing routine for S_v was justified so long as the magnitude and broad shape of the curve were preserved.

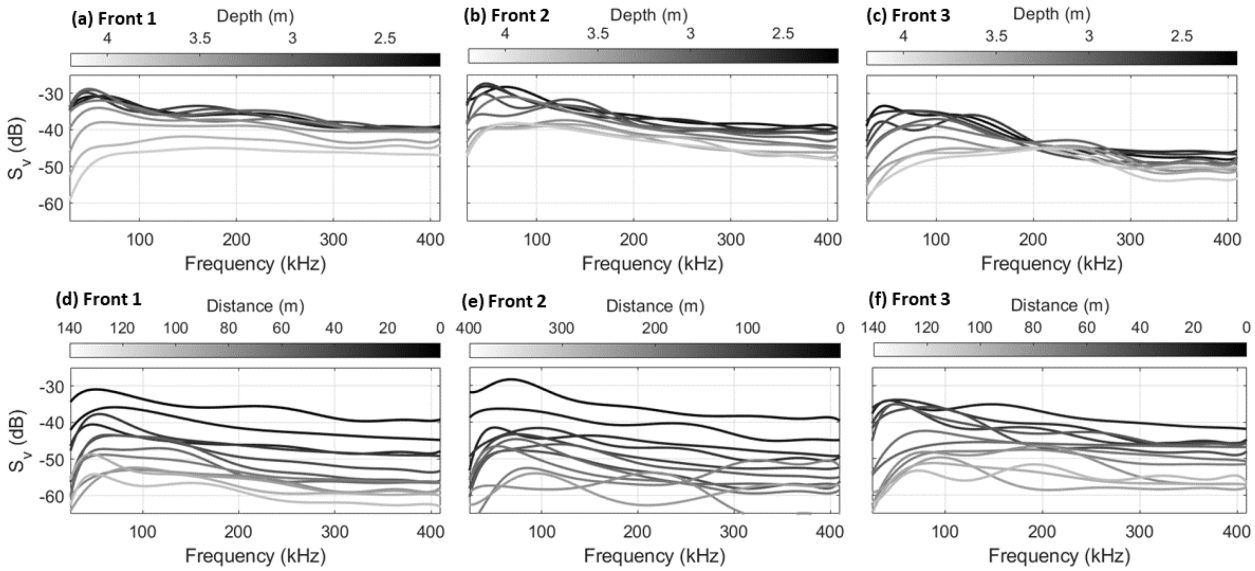

Figure 4.8 Volume backscattering spectra [dB re 1 m^{-1}] computed in depth- and distance-varying bins for all three front transects. Curves in (a), (b), and (c) are colored by depth. Curves (d), (e), and (f) are colored by distance from the front.

4.3.5 S_v inversion

Because the S_v measurements in this study are broadband, the approach of Caruthers et al. (1999) was adapted to invert S_v instead of excess attenuation spectra. Recall the harmonic resonator formulation for volume backscattering from bubbles (Medwin and Clay, 1998):

$$s_v = \int_a [n(a)da] \left[\frac{a^2}{[(f_R/f)^2 - 1]^2 + \delta^2(f)} \right] \tag{4.2}$$

where lowercase s_v denotes linear space while uppercase $S_v = 10\log_{10}|s_v|$ denotes log space. Despite being most accurate near and below resonance, at high frequencies the harmonic resonator model for the scattering cross section converges to a value four times that of the modal series solution because it does not include higher order resonances. Thus, for numerical calculations of predicted backscattering in this dissertation, a hybrid scattering model was generated using the resonator model for $ka < 0.1$ and the modal solution (Medwin and Clay, 1998) for $ka > 0.1$ (Fig. 1.4), following the approach of Lavery et al. (2007).

This hybrid formulation for the forward calculation from $n(a)$ to s_v is referred to as the "formal theory." If I assume backscattering is dominated by resonant bubbles, I obtain the resonant bubble approximation (RBA) from the harmonic resonator formulation (Medwin and Clay, 1998):

$$s_v \approx \frac{\pi a^3 n(a)}{2\delta} \tag{4.3}$$

where s_v is a function of frequency derived from the relationship between resonance frequency and radius (Medwin and Clay, 1998). Starting with the measured volume backscattering spectrum, $s_{v,meas}$, the inversion procedure followed these steps for a single iteration:

1. $s_{v,meas} \xrightarrow{RBA} n_1$
2. $n_1 \xrightarrow{formal\ theory} s_{v,1}$
3. $(s_{v,meas} - s_{v,1}) \xrightarrow{RBA} n_{error}$
4. $n_2 = n_1 + n_{error}$
5. $n_2 \xrightarrow{formal\ theory} s_{v,2}$

For additional iterations, $s_{v,2}$ can be plugged back into Step 3-5 in as many loops as necessary to get good agreement between $s_{v,meas}$ and $s_{v,2}$. The agreement may be evaluated by calculating the mean square error between $S_{v,meas}$ and $S_{v,2}$ in log space or by visual inspection of the two curves. For the results presented in this chapter, a single iteration of the inversion procedure Steps 1-5 was enough to get sufficient agreement between $s_{v,meas}$ and $s_{v,2}$.

4.4 Results & Discussion

4.4.1 Bubbles under breaking waves

The mean volume backscattering spectra and bubble size distribution were computed for two columns of ten 20-cm tall bins evenly spaced from 2.2-4.0 m depth, one column of bins in a section of data with no visible bubbles, and the other in a bubble plume penetrating over 5 m deep (Fig. 4.6.a; Fig. 4.9). These data were collected beyond the Connecticut River plume in the ambient Long Island Sound, so are not impacted by density-driven stratification.

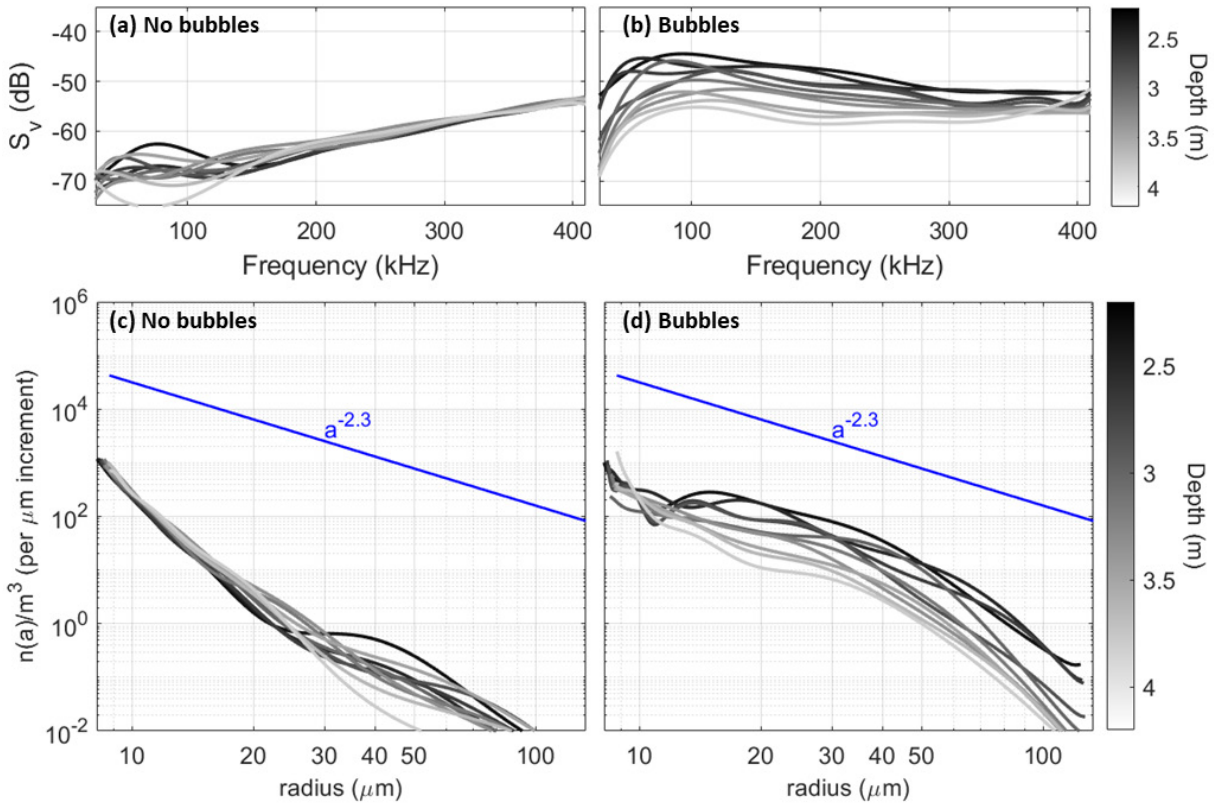

Figure 4.9 Depth-dependent volume backscattering spectra [dB re 1 m^{-1}] and corresponding bubble size distributions in seawater away from the front. (a) and (c) represent an area without bubbles, (b) and (d) represent a bubble plume fed by breaking waves.

Lamarre and Melville (1994) observed that breaking waves alone inject bubbles down to only about 1 m deep, so the deeply penetrating plumes observed in the Connecticut River estuary, which resemble observations from studies in other environments (e.g., Trevorrow, 2003; Zedel and Farmer, 1991), are probably driven by turbulence. One source of turbulence that could deepen bubble plumes under breaking waves is Langmuir circulation, which are wind-driven cells that create narrow zones of downwelling alternating with zones of upwelling. These cells have been observed in the open ocean to form organized structures of bubbles clouds with a mean penetration depth of 6 m for wind speeds greater than 5 m/s (Zedel and Farmer, 1991). Langmuir circulation has also been observed in shallow coastal environments (Graham and Hall, 1997; Scully et al., 2015), and numerical simulations suggest that the length scales of coastal Langmuir cells are influenced by environmental forcing conditions like Stokes drift velocity, surface wind stress, and wavenumber (Shrestha et al., 2018). Other turbulent mechanisms that could deepen bubble plume penetration are wind stress, which enhances the dissipation rate of kinetic energy from breaking waves (Agrawal et al., 1992), and convection driven by surface cooling (Steffen and D'Asaro, 2002; Zikanov et al., 2002). Likely, a combination of all three mechanisms is a play to create the irregular bubble cloud structure observed in this study (Crawford and Farmer, 1987; D'Asaro, 2001; Gargett and Grosch, 2014; Thorpe, 1992).

In the absence of bubbles, S_v is essentially a spectrum of noise (Fig. 4.9.a), so its corresponding bubble size distribution represents the minimum measurable bubble density with the echosounding

system (Fig. 4.9.c). Noise increased with frequency, so the corresponding bubble size distribution has a relatively steep slope. In the bubble plume, which was fed by wind-driven breaking waves at the surface, the overall bubble density was lower than that of bubbles entrained in the front and had a spectral slope that agreed reasonably well with the -2.3 power law previously observed for quiescent bubbles (Deane and Stokes, 2002), and steepened slightly with depth. As a check, the mean volume backscattering spectrum was also calculated for a section of data below the frontal bubble cloud (Fig. 4.10.a), and its corresponding bubble size distribution agreed with that observed in bubble-free water away from the front (Fig. 4.10.c).

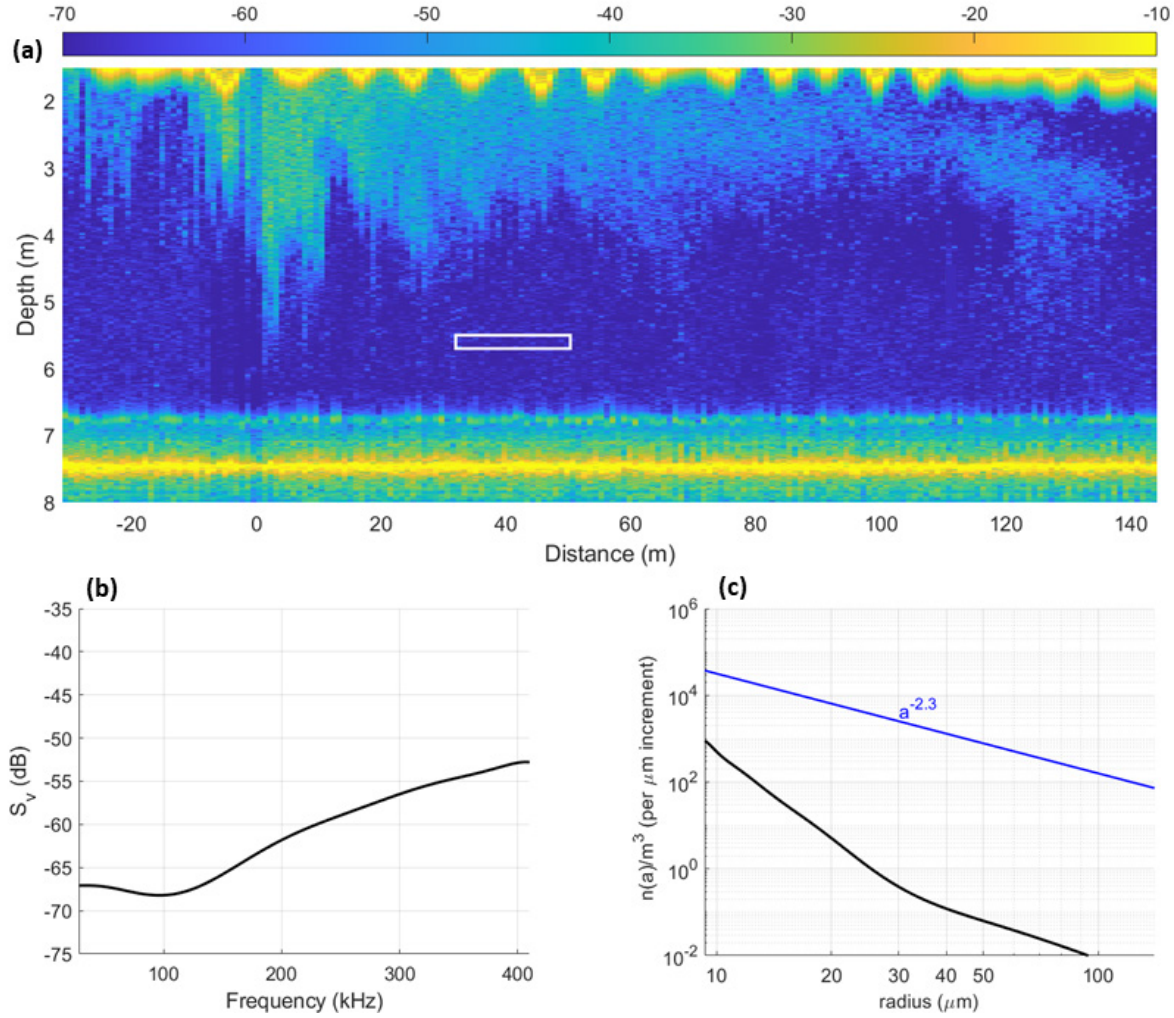

Figure 4.10 a) 120 kHz echogram of volume backscattering [dB re 1 m^{-1}] in Front 1. White rectangle indicates the bubble-free area where the mean volume backscattering spectrum (b) and the corresponding bubble size distribution (c) were calculated. Blue line in (c) is a -2.3 power law for reference (Deane and Stokes, 2002).

4.4.2 Depth dependence in the front

The volume backscattering spectra were calculated for a series of ten 20-cm tall bins at the front, evenly spaced from 2.2-4.0 m depth (Fig. 4.6.b-d). S_v rolled off in the lower frequencies and had a shallow decreasing slope above the 38 kHz band (Fig. 4.8.a-c). In all three transect replicates, the volume backscattering was broadly consistent up to around 3.5 m depth, beyond which it started to droop.

The $n(a)$ inversion results for the depth-varying bins reflect the trends suggested by the S_v curves (Fig. 4.11). The shape and magnitude of the bubble size distribution was similar for all three transects, with Front 3 being a bit lower overall than the other two. Bubble density decreased by 1-2 orders of magnitude across the full depth range, with most of that decrease incurred below ~3.5 m. The bubble size distribution approximately follows a -2.3 power law, which was observed by Deane and Stokes (2002) for bubbles of radii < 1000 µm under breaking waves. These observations suggest that bubbles generated by breaking waves at the front are subducted by the downwelling current to > 4 m depth and that the bubble population is well maintained throughout much of this process. Using the relationship between bubble size and rise velocity (Eq. 4.1), bubbles would need to be smaller than 1300 µm in radius to be carried by the 20 cm/s downwelling current, which far exceeds the maximum radius measurable with the frequency band used here. In general, the density of bubbles in the front exceeds the bubble density under breaking waves (Fig. 4.9.d), though they are similar in the deeper section of the front.

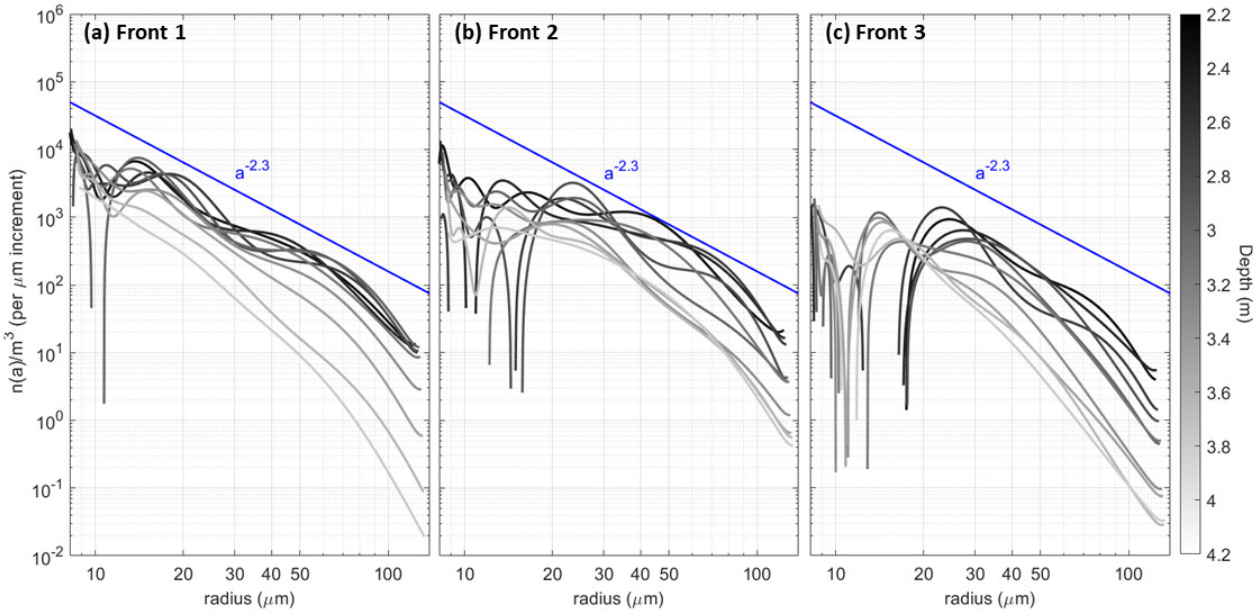

Figure 4.11 Bubble size distributions for depth-varying bins in a) Front 1, b) Front 2, and c) Front 3. Curves are colored from dark to light corresponding to depth of S_v bins. Blue line is a -2.3 power law for reference (Deane and Stokes, 2002).

4.4.3 Dependence on distance from the front

The volume backscattering spectra were calculated for a series of twelve 20-cm tall bins at 2.2 m depth, evenly spaced across most of the frontal bubble cloud (Fig. 4.8.d-f). S_v was greatest at the frontal head and dropped ~20-30 dB from the closest bin to the farthest bin across all frequencies, indicating a significant drop in overall bubble density. The shape of S_v also evolved with distance from the front, with spectra becoming slightly flatter with distance from the front with steeper roll-off at the low frequencies, indicating that the bubble size distribution changed with distance.

In the $n(a)$ inversion results, the bubble density dropped considerably with distance from the front, with an overall density change of ~2 orders of magnitude in all three transects (Fig. 4.12). This was expected since bubbles advected behind the front are entrained for a long time and are thus subject to dissolution. The bubble size distribution also appears to steepen slightly with distance, suggesting that larger bubbles are being lost faster to buoyant degassing. Turbulent mixing due to Kelvin-Helmholtz instabilities along the density gradient between the river plume and underlying seawater inhibits entrained microbubbles from rising to the surface, as Delatolas et al. (2023) observed that turbulent mixing in the ~100 m behind the downwelling zone entrains ambient water. This could create a scenario where dissolution dominates the evolution of the bubble size distribution.

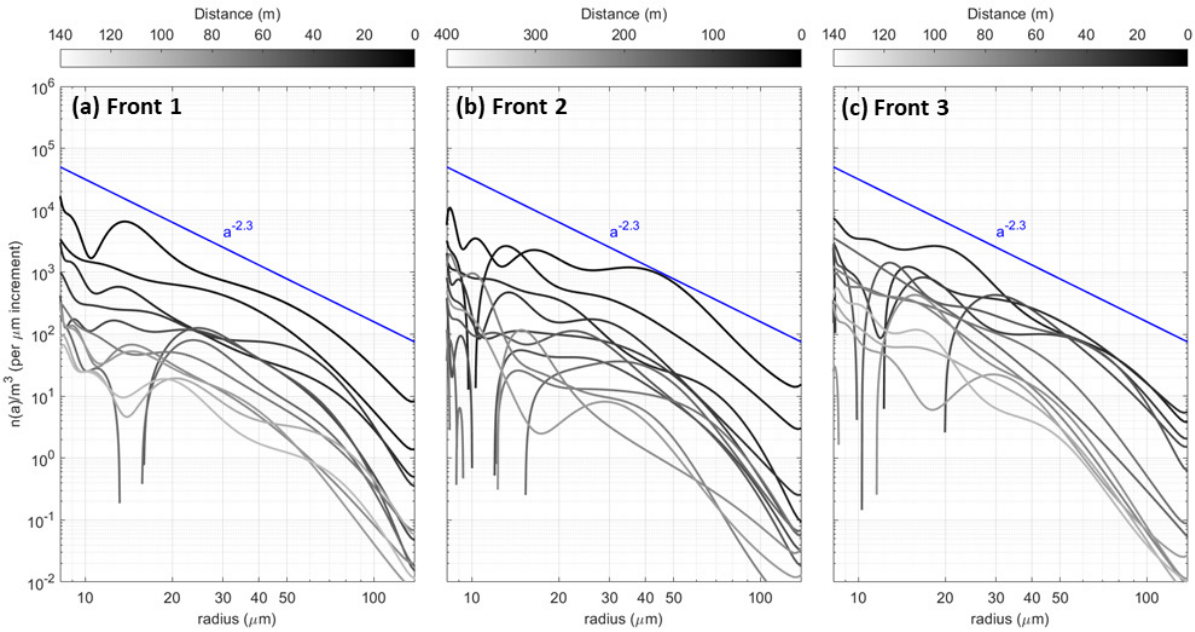

Figure 4.12 Bubble size distributions for distance-varying bins in a) Front 1, b) Front 2, and c) Front 3. Curves are colored from dark to light corresponding to S_v bins closest to and farthest from the front, respectively. Blue line is a -2.3 power law for reference (Deane and Stokes, 2002).

Modeling work by Thorpe et al. (1992) predicts that increased dissolution rates yield uniform decreases in bubble size distributions, and observations in fresh water suggest that the bubble dissolution rate is independent of radius for bubbles of radius 20-350 µm (Thorpe, 1982). Additional work by Garrett et al. (2000) indicates that dissolution flattens $n(a)$ for smaller bubbles while buoyancy

steepens $n(a)$ for larger bubbles. Other studies that have attempted to measure bubbles under breaking waves have reported bubble size distributions that peak around 20-30 µm, above which they follow a power law and below which they decrease with decreasing bubble size (Blenkinsopp and Chaplin, 2010; Vagle and Farmer, 1992). Both dissolution and buoyancy are likely contributing to the spatial evolution of the bubble size distribution observed in the present study.

4.4.4 Discrepancy between measurement methods

One concerning observation from this study is that the magnitude of $n(a)$ calculated from volume backscattering is significantly lower than the bubble densities reported in Chapter 3, which were calculated from broadband attenuation (Fig. 4.13). At comparable depths in the Connecticut River ebb plume front on the same day, the volume backscattering measurements yielded bubble size distributions approximately 1.5 orders of magnitude lower than the attenuation measurement instrument described in Chapter 3. The backscattering yielded $n(a)$ curves that agreed reasonably well with the -2.3 power law expected for quiescent bubbles under breaking waves (Deane and Stokes, 2002), while the attenuation yielded $n(a)$ curves with a shallower slope (Fig. 4.13).

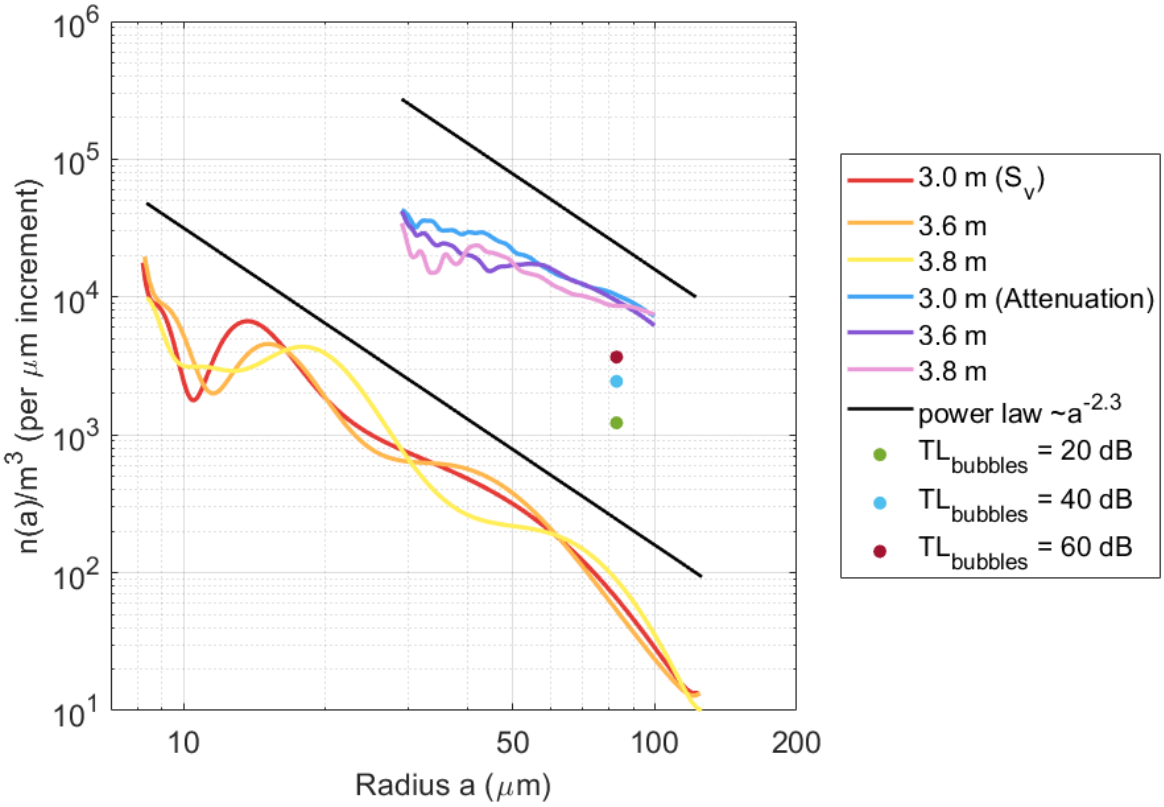

Figure 4.13 Bubble size distributions in the Connecticut River front from 3-3.8 m depth measured via volume backscattering (red, orange, yellow) and via excess attenuation in Chapter 3 (blue, purple, pink). Rough estimates of the density of 83 µm bubbles derived from excess losses in seafloor scattering strength ($TL_{bubbles}$) at 38 kHz are also included.

Bassett et al. (2023) published observations of the bubble size distribution of a front in the James River estuary, where the processes driving the bubble distribution should be broadly similar to those of the Connecticut River estuary. They calculated $n(a)$ from broadband backscatter at a range of frequencies overlapping with the range used in the present study, and the slope and magnitude of their observed bubble size distribution agree reasonably well with the observations presented here. To build confidence in my estimates of $n(a)$ from attenuation spectra, consider the laboratory results presented in Chapter 3 (Section 3.6). The magnitude and shape of the size distribution of bubbles estimated from attenuation under a breaking wave agreed well with published observations of quiescent bubbles (e.g., Deane and Stokes, 2002; Harb and Foroutan, 2019). Given the good agreement of both measurement methods used in this dissertation with previous studies, there might be a systematic issue causing the disparity between the two methods for field measurements.

A potential reason for the discrepancy between measurement methods is that a sampling bias resulted in measurements of different parts of the front where the bubble size distribution was different. The research vessel steamed continuously during backscattering measurements but held a stationary position over the front during attenuation measurements. Although an unlikely source of error, it is worth mentioning the possibility that attenuation measurements were contaminated with extra bubbles generated in the ship's wake while it was repositioning. During continuous transects over the front with the echosounders pinging, there was frequent signal dropout suggesting the presence of dense bubble clouds. There was also variability in the amount of excess transmission loss impacting the scattering strength of the seafloor in the 38 kHz band, which ranged from 20 to more than 60 dB of excess loss at the downwelling zone where the bubble population was densest (Fig. 4.7.b-d).

Consider the measured seafloor backscattering spectrum $S_{v,measured}$ as the sum of backscattering from the seafloor ($S_{v,seafloor}$), and excess transmission loss accrued from two-way travel through the bubble cloud ($TL_{bubbles}$):

$$S_{v,measured} = S_{v,seafloor} - TL_{bubbles}. \quad (4.4)$$

The seafloor scattering strength at the front in the 38 kHz band drops by approximately 20 dB in Front 1, 60 dB in Front 2, and 40 dB in Front 3 (Fig. 4.7). Bassett and Lavery (2021) proposed that because these drops in seafloor scattering strength occur only near the downwelling zone and not further downstream, this excess attenuation is likely caused by a high density of bubbles concentrated high in the water column. In this study, I have not reported bubble size distributions estimated from volume backscattering in this part of the front because the data were impacted by significant signal dropout. However, it is possible that my measurements of broadband excess attenuation (Section 3.7) were obtained in this section of the front.

As an exercise, assume that the excess losses in seafloor scattering strength accrued in the first 3 m of depth. Since the echosounders were fixed at a depth of 0.79 m, the two-way travel path of the signal would be $2 \times (3 - 0.79) = 4.4$ m long. If I estimate 60 dB of seafloor scattering loss at 38 kHz, then I can calculate a rough attenuation rate as $60/4.42 = 14$ dB/m at 38 kHz, which can be plugged into the Resonant Bubble Approximation (Eq. 4.3) to obtain a corresponding density of bubbles of radius 83 µm. This calculation was repeated for 20, 40, and 60 dB of drop in the seafloor scattering strength and yielded a range of estimates of the bubble density that are significantly closer to that measured with the

bubble attenuation instrument (Fig. 4.13). This is only a rough estimate, as the bubble size distribution may not be uniform from the surface to 3 m deep (Baschek et al., 2006) and because of the signal dropout in the backscatter, there is uncertainty over what spatial scales $TL_{bubbles}$ is accrued. For instance, the same total losses accrued over just the 0.5-m blanking distance of the echosounder yields a higher estimated density of 83 μm radius bubbles in excellent agreement with that measured with the attenuation instrument. A targeted future study is necessary to test the hypothesis that a sampling bias led to the disparity in bubble size distributions because the attenuation and backscattering observations were taken at different parts of the front. If true, the findings of this chapter would align with the theory proposed by Bassett and Lavery (2021).

4.5 Summary & Conclusions

The goals of this chapter were to 1) investigate the depth and distance dependence of the density and size distribution of microbubbles in the Connecticut River ebb plume front, and 2) relate depth- and distance-dependent trends in the bubble size distribution to the hydrodynamics of the front. Broadband backscattering measurements were collected with a shipboard system as it passed over the front, and mean volume backscattering spectra were calculated for a series of bins ranging in depth at the front and evenly spaced from the front out to the tail of the associated bubble cloud (Fig. 4.6). Volume backscattering spectra were inverted to estimate bubble size distributions via an iterative method based on Caruthers et al. (1999).

Bubbles generated by breaking surface waves at the front are subducted by a downwelling current and advected landward behind the front. I observed that the bubble size distribution largely maintains its shape and magnitude with depth in the downwelling zone of the front, suggesting that bubbles initially entrained at the surface remain entrained to around 3.5 m depth. I also observed that with increasing distance behind the front, the bubble size distribution steepens slightly and decreases in magnitude, suggesting that bubbles are lost to buoyancy and dissolution as they are advected, with larger bubbles rising out most quickly and smaller bubbles entrained in turbulent mixing along the sharp density gradient.

Surprisingly, there was a concerning disparity in the bubble size distribution estimated from volume backscattering measurements versus broadband excess attenuation. This was proposed to come from a sampling bias arising from signal dropout caused by high concentrations of shallow bubbles in the downwelling zone. I hypothesize that this may have led to volume backscattering observations being taken at regions of the front where the bubble density was lower than where excess attenuation was measured. An additional field experiment is needed to investigate this theory.

The observations presented in this chapter suggest that while bubbles in the Connecticut River front are generated by breaking waves in a process like that in the open ocean, frontal dynamics play an important part in driving the density and size distribution of these bubbles once entrained. Further work is needed to better understand spatial and temporal variability of the bubble distribution along the front as well as to evaluate the performance of different measurement approaches. A better understanding of bubbles in tidal fronts and the factors that drive them will permit better constrained estimates of their contribution to the aeration of estuarine waters as well as better predictions of how frontal structures might impact acoustical operations in coastal environments.

5 Conclusion

5.1 Summary of contributions and significance

The development of broadband acoustical technology opened the door to a wide range of biological, physical, and yet-to-be-explored oceanographic applications. Accurate sound scattering models form the foundation of acoustical oceanography as they are crucial for giving predictive power and meaning to measurements. Once a scattering model has been developed and verified, it may be used to quantitatively interpret acoustical data, thereby offering a means to survey vast oceanographic environments with an efficiency unmatched by other sampling methods. While many advancements in our understanding of the marine environment have been made possible by broadband acoustics, there remain countless gaps in our understanding of sound scattering processes in the ocean as well as unanswered scientific questions well suited to acoustical solutions. This dissertation addressed several of these knowledge gaps.

5.1.1 Gelatinous organisms

As the role of gelatinous organisms as both predator and prey becomes increasingly appreciated, they remain acoustically understudied compared to other types of animals. Jellies are ubiquitous members of marine ecosystems potentially accounting for a significant proportion of global marine biomass, but estimates of their abundance are not well constrained because they are so difficult to sample via traditional methods. Little effort has been made to understand sound scattering from gelatinous organisms so that they may be better incorporated into biomass estimates. Additionally, most acoustical studies have employed narrowband signals, hence missing out on the additional resolution and characterization information offered by broadband techniques.

To address these problems in Chapter 2, a sound scattering model was developed for a common species of scyphozoan jelly using the Distorted Wave Born Approximation (DWBA) and a simplified 3-D medusa bell shape that can be adjusted to reflect a range of flexion states. Broadband target strength (TS) measurements were collected from live individuals in a laboratory setting to verify the sound scattering model, and changes to the scattering behavior due to swimming pulsations were examined. This model is a necessary step toward being able to quantify jellies in the field. Since gelatinous organisms commonly occur in mixed aggregations containing multiple types of scatterers, the ability to acoustically distinguish between jellies and other organisms is critical for constraining biomass estimates inferred from volume backscattering measurements as is common practice in fisheries. In environments dominated by gelatinous organisms, a deep understanding of jelly TS will permit more rigorous population assessments. Broadly, the work presented in Chapter 2 is an important step toward better understanding the biomass, distribution, and dynamics of jelly populations.

5.1.2 Bubbles in estuarine fronts

Oceanic frontal structures are important contributors to vertical mixing. In estuaries, fronts that form at the convergence of brackish river outflow with surrounding seawater enhance surface wave breaking and form narrow zones of sustained downwelling that entrain dense and deeply penetrating microbubble plumes. This process has been estimated to contribute a significant proportion of air-sea gas exchange in these coastal environments, provided that the density and size distribution of bubbles in a front are known (Baschek et al., 2006). Though multiple studies have measured the bubble size distributions under breaking waves in the open ocean, few have attempted to measure bubble size distributions in estuarine fronts. This raises questions about what the bubble size distributions are in fronts and how frontal bubble populations are impacted by the complex flow structure in these highly stratified environments. Chapters 3 and 4 addressed these questions within the context of the tidal ebb plume front that forms in the Connecticut River estuary.

In Chapter 3, a towable instrument was developed to measure excess attenuation from bubbles from which bubble size distributions could be inferred. The instrument was tested by measuring bubbles under breaking waves in a laboratory wave tank and deployed in the field to measure bubbles in the Connecticut River front. The density of bubbles in the front decreased a small amount with depth, suggesting that many bubbles generated at the surface are subducted. The instrument described in this chapter is towable from a research vessel and thus developed specifically for studying bubbles in tidal fronts. With some minor improvements, this instrument will enable more rigorous and high-resolution measurements to address more complex questions about the distribution of bubbles in fronts.

Chapter 4 examined the spatial trends of the bubble distribution with depth and horizontal distance from the front. Measurements of broadband volume backscattering at a series of locations relative to the front were inverted for the bubble size distribution using an adapted version of the iterative method described by Caruthers et al. (1999). In the downwelling zone of the front, the bubble distribution decreased in magnitude while maintaining its shape up to about 3.5 m depth. The bubble size distribution was observed to decrease in magnitude and steepen with distance away from the downwelling zone. A steepening of the bubble size distribution suggests the loss of larger bubbles due to buoyancy while a uniform decrease in the distribution suggests that dissolution is at play. The results from this chapter suggest that a combination of buoyancy and dissolution could be driving the evolution of the bubble distribution in and behind the front. These findings may be used to inform estimates of bubble-mediated air-sea gas exchange due to the front. Observations of excess transmission loss due to bubbles at the front may also inform best practices for acoustical operations in estuarine environments where tidal fronts commonly occur.

5.1.3 List of contributions

The contributions made by this dissertation to the field of acoustical oceanography are outlined below:

Chapter 2: Broadband backscattering from scyphozoan jellyfish	• Developed a physics-based 3-D sound scattering model for a gelatinous organism and verified it with controlled laboratory measurements. • Collected broadband target strength measurements of a gelatinous organism. • Predicted and verified changes in scattering behavior based on flexion state during swimming pulsations.
Chapter 3: Measuring the bubble size distribution in an estuarine front via broadband attenuation	• Developed a towable instrument specifically for measuring broadband excess attenuation from bubbles. • Collected broadband observations of the bubble size distribution in the Connecticut River tidal ebb plume front.
Chapter 4: Spatial trends of the bubble size distribution in an estuarine front	• Described observations of spatial trends in the bubbles size distribution of the Connecticut River tidal ebb plume front within the context of frontal kinematics. • Hypothesized that spatial evolution of the bubble distribution may be driven by both kinematics and dissolution. • Observed a discrepancy between bubble size distributions estimated from volume backscattering and excess attenuation and proposed that this could be due to a sampling bias.

5.2 Recommendations for future work

5.2.1 Scattering models for gelatinous organisms

Further development of the jellyfish sound scattering model is needed for the model to be fully functional. Experimental verification of the model's orientation dependence is a high priority before field-based use. Once orientation dependence is accounted for, the model may be put to the test using an approach similar on that of Lavery et al. (2007) where volume backscattering measurements of a population of jellies are compared with predicted volume backscattering spectra based on parameters measured via a different sampling method such as trawling or imaging.

Another direction for this research is to apply the modeling framework described in Chapter 2 to another species of gelatinous organism. One advantage of this model is that it can be tuned to any shape, size, or orientation. Medusae exhibit diverse morphologies, and different species may be of

interest depending on geographic location. Other ubiquitous jellies such as ctenophores and salps currently lack rigorous sound scattering models.

5.2.2 Understanding bubbles in estuarine fronts

The work presented in Chapters 3 and 4 opens many doors for future work toward understanding the distribution of bubbles in estuarine tidal fronts and further developing the measurement techniques described. While the initial measurements of the bubble size distribution and observed trends are valuable, many questions remain that will require measurements of more complex features of the front and better-informed sampling strategies.

One reason that shipboard backscattering measurements were collected in conjunction with the attenuation instrument was so that the two methods could be compared to build confidence in the obtained bubble size distributions. However, there was a concerning discrepancy between the magnitude of the bubble size distributions measured by both methods, which I speculate could be due to a sampling bias that led to significantly higher measurements of bubble density taken with the attenuation instrument than with volume backscattering. An additional field experiment is crucial to establishing a basis for agreement between the two measurement methods. I propose a targeted sampling strategy involving systematic transects over the front with both measurement systems collecting data concurrently, including both repeated transects over the same section of the front to obtain near-identical replicates and a lawnmower pattern sampling along the front to investigate spatial variability. Extra care must be taken to ensure that the attenuation instrument is towed at a depth below the blanking range of the echosounders, and I recommend collecting long-time data files for the attenuation instrument as described in Section 3.4. A single several-minute file could be collected for each transect, pausing in between transects to allow time for each file to write to the data acquisition laptop. This sampling strategy would allow backscatter and attenuation measurements to be collocated so that they may be compared directly, and a continuously moving research vessel would diminish any possibility of measurement contamination by ship wake. It might also be worthwhile to repeat the measurements with various spacing of the components of the attenuation instrument to ensure good quality field measurements without fully attenuated or saturated signals. A separate, controlled study investigating the effect of different spacings between the sources and receivers in combination with varying transit power could be helpful before attempting to survey a tidal front again, as different arrangements may be needed to measure different sections of the front.

Once measurement procedures are optimized and greater confidence is built in their accuracy, future studies may consider investigating the variability of the bubble distribution parallel to the front as well as the time evolution of the bubble population as the front develops. Incorporation of imaging methods for ground-truthing acoustical measurements would be an additional asset to this work. I attempted to complement my acoustical measurements with holographic image data, however the estuary proved to be too turbid to distinguish bubbles in the images collected (Appendix B). Future work might focus on developing an optical or other technique for measuring bubbles in turbid environments in conjunction with acoustics. Hopefully, future studies in the Connecticut River estuary will be subject to calmer weather conditions to reduce the possibility of confusion between bubbles associated with the front and bubbles associated with breaking surface waves.

5.3 Closing comments

This dissertation presents several contributions to the field of acoustical oceanography. A sound scattering model for a vastly understudied organism has been added to the existing library of scattering models for marine animals. I have built upon existing techniques for acoustically measuring microbubbles and used them to deepen our understanding of bubbles entrained in estuarine fronts. These contributions are not necessarily groundbreaking, but they help propel the field forward. The insights gained from this dissertation have implications for our ability to quantify marine resources, monitor the health of marine ecosystems, better understand air-sea interactions, and ensure effective operation in dynamic coastal environments. Even the most incremental developments in our understanding of the ocean are more important now than ever during these uncertain times for the health of our planet. Acoustical technology unlocked our ability to sense and observe the ocean in many ways, and it could play an integral role in creating a sustainable future for humankind.

Appendix

A. Calculating indirectly measured size parameters

In the following formulations, the subscript 'e' and superscript (e) refer to the bell's expanded position; the subscript 'c' and superscript (c) indicate that the bell is in a contracted state. The expanded bell diameter (W_e) and vertical thickness (t_e) were the only size parameters measured directly in this study. Other parameters necessary for constructing the stacked spherical caps model shape and a range of contracted positions were derived and calculated using geometric formulas, assuming the bell volume is conserved (Fig. 3). Recall that the expanded bell height, $H_{top}^{(e)}$, is obtained from W_e via the fineness ratio $f_{ratio}^{(e)} = W_e/H_{top}^{(e)}$. Then, the height of the bottom face, $H_{bot}^{(e)} = H_{top}^{(e)} - t_e$. From there, the radii of curvature for the top and bottom faces, r_{top} and r_{bot}, respectively, follow as

$$r_{top} = \frac{H_{top}^{(\mathrm{e})}}{2} + \frac{W_e^2}{8H_{top}^{(e)}}\,;\, r_{bot} = \frac{H_{bot}^{(\mathrm{e})}}{2} + \frac{W_{\mathrm{e}}^2}{8H_{bot}^{(\mathrm{e})}}. \tag{A.1}$$

The volumes of the spherical caps forming the top and bottom faces of the expanded bell, $V_{top}^{(e)}$ and $V_{bot}^{(e)}$, are then calculated; the difference between them is the total volume of the jelly's bell, V_0:

$$V_{top}^{(\mathrm{e})} = \frac{\pi}{6} H_{top}^{(e)} \left[3\left(\frac{W_e}{2}\right)^2 + H_{top}^{(\mathrm{e})\,2} \right] \tag{A.2a}$$

$$V_{bot}^{(\mathrm{e})} = \frac{\pi}{6} H_{bot}^{(\mathrm{e})} \left[3\left(\frac{W_e}{2}\right)^2 + H_{bot}^{(\mathrm{e})\,2} \right] \tag{A.2b}$$

$$V_0 = V_{top} - V_{bot}. \tag{A.2c}$$

where V_0 is a conserved quantity across all swimming positions. From this foundation, size parameters may be obtained for another fineness ratio, $f_{ratio}^{(c)} = W_c/H_{top}^{(c)}$. Ideally, W_c is obtained from the ratio $W_{ratio} = W_e/W_c$ determined by visual data of the jelly's swimming pulsations. In hypothetical cases, such as for swimming-averaged model predictions, W_{ratio} is assumed to scale linearly with f_{ratio}. From these ratios, size parameters for the contracted top face can be obtained as

$$W_{\mathrm{c}} = W_{\mathrm{e}}/W_{ratio} \tag{A.3a}$$

$$H_{top}^{(\mathrm{c})} = W_{\mathrm{c}}/f_{ratio}^{(\mathrm{c})} \tag{A.3b}$$

$$V_{top}^{(\mathrm{c})} = \frac{\pi}{6} H_{top}^{(\mathrm{c})} \left[3\left(\frac{W_c}{2}\right)^2 + H_{top}^{(\mathrm{c})\,2} \right]. \tag{A.4c}$$

Then, volume conservation may be used to obtain a cubic polynomial:

$$V_0 = V_{top}^{(\mathrm{c})} - V_{bot}^{(\mathrm{c})} = V_{top}^{(\mathrm{c})} - \frac{\pi}{6} H_{bot}^{(\mathrm{c})} \left[3 \left(\frac{W_\mathrm{c}}{2} \right)^2 + {H_{bot}^{(\mathrm{c})}}^2 \right] \tag{A.4}$$

that can be solved for $H_{bot}^{(c)}$ computationally. Finally, the thickness of the contracted bell is obtained as

$$t_\mathrm{c} = H_{top}^{(c)} - H_{bot}^{(c)} \tag{A.5}$$

and the contracted bell shape can be digitally constructed and integrated via the DWBA formulation.

B. Holographic measurements of bubble size distributions

A holographic imaging system was deployed alongside the bubble attenuation measurement system (Chapter 3) with the intention of using image data to ground-truth the acoustical measurements of bubble size distributions. Digital Inline Holographic Microscopy (DIHM) has been used to measure and map small-scale 3-D distributions of bubble streams in the lab (Shao, 2019; Tian et al., 2010) as well as in a field setting to characterize bubble distributions in a ship wake (Talapatra et al., 2012), but it has yet to be used more broadly for oceanographic measurements. Due to its ability to discriminate between bubbles and particulates (O'Hern et al., 1988), holographic imaging could be a useful tool for quantifying bubbles in turbid environments such as estuaries. The advantage of using digital inline holography (DIH) to detect bubbles is that it produces high-resolution 3-D images of a known volume. The main disadvantage is that processing holographic data is very computationally intensive.

The holographic system was custom built by Seascan Inc. (Falmouth, Massachusetts, USA). The system consists of a 16-megapixel camera and a 658-nm wavelength collimated laser light source with an adjustable separation distance (Fig. B.1). Objects in the laser beam diffract light, producing images of the resulting interference pattern with a pixel size of 7.4 µm. The system was mounted with 5 cm of separation between source and receiver (FIG B.2) and tested in a lab using a rectangular table-top tank and in an enclosed testing well on the dock of the Woods Hole Oceanographic Institution (Woods Hole, Massachusetts, USA). Microbubbles were generated for testing purposes using an electric air pump with the output covered with a piece of dense foam to fragment the outflowing air.

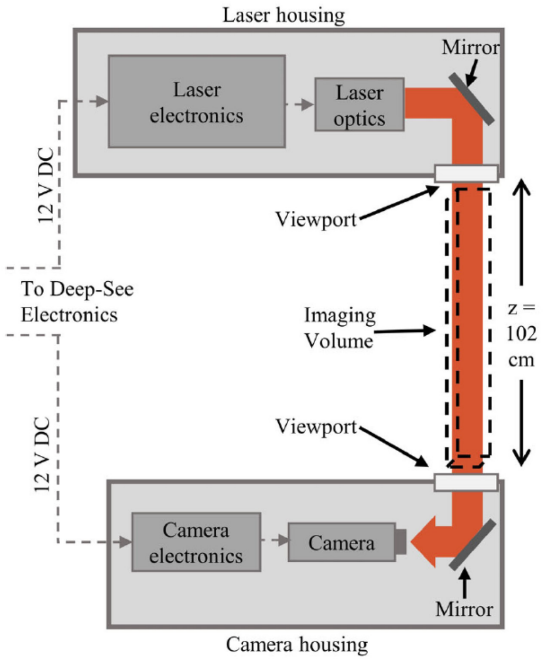

Figure B.1 Schematic diagram of the custom holographic imaging system reproduced from Cotter et al. (2021).

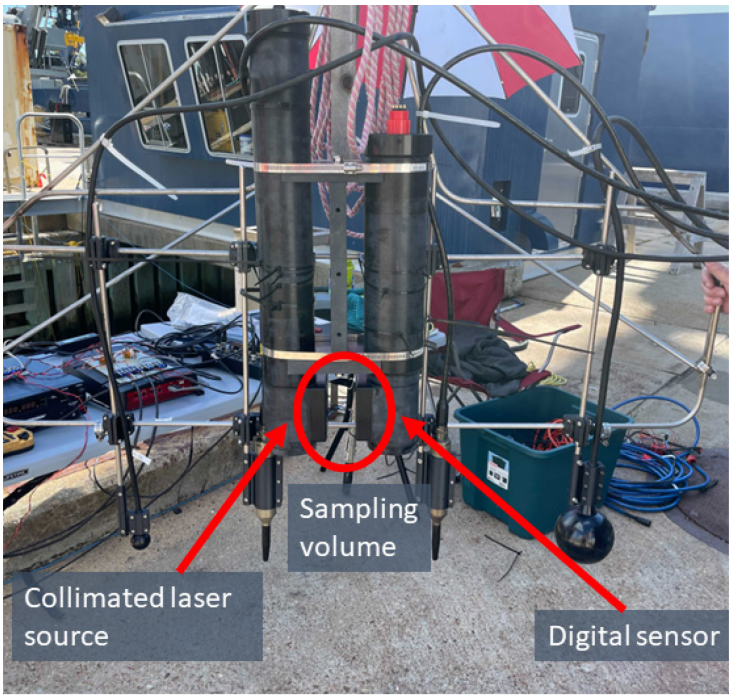

Figure B.2 Holographic camera with 5 cm separation between source and receiver mounted on the bubble attenuation instrument frame (described in Chapter 3) for testing at the Woods Hole Oceanographic Institution (Woods Hole, Massachusetts, USA).

Image data collected by the system were processed using the approach described by Tian et al. (2010). Reconstructions of a hologram are calculated at a range of focus planes between source and receiver and combined to produce a 2-D projection of the minimum intensity value of each pixel. The result is a map of bubble edges from which a size distribution can be obtained (Fig. B.3). An image processing routine was developed to count and size the bubbles in the imaging volume that involves binarizing the minimum intensity projection, area thresholding to reduce noise and omit small non-bubble particulates, and circularity thresholding to detect round bubbles in the image (Fig. B.4). The radii of circular objects detected by the circularity threshold were obtained and the bubble density calculated by dividing the number of bubbles by the sampling volume (Fig. B.5).

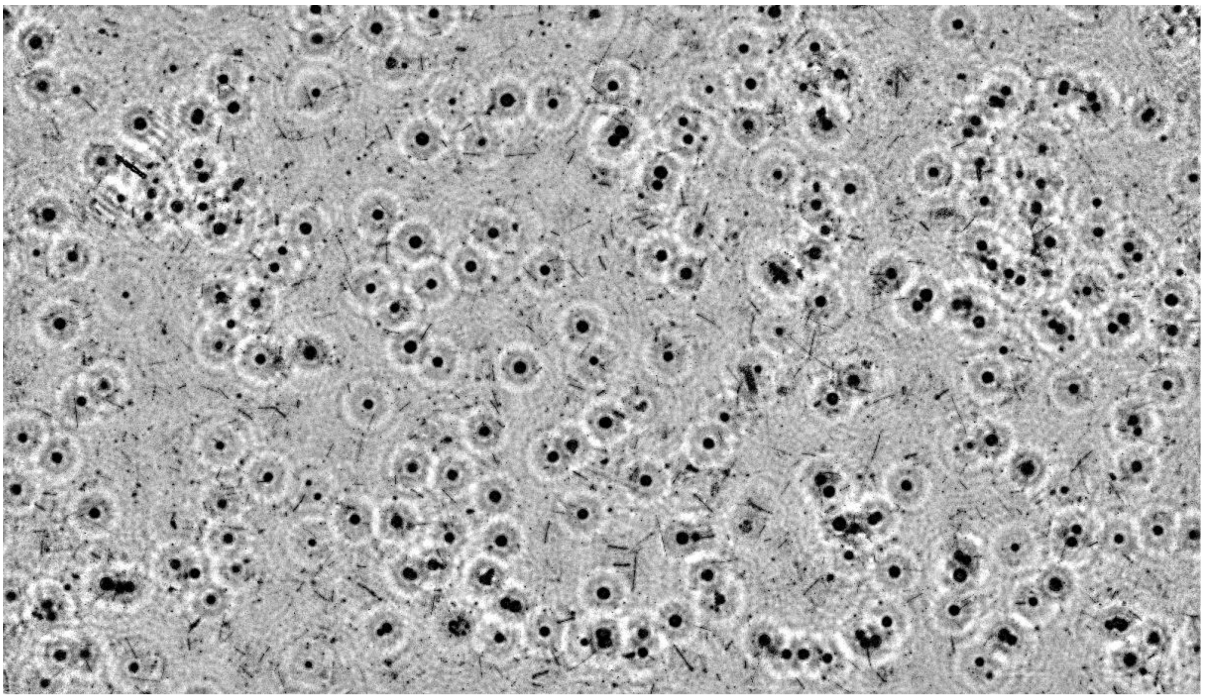

Figure B.3 Minimum intensity projection of a holographic image of bubbles generated in the lab.

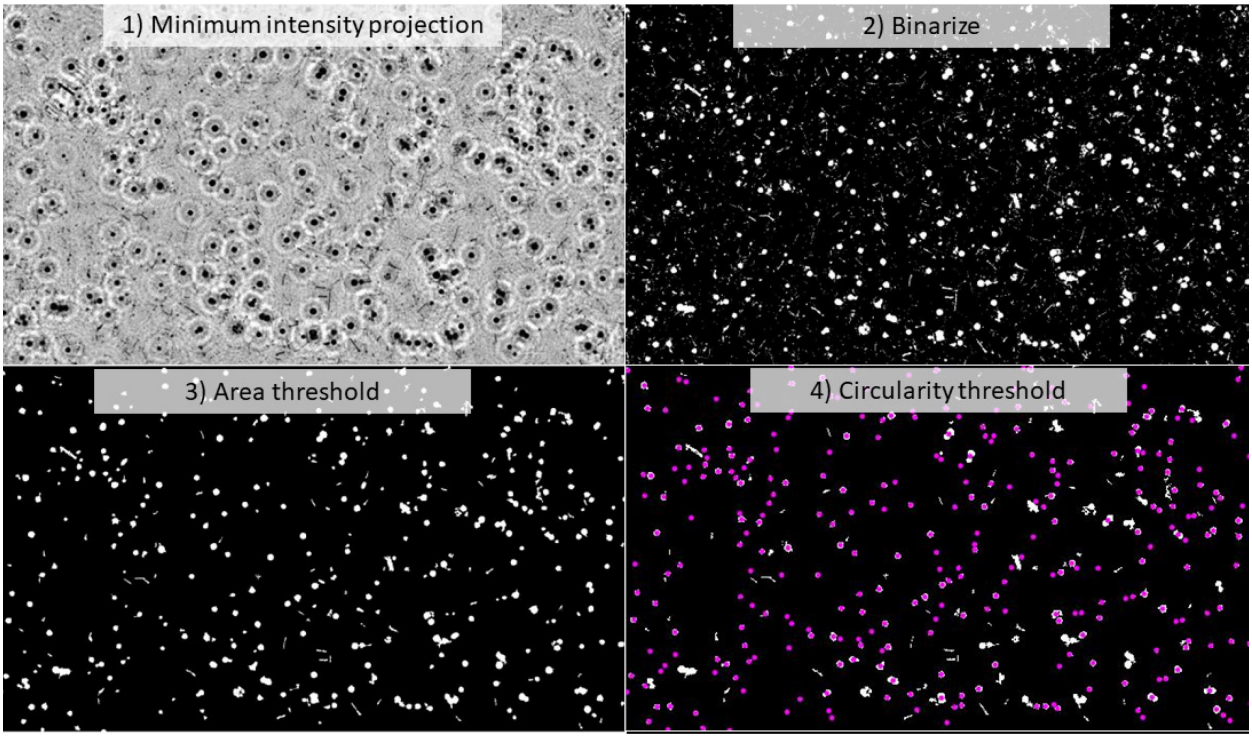

Figure B.4 Steps of holographic image processing routine for detecting and sizing bubbles from a minimum intensity projection.

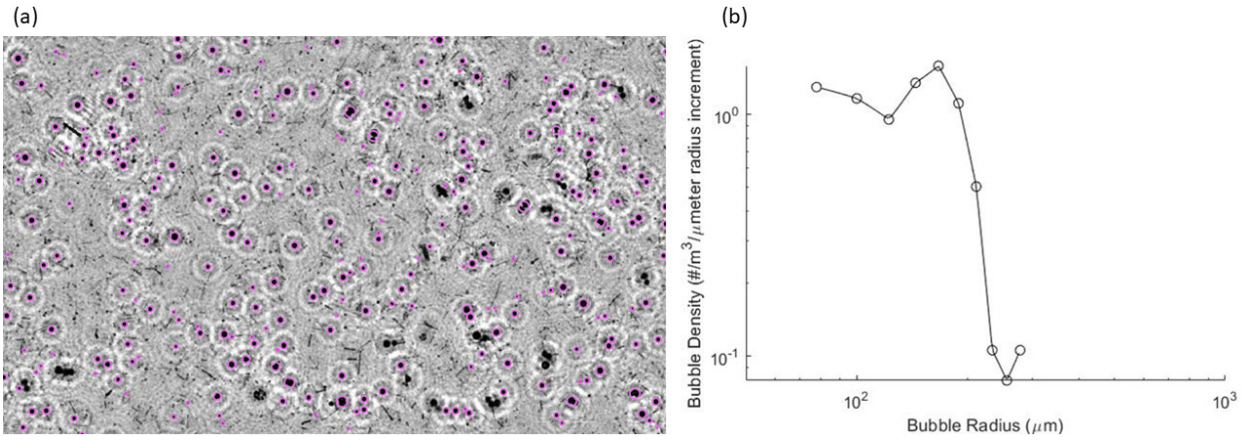

Figure B.5 Left: detected bubbles from a minimum intensity projection indicated with purple circles. Right: corresponding bubble size distribution for lab-generated bubbles.

The holographic imaging system was deployed in the Connecticut River ebb plume front during the October 2021 field campaign. Despite showing promise as a bubble measurement technique during testing, it was impossible to distinguish bubbles in the images in such a turbid and turbulent environment (Fig. B.6). While DIHM has the potential be a valuable method for measuring bubbles in the field, it is probably not well suited to an estuarine setting. In fact, holography might be better suited for studying small-scale turbulence than bubbles. Additional testing side-by-side with acoustical techniques is needed to determine the conditions in which holographic imaging can provide accurate ground-truth bubble measurements.

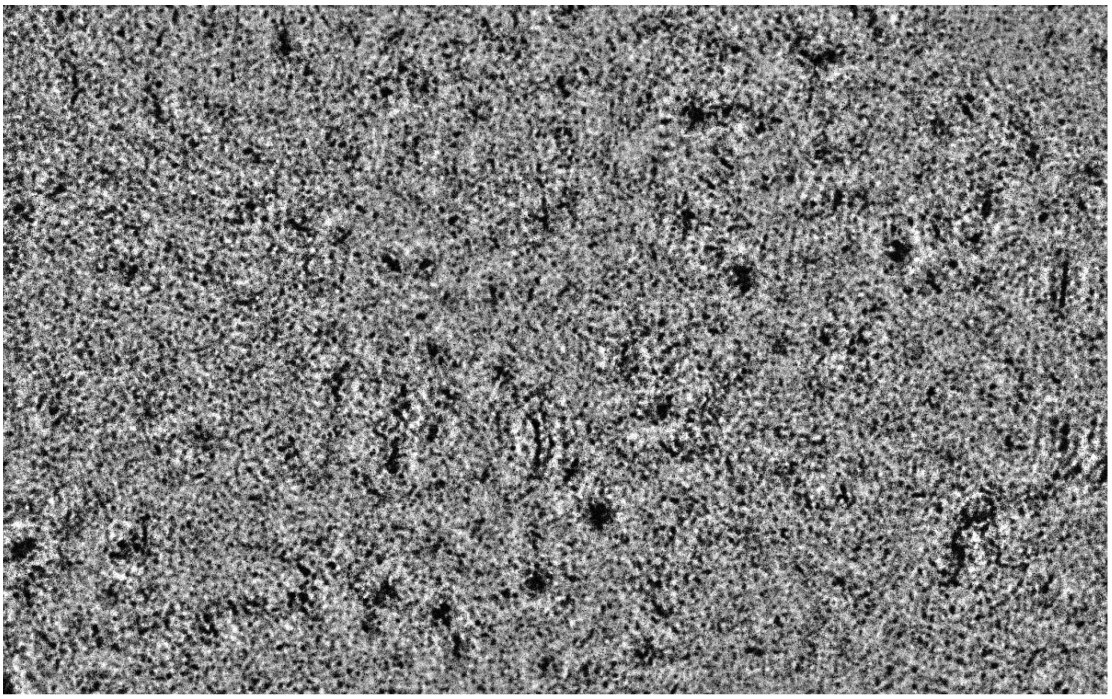

Figure B.6 Minimum intensity projection of a holographic image collected in the Connecticut River tidal ebb plume front.

References

van der A, D. A., van der Zanden, J., O'Donoghue, T., Hurther, D., Cáceres, I., McLelland, S. J., and Ribberink, J. S. (**2017**). "Large-scale laboratory study of breaking wave hydrodynamics over a fixed bar," Journal of Geophysical Research: Oceans, **122**, 3287–3310. doi:10.1002/2016JC012072

Agersted, M. D., Khodabandeloo, B., Liu, Y., Melle, W., and Klevjer, T. A. (**2021**). "Application of an unsupervised clustering algorithm on in situ broadband acoustic data to identify different mesopelagic target types," ICES Journal of Marine Science, **78**, 2907–2921. doi:10.1093/icesjms/fsab167

Agrawal, Y. C., Terray, E. A., Donelan, M. A., Hwang, P. A., Williams, A. J., Drennan, W. M., Kahma, K. K., et al. (**1992**). "Enhanced dissipation of kinetic energy beneath surface waves," Nature, **359**, 219–220. doi:10.1038/359219a0

Ainslie, M. A. (**2005**). "Effect of wind-generated bubbles on fixed range acoustic attenuation in shallow water at 1–4kHz," The Journal of the Acoustical Society of America, **118**, 3513–3523. doi:10.1121/1.2114527

Aksnes, D. L., Røstad, A., Kaartvedt, S., Martinez, U., Duarte, C. M., and Irigoien, X. (**2017**). "Light penetration structures the deep acoustic scattering layers in the global ocean," Sci. Adv., **3**, e1602468. doi:10.1126/sciadv.1602468

Alvarez Colombo, G., Benović, A., Malej, A., Lučić, D., Makovec, T., Onofri, V., Acha, M., et al. (**2008**). "Acoustic survey of a jellyfish-dominated ecosystem (Mljet Island, Croatia)," Hydrobiologia, **616**, 99–111. doi:10.1007/s10750-008-9587-6

Andersen, L. N., Chu, D., Heimvoll, H., Korneliussen, R., Macaulay, G. J., and Ona, E. (**2021**). "Quantitative processing of broadband data as implemented in a scientific splitbeam echosounder." doi:10.48550/arXiv.2104.07248

Andreeva, I. B., and Belousov, A. V. (**1996**). "Multiple sound scattering by densely packed shoals of marine animals," ICES Journal of Marine Science, **53**, 323–327. doi:10.1006/jmsc.1996.0043

Annalakshmi, G., Murugan, S. S., and Ramasundaram, K. (**2019**). "Side Scan Sonar Images Based Ocean Bottom Sediment Classification," 2019 International Symposium on Ocean Technology (SYMPOL), 138–144. Presented at the 2019 International Symposium on Ocean Technology (SYMPOL). doi:10.1109/SYMPOL48207.2019.9005290

Baldy, S., and Bourguel, M. (**1985**). "Measurements of bubbles in a stationary field of breaking waves by a laser-based single-particle scattering technique," Journal of Geophysical Research: Oceans, **90**, 1037–1047. doi:10.1029/JC090iC01p01037

Baliarsingh, S. K., Lotliker, A. A., Srichandan, S., Samanta, A., Kumar, N., and Nair, T. M. B. (**2020**). "A review of jellyfish aggregations, focusing on India's coastal waters," Ecol Process, **9**, 58. doi:10.1186/s13717-020-00268-z

Båmstedt, U., Kaartvedt, S., and Youngbluth, M. (**2003**). "An evaluation of acoustic and video methods to estimate the abundance and vertical distribution of jellyfish," Journal of Plankton Research, **25**, 1307–1318. doi:10.1093/plankt/fbg084

Baschek, B., Farmer, D. M., and Garrett, C. (**2006**). "Tidal fronts and their role in air-sea gas exchange," J Mar Res, **64**, 483–515. doi:10.1357/002224006778715766

Bassett, C., De Robertis, A., and Wilson, C. D. (**2018**). "Broadband echosounder measurements of the frequency response of fishes and euphausiids in the Gulf of Alaska," ICES Journal of Marine Science, **75**, 1131–1142. doi:10.1093/icesjms/fsx204

Bassett, C., and Lavery, A. (**2021**). “Observations of high-frequency acoustic attenuation due to bubble entrainment at estuarine fronts,” Seattle, Washington, 005001. Presented at the 181st Meeting of the Acoustical Society of America. doi:10.1121/2.0001539

Bassett, C., Lavery, A. C., Ralston, D., Geyer, W. R., Jurisa, J. T., Thomson, J., Honegger, D. A., et al. (**2023**). “Acoustic backscattering at a tidal intrusion front,” Progress in Oceanography, , doi: 10.1016/j.pocean.2023.103167. doi:10.1016/j.pocean.2023.103167

Bassett, C., Lavery, A. C., Stanton, T. K., and Cotter, E. D. (**2020**). “Frequency- and depth-dependent target strength measurements of individual mesopelagic scatterers,” The Journal of the Acoustical Society of America, **148**, EL153–EL158. doi:10.1121/10.0001745

Bayha, K. M., Collins, A. G., and Gaffney, P. M. (**2017**). “Multigene phylogeny of the scyphozoan jellyfish family Pelagiidae reveals that the common U.S. Atlantic sea nettle comprises two distinct species (Chrysaora quinquecirrha and C. chesapeakei),” PeerJ, **5**, e3863. doi:10.7717/peerj.3863

Benoit-Bird, K. J., and Waluk, C. M. (**2020**). “Exploring the promise of broadband fisheries echosounders for species discrimination with quantitative assessment of data processing effects,” The Journal of the Acoustical Society of America, **147**, 411–427. doi:10.1121/10.0000594

Blanluet, A., Doray, M., Berger, L., Romagnan, J.-B., Le Bouffant, N., Lehuta, S., and Petitgas, P. (**2019**). “Characterization of sound scattering layers in the Bay of Biscay using broadband acoustics, nets and video,” (S. Ntalampiras, Ed.) PLoS ONE, **14**, e0223618. doi:10.1371/journal.pone.0223618

Blenkinsopp, C. E., and Chaplin, J. R. (**2010**). “Bubble Size Measurements in Breaking Waves Using Optical Fiber Phase Detection Probes,” IEEE Journal of Oceanic Engineering, **35**, 388–401. Presented at the IEEE Journal of Oceanic Engineering. doi:10.1109/JOE.2010.2044940

Brierley, A. S., Axelsen, B. E., Boyer, D. C., Lynam, C. P., Didcock, C. A., Boyer, H. J., Sparks, C. A., et al. (**2004**). “Single-target echo detections of jellyfish,” ICES Journal of Marine Science, **61**, 383–393. doi:10.1016/j.icesjms.2003.12.008

Brierley, A. S., Axelsen, B. E., Buecher, E., Sparks, C. A., Boyer, H., and Gibbons, M. J. (**2001**). “Acoustic observations of jellyfish in the Namibian Benguela,” Marine Ecology Progress Series, **210**, 55–66. doi:10.3354/meps210055

Brotz, L., Cheung, W. W. L., Kleisner, K., Pakhomov, E., and Pauly, D. (**2012**). “Increasing jellyfish populations: trends in Large Marine Ecosystems,” Hydrobiologia, **690**, 3–20. doi:10.1007/s10750-012-1039-7

Buesseler, K. O., Lamborg, C. H., Boyd, P. W., Lam, P. J., Trull, T. W., Bidigare, R. R., Bishop, J. K. B., et al. (**2007**). “Revisiting Carbon Flux Through the Ocean’s Twilight Zone,” Science, **316**, 567–570. doi:10.1126/science.1137959

Cartmill, J. W., and Yang Su, M. (**1993**). “Bubble size distribution under saltwater and freshwater breaking waves,” Dynamics of Atmospheres and Oceans, American Geophysical Union Ocean Sciences Meeting, **20**, 25–31. doi:10.1016/0377-0265(93)90046-A

Caruthers, J. W., Elmore, P. A., Novarini, J. C., and Goodman, R. R. (**1999**). “An iterative approach for approximating bubble distributions from attenuation measurements,” The Journal of the Acoustical Society of America, **106**, 185–189. doi:10.1121/1.427047

Chua, G., Chitre, M., and Deane, G. B. (**2021**). “Long-Lived Bubbles and Their Impact on Underwater Acoustic Communication,” IEEE Journal of Oceanic Engineering, **46**, 1008–1023. Presented at the IEEE Journal of Oceanic Engineering. doi:10.1109/JOE.2020.3028396

Cimino, M., Patris, S., Ucharm, G., Bell, L., and Terrill, E. (**2018**). “Jellyfish distribution and abundance in relation to the physical habitat of Jellyfish Lake, Palau,” Journal of Tropical Ecology, **34**, 1–15. doi:10.1017/S0266467418000044

Clay, C. S., and Medwin, H. (**1964**). “High-Frequency Acoustical Reverberation from a Rough-Sea Surface,” The Journal of the Acoustical Society of America, **36**, 2131–2134. doi:10.1121/1.1919333

Clinton, M., Ferrier, D. E. K., Martin, S. A. M., and Brierley, A. S. (**2021**). “Impacts of jellyfish on marine cage aquaculture: an overview of existing knowledge and the challenges to finfish health,” ICES Journal of Marine Science, doi:10.1093/icesjms/fsaa254

Commander, K. W., and McDonald, R. J. (**1991**). “Finite-element solution of the inverse problem in bubble swarm acoustics,” The Journal of the Acoustical Society of America, **89**, 592–597. doi:10.1121/1.400671

Cotter, E., Bassett, C., and Lavery, A. (**2021a**). “Classification of broadband target spectra in the mesopelagic using physics-informed machine learninga),” The Journal of the Acoustical Society of America, **149**, 3889–3901. doi:10.1121/10.0005114

Cotter, E., Fischell, E., and Lavery, A. (**2021b**). “Computationally efficient processing of in situ underwater digital holograms,” Limnology & Ocean Methods, **19**, 476–487. doi:10.1002/lom3.10438

Crawford, G. B., and Farmer, D. M. (**1987**). “On the spatial distribution of ocean bubbles,” Journal of Geophysical Research: Oceans, **92**, 8231–8243. doi:10.1029/JC092iC08p08231

Cromwell, T., and Reid, J. L. (**1956**). “A Study of Oceanic Fronts,” Tellus, **8**, 94–101. doi:10.1111/j.2153-3490.1956.tb01198.x

Czerski, H. (**2012**). “An Inversion of Acoustical Attenuation Measurements to Deduce Bubble Populations,” Journal of Atmospheric and Oceanic Technology, **29**, 1139–1148. doi:10.1175/JTECH-D-11-00170.1

Dahl, P. H. (**2003**). “The contribution of bubbles to high-frequency sea surface backscatter: A 24-h time series of field measurements,” The Journal of the Acoustical Society of America, **113**, 769–780. doi:10.1121/1.1532029

Dahl, P. H., Choi, J. W., Williams, N. J., and Graber, H. C. (**2008**). “Field measurements and modeling of attenuation from near-surface bubbles for frequencies 1–20kHz,” The Journal of the Acoustical Society of America, **124**, EL163–EL169. doi:10.1121/1.2963096

D’Asaro, E. A. (**2001**). “Turbulent Vertical Kinetic Energy in the Ocean Mixed Layer,” Journal of Physical Oceanography, **31**, 3530–3537. doi:10.1175/1520-0485(2002)031<3530:TVKEIT>2.0.CO;2

Davison, P. C., Koslow, J. A., and Kloser, R. J. (**2015a**). “Acoustic biomass estimation of mesopelagic fish: backscattering from individuals, populations, and communities,” ICES Journal of Marine Science, **72**, 1413–1424. doi:10.1093/icesjms/fsv023

Davison, P., Lara-Lopez, A., and Anthony Koslow, J. (**2015b**). “Mesopelagic fish biomass in the southern California current ecosystem,” Deep Sea Research Part II: Topical Studies in Oceanography, CCE-LTER: Responses of the California Current Ecosystem to Climate Forcing, **112**, 129–142. doi:10.1016/j.dsr2.2014.10.007

De Robertis, A., and Taylor, K. (**2014**). “In situ target strength measurements of the scyphomedusa Chrysaora melanaster,” Fisheries Research, **153**, 18–23. doi:10.1016/j.fishres.2014.01.002

Deane, G. B. (**1997**). “Sound generation and air entrainment by breaking waves in the surf zone,” The Journal of the Acoustical Society of America, **102**, 2671–2689. doi:10.1121/1.420321

Deane, G. B., Preisig, J. C., and Lavery, A. C. (**2013**). “The Suspension of Large Bubbles Near the Sea Surface by Turbulence and Their Role in Absorbing Forward-Scattered Sound,” IEEE Journal of Oceanic Engineering, **38**, 632–641. Presented at the IEEE Journal of Oceanic Engineering. doi:10.1109/JOE.2013.2257573

Deane, G. B., and Stokes, M. D. (**2002**). “Scale dependence of bubble creation mechanisms in breaking waves,” Nature, **418**, 839–844. doi:10.1038/nature00967

Delatolas, N., MacDonald, D. G., Goodman, L., Whitney, M., Huguenard, K., and Cole, K. (**2023**). “Comparison of structure and turbulent mixing between lateral and leading-edge river plume fronts: Microstructure observations from a T-REMUS AUV,” Estuarine, Coastal and Shelf Science, **283**, 108234. doi:10.1016/j.ecss.2023.108234

Demer, D. A.; Andersen, L. N.; Bassett, C.; Berger, L.; Chu, D.; Condiotty, J.; Cutter, G. R.; Hutton, B.; Korneliussen, R.; Le Bouffant, N.; Macaulay, G.; Michaels, W. L.; Murfin, D.; Pobitzer, A.; Renfree, J. S.; Sessions, T. S.; Stierhoff, K. L.; And T (**2017**). "Report: Evaluation of a wideband echosounder for fisheries and marine ecosystem science." doi: 10.17895/ICES.PUB.2318.

Duarte, C. M., Pitt, K. A., Lucas, C. H., Purcell, J. E., Uye, S., Robinson, K., Brotz, L., et al. (**2013**). "Is global ocean sprawl a cause of jellyfish blooms?," Frontiers in Ecology and the Environment, **11**, 91–97. doi:10.1890/110246

Dunn, M., McGowan-Yallop, C., Pedersen, G., Falk-Petersen, S., Daase, M., Last, K., Langbehn, T. J., et al. (**2023**). "Model-informed classification of broadband acoustic backscatter from zooplankton in an in situ mesocosm." doi:10.1093/icesjms/fsad192

Escobar-Flores, P. C., O'Driscoll, R. L., Montgomery, J. C., Ladroit, Y., and Jendersie, S. (**2020**). "Estimates of density of mesopelagic fish in the Southern Ocean derived from bulk acoustic data collected by ships of opportunity," Polar Biol, **43**, 43–61. doi:10.1007/s00300-019-02611-3

Eyring, C. F., Christensen, R. J., and Raitt, R. W. (**1948**). "Reverberation in the Sea," The Journal of the Acoustical Society of America, **20**, 462–475. doi:10.1121/1.1906399

Farmer, D. M., Vagle, S., and Booth, A. D. (**1998**). "A Free-Flooding Acoustical Resonator for Measurement of Bubble Size Distributions," JOURNAL OF ATMOSPHERIC AND OCEANIC TECHNOLOGY, **15**, 15. doi:10.1175/1520-0426(1998)015%3C1132:AFFARF%3E2.0.CO;2

Foote, K. G. (**1982**). "On multiple scattering in fisheries acoustics," International Council for the Exploration of the Sea.

Foote, K. G. (**1983**). "Linearity of fisheries acoustics, with addition theorems," The Journal of the Acoustical Society of America, **73**, 1932–1940. doi:10.1121/1.389583

Foote, K. G. (**1985**). "Rather-high-frequency sound scattering by swimbladdered fish," The Journal of the Acoustical Society of America, **78**, 688–700. doi:10.1121/1.392438

Foote, K. G., and MacLennan, D. N. (**1984**). "Comparison of copper and tungsten carbide calibration spheres," The Journal of the Acoustical Society of America, **75**, 612–616. doi:10.1121/1.390489

Forland, T. N., Hobæk, H., Ona, E., and Korneliussen, R. J. (**2014**). "Broad bandwidth acoustic backscattering from sandeel—measurements and finite element simulations," ICES Journal of Marine Science, **71**, 1894–1903. doi:10.1093/icesjms/fsu010

Gargett, A. E., and Grosch, C. E. (**2014**). "Turbulence Process Domination under the Combined Forcings of Wind Stress, the Langmuir Vortex Force, and Surface Cooling," Journal of Physical Oceanography, **44**, 44–67. doi:10.1175/JPO-D-13-021.1

Garrett, C., Li, M., and Farmer, D. (**2000**). "The Connection between Bubble Size Spectra and Energy Dissipation Rates in the Upper Ocean," Journal of Physical Oceanography, **30**, 2163–2171. doi:10.1175/1520-0485(2000)030<2163:TCBBSS>2.0.CO;2

Garvine, R. W. (**1974**). "Dynamics of Small-Scale Oceanic Fronts," Journal of Physical Oceanography, **4**, 557–569. doi:10.1175/1520-0485(1974)004<0557:DOSSOF>2.0.CO;2

Garvine, R. W. (**1977**). "Observations of the motion field of the Connecticut River plume," Journal of Geophysical Research (1896-1977), **82**, 441–454. doi:10.1029/JC082i003p00441

Garvine, R. W., and Monk, J. D. (**1974**). "Frontal structure of a river plume," Journal of Geophysical Research (1896-1977), **79**, 2251–2259. doi:10.1029/JC079i015p02251

Gorska, N., Korneliussen, R. J., and Ona, E. (**2007**). "Acoustic backscatter by schools of adult Atlantic mackerel," ICES Journal of Marine Science, **64**, 1145–1151. doi:10.1093/icesjms/fsm094

Graham, A., and Hall, A. J. (**1997**). "The horizontal distribution of bubbles in a shallow sea," Continental Shelf Research, **17**, 1051–1082. doi:10.1016/S0278-4343(97)00006-X

Graham, T. R., Harvey, J. T., Benson, S. R., Renfree, J. S., and Demer, D. A. (**2010**). "The acoustic identification and enumeration of scyphozoan jellyfish, prey for leatherback sea turtles

(Dermochelys coriacea), off central California," ICES Journal of Marine Science, **67**, 1739–1748. doi:10.1093/icesjms/fsq112
Graham, W., Martin, D., and Martin, J. (**2003**). "In situ quantification and analysis of large jellyfish using a novel video profiler," Mar. Ecol. Prog. Ser., **254**, 129–140. doi:10.3354/meps254129
Hansen, R. E. (**2019**). "Mapping the ocean floor in extreme resolution using interferometric synthetic aperture sonar," Proceedings of Meetings on Acoustics, **38**, 055003. doi:10.1121/2.0001058
Harb, C., and Foroutan, H. (**2019**). "A Systematic Analysis of the Salinity Effect on Air Bubbles Evolution: Laboratory Experiments in a Breaking Wave Analog," J. Geophys. Res. Oceans, **124**, 7355–7374. doi:10.1029/2019JC015337
Hinze, J. O. (**1955**). "Fundamentals of the hydrodynamic mechanism of splitting in dispersion processes," AIChE Journal, **1**, 289–295. doi:10.1002/aic.690010303
Hirose, M., Mukai, T., Hwang, D., and Iida, K. (**2005**). "Target strength measurements on tethered live jellyfish Nemopilema nomurai," Bulletin of the Japanese Society of Scientific Fisheries (Japan), **71**, 571–577.
Hirose, M., Mukai, T., Hwang, D., and Iida, K. (**2009**). "The acoustic characteristics of three jellyfish species: Nemopilema nomurai, Cyanea nozakii, and Aurelia aurita," ICES Journal of Marine Science, **66**, 1233–1237. doi:10.1093/icesjms/fsp126
Houghton, J., Doyle, T., Davenport, J., and Hays, G. (**2006**). "Developing a simple, rapid method for identifying and monitoring jellyfish aggregations from the air," Mar. Ecol. Prog. Ser., **314**, 159–170. doi:10.3354/meps314159
Irigoien, X., Klevjer, T. A., Røstad, A., Martinez, U., Boyra, G., Acuña, J. L., Bode, A., et al. (**2014**). "Large mesopelagic fishes biomass and trophic efficiency in the open ocean," Nat Commun, **5**, 3271. doi:10.1038/ncomms4271
Jech, J. M., Horne, J. K., Chu, D., Demer, D. A., Francis, D. T. I., Gorska, N., Jones, B., et al. (**2015**). "Comparisons among ten models of acoustic backscattering used in aquatic ecosystem research," The Journal of the Acoustical Society of America, **138**, 3742–3764. doi:10.1121/1.4937607
Johnson, B. D., and Cooke, R. C. (**1979**). "Bubble populations and spectra in coastal waters: A photographic approach," Journal of Geophysical Research: Oceans, **84**, 3761–3766. doi:10.1029/JC084iC07p03761
Jones, B. A., Lavery, A. C., and Stanton, T. K. (**2009**). "Use of the distorted wave Born approximation to predict scattering by inhomogeneous objects: Application to squid," The Journal of the Acoustical Society of America, **125**, 73–88. doi:10.1121/1.3021298
Kaartvedt, S., Staby, A., and Aksnes, D. L. (**2012**). "Efficient trawl avoidance by mesopelagic fishes causes large underestimation of their biomass," Marine Ecology Progress Series, **456**, 1–6. doi:10.3354/meps09785
Kahn, R. E., and Lavery, A. C. (**2020**). "Broadband scattering from mesopelagic jellyfish," The Journal of the Acoustical Society of America, **148**, 2445–2445. doi:10.1121/1.5146746
Kang, D., Lee, C.-W., Lee, H., and Kim, M.-R. (**2012**). "Sound speed and density ratios inside the body of moon jellyfish (Aurelia aurita s.l.) for hydroacoustic modeling," Ocean and Polar Research, **34**, 85–91. doi:10.4217/OPR.2012.34.1.085
Kang, D., Park, J., Jung, S.-K., and Cho, S. (**2014**). "Estimates of acoustic target strength for giant jellyfish Nemopilema nomurai Kishinouye in the coastal Northwest Pacific," ICES Journal of Marine Science, **71**, 597–603. doi:10.1093/icesjms/fst182
Katz, E. J. (**1969**). "Further study of a front in the Sargasso Sea," Tellus, **21**, 259–269. doi:10.1111/j.2153-3490.1969.tb00437.x
Kilcher, L. F., and Nash, J. D. (**2010**). "Structure and dynamics of the Columbia River tidal plume front," Journal of Geophysical Research: Oceans. doi:10.1029/2009JC006066

Kim, S., Lee, K., Yoon, W. D., Lee, H., and Hwang, K. (**2016a**). "Vertical distribution of giant jellyfish, Nemopilema nomurai using acoustics and optics," Ocean Sci. J., **51**, 59–65. doi:10.1007/s12601-016-0006-z

Kim, S., Lee, K., Yoon, W. D., Lee, H., and Hwang, K. (**2016b**). "Vertical distribution of giant jellyfish, Nemopilema nomurai using acoustics and optics," Ocean Sci. J., **51**, 59–65. doi:10.1007/s12601-016-0006-z

Klevjer, T. A., Irigoien, X., Røstad, A., Fraile-Nuez, E., Benítez-Barrios, V. M., and Kaartvedt., S. (**2016**). "Large scale patterns in vertical distribution and behaviour of mesopelagic scattering layers," Sci Rep, **6**, 19873. doi:10.1038/srep19873

Knauss, J. A. (**1957**). "An Observation of an Oceanic Front," Tellus, **9**, 234–237. doi:10.1111/j.2153-3490.1957.tb01878.x

Kubilius, R., Macaulay, G. J., and Ona, E. (**2020**). "Remote sizing of fish-like targets using broadband acoustics," Fisheries Research, **228**, 105568. doi:10.1016/j.fishres.2020.105568

Lamarre, E. (**1993**). *An experimental study of air entrainment by breaking waves* (Thesis), Massachusetts Institute of Technology. Retrieved from https://dspace.mit.edu/handle/1721.1/12685

Lamarre, E., and Melville, W. K. (**1994**). "Sound-speed measurements near the ocean surface," The Journal of the Acoustical Society of America, **96**, 3605–3616. doi:10.1121/1.410578

Largier, J. L. (**1993**). "Estuarine fronts: How important are they?," Estuaries, **16**, 1–11. doi:10.2307/1352760

Lavery, A. C., Bassett, C., Lawson, G. L., and Jech, J. M. (**2017**). "Exploiting signal processing approaches for broadband echosounders," (D. Demer, Ed.) ICES Journal of Marine Science, **74**, 2262–2275. doi:10.1093/icesjms/fsx155

Lavery, A. C., Chu, D., and Moum, J. N. (**2010**). "Measurements of acoustic scattering from zooplankton and oceanic microstructure using a broadband echosounder," ICES Journal of Marine Science, **67**, 379–394. doi:10.1093/icesjms/fsp242

Lavery, A. C., Stanton, T. K., McGehee, D. E., and Chu, D. (**2002**). "Three-dimensional modeling of acoustic backscattering from fluid-like zooplankton," The Journal of the Acoustical Society of America, **111**, 1197–1210. doi:10.1121/1.1433813

Lavery, A. C., Wiebe, P. H., Stanton, T. K., Lawson, G. L., Benfield, M. C., and Copley, N. (**2007**). "Determining dominant scatterers of sound in mixed zooplankton populations," The Journal of the Acoustical Society of America, **122**, 3304–3326. doi:10.1121/1.2793613

Lawson, G. L., Wiebe, P. H., Stanton, T. K., and Ashjian, C. J. (**2008**). "Euphausiid distribution along the Western Antarctic Peninsula—Part A: Development of robust multi-frequency acoustic techniques to identify euphausiid aggregations and quantify euphausiid size, abundance, and biomass," Deep Sea Research Part II: Topical Studies in Oceanography, Dynamics of Plankton, Krill, and Predators in Relation to Environmental Features of the Western Antarctic Peninsula and Related Areas: SO GLOBEC Part II, **55**, 412–431. doi:10.1016/j.dsr2.2007.11.010

Lee, W.-J., Lavery, A. C., and Stanton, T. K. (**2012**). "Orientation dependence of broadband acoustic backscattering from live squid," The Journal of the Acoustical Society of America, **131**, 4461. doi:10.1121/1.3701876

Lee, Y.-W., and Hwang, B.-K. (**2009**). "Theoretical examination of the effects of fluctuation of acoustic scattering on the swimming behavior of giant jellyfish," Korean Journal of Fisheries and Aquatic Sciences, **42**, 165–170. doi:10.5657/kfas.2009.42.2.165

Leighton, T. G., Meers, S. D., and White, P. R. (**2004**). "Propagation through nonlinear time-dependent bubble clouds and the estimation of bubble populations from measured acoustic characteristics," Proc. R. Soc. Lond. A, **460**, 2521–2550. doi:10.1098/rspa.2004.1298

Lewis, E. R., and Schwartz, S. E. (**2004**). *Sea Salt Aerosol Production: Mechanisms, Methods, Measurements, and Models*, American Geophysical Union, 423 pages.

Liu, H., Yu, J., Wang, T., Yang, Y., Wang, J., and Zheng, R. (**2013**). "Digital holography experiment of 3D detection of underwater bubble fields," Chinese Optics Letters, **11**, S20901. doi: 10.3788/COL201311.S20901

Lubis, M. Z., and Manik, H. M. (**2017**). "Acoustic systems (split beam echo sounder) to determine abundance of fish in marine fisheries:," Journal of Geoscience, Engineering, Environment, and Technology, **2**, 76–83. doi:10.24273/jgeet.2017.2.1.38

Luketina, D. A., and Imberger, J. (**1987**). "Characteristics of a surface buoyant jet," Journal of Geophysical Research: Oceans, **92**, 5435–5447. doi:10.1029/JC092iC05p05435

Lynam, C. P., Gibbons, M. J., Axelsen, B. E., Sparks, C. A., Coetzee, J., Heywood, B. G., and Brierley, A. S. (**2006**). "Jellyfish overtake fish in a heavily fished ecosystem," Current biology, **16**, R492–R493. doi:10.1016/j.cub.2006.09.012

Marmorino, G. O., and Trump, C. L. (**1996**). "High-resolution measurements made across a tidal intrusion front," Journal of Geophysical Research: Oceans, **101**, 25661–25674. doi:10.1029/96JC02384

Marmorino, G. O., and Trump, C. L. (**2000**). "Gravity current structure of the Chesapeake Bay outflow plume," Journal of Geophysical Research: Oceans, **105**, 28847–28861. doi:10.1029/2000JC000225

Marston, T. M., Bassett, C., Plotnick, D. S., Kidwell, A. N., and Honegger, D. A. (**2023**). "Three-dimensional observations of tidal plume fronts in estuaries using a synthetic aperture sonar array," The Journal of the Acoustical Society of America, **154**, 1124–1137. doi:10.1121/10.0020671

Medwin, H. (**1970**). "In situ acoustic measurements of bubble populations in coastal ocean waters," J. Geophys. Res., **75**, 599–611. doi:10.1029/JC075i003p00599

Medwin, H. (**1977**). "Acoustical determinations of bubble-size spectra," J. Acoust. Soc. Am., **62**, 5. doi:10.1121/1.381617

Medwin, H., and Breitz, N. D. (**1989**). "Ambient and transient bubble spectral densities in quiescent seas and under spilling breakers," Journal of Geophysical Research: Oceans, **94**, 12751–12759. doi:10.1029/JC094iC09p12751

Medwin, H., and Clay, C. S. (**1998**). *Fundamentals of acoustical oceanography*, Applications of modern acoustics, Academic Press, Boston, 712 pages.

Mills, C. E. (**2001**). "Jellyfish blooms: are populations increasing globally in response to changing ocean conditions?," Hydrobiologia, **451**, 55–68. doi:10.1023/A:1011888006302

Misund, O. A., Aglen, A., and Frønæs, E. (**1995**). "Mapping the shape, size, and density of fish schools by echo integration and a high-resolution sonar," ICES Journal of Marine Science, **52**, 11–20. doi:10.1016/1054-3139(95)80011-5

Monger, B. C., Chinniah-Chandy, S., Meir, E., Billings, S., Greene, C. H., and Wiebe, P. H. (**1998**). "Sound scattering by the gelatinous zooplankters Aequorea victoria and Pleurobrachia bachei," Deep Sea Research Part II: Topical Studies in Oceanography, **45**, 1255–1271. doi:10.1016/S0967-0645(98)00029-0

Morse, P. M., and Ingard, K. U. (**1986**). *Theoretical Acoustics*, Princeton University Press, 954 pages.

Mutlu, E. (**1996**). "Target strength of the common jellyfish (Aurelia aurita): a preliminary experimental study with a dual-beam acoustic system," ICES Journal of Marine Science, **53**, 309–311. doi:10.1006/jmsc.1996.0040

Nash, J. D., and Moum, J. N. (**2005**). "River plumes as a source of large-amplitude internal waves in the coastal ocean," Nature, **437**, 400–403. doi:10.1038/nature03936

Nesse, T. L., Hobæk, H., and Korneliussen, R. J. (**2009**). "Measurements of acoustic-scattering spectra from the whole and parts of Atlantic mackerel," ICES Journal of Marine Science, **66**, 1169–1175. doi:10.1093/icesjms/fsp087

O'Donnell, J., Marmorino, G. O., and Trump, C. L. (**1998**). "Convergence and Downwelling at a River Plume Front," Journal of Physical Oceanography, **28**, 1481–1495. doi:10.1175/1520-0485(1998)028<1481:CADAAR>2.0.CO;2

O'Hern, T. J., d'Agostino, L., and Acosta, A. J. (**1988**). "Comparison of Holographic and Coulter Counter Measurements of Cavitation Nuclei in the Ocean," Journal of Fluids Engineering, **110**, 200–207. doi:10.1115/1.3243535

Pakhomov, E., and Yamamura, O. (**2021**). "Report of the advisory panel on micronekton sampling inter-calibration experiment.," Retrieved from https://www.proquest.com/openview/68db22a52f0dd2936e24e98cd4256a2e/1?pq-origsite=gscholar&cbl=666304

Pauly, D., Graham, W., Libralato, S., Morissette, L., and Deng Palomares, M. L. (**2009**). "Jellyfish in ecosystems, online databases, and ecosystem models," Hydrobiologia, **616**, 67–85. doi:10.1007/s10750-008-9583-x

Pitt, K. A., Lucas, C. H., Condon, R. H., Duarte, C. M., and Stewart-Koster, B. (**2018**). "Claims That Anthropogenic Stressors Facilitate Jellyfish Blooms Have Been Amplified Beyond the Available Evidence: A Systematic Review," Frontiers in Marine Science. doi:10.3389/fmars.2018.00451

Preisig, J. (**2007**). "Acoustic propagation considerations for underwater acoustic communications network development," SIGMOBILE Mob. Comput. Commun. Rev., **11**, 2–10. doi:10.1145/1347364.1347370

Preisig, J. C., and Deane, G. B. (**2004**). "Surface wave focusing and acoustic communications in the surf zone," The Journal of the Acoustical Society of America, **116**, 2067–2080. doi:10.1121/1.1771591

Proud, R., Handegard, N. O., Kloser, R. J., Cox, M. J., and Brierley, A. S. (**2019**). "From siphonophores to deep scattering layers: uncertainty ranges for the estimation of global mesopelagic fish biomass," (D. Demer, Ed.) ICES Journal of Marine Science, **76**, 718–733. doi:10.1093/icesjms/fsy037

Reeder, D. B., Joseph, J. E., Rago, T. A., Bullard, J. M., Honegger, D., and Haller, M. C. (**2022**). "Acoustic spectrometry of bubbles in an estuarine front: Sound speed dispersion, void fraction, and bubble density," The Journal of the Acoustical Society of America, **151**, 2429–2443. doi:10.1121/10.0009923

Richardson, A. J., Bakun, A., Hays, G. C., and Gibbons, M. J. (**2009**). "The jellyfish joyride: causes, consequences and management responses to a more gelatinous future," Trends in Ecology & Evolution, **24**, 312–322. doi:10.1016/j.tree.2009.01.010

Rojas, G., and Loewen, M. R. (**2007**). "Fiber-optic probe measurements of void fraction and bubble size distributions beneath breaking waves," Exp Fluids, **43**, 895–906. doi:10.1007/s00348-007-0356-5

Sarabun, C. C. (**1993**). "Observations of a Chesapeake Bay tidal front," Estuaries, **16**, 68–73. doi:10.2307/1352764

Scully, M. E., Fisher, A. W., Suttles, S. E., Sanford, L. P., and Boicourt, W. C. (**2015**). "Characterization and Modulation of Langmuir Circulation in Chesapeake Bay," Journal of Physical Oceanography, **45**, 2621–2639. doi:10.1175/JPO-D-14-0239.1

Shao, S. (**2019**). "A hybrid image processing method for measuring 3D bubble distribution using digital inline holography," Chemical Engineering Science. doi:10.1016/j.ces.2019.07.009

Shin, H.-H., Han, I., Oh, W., Chae, J., Yoon, E., and Lee, K. (**2019**). "Estimation of Moon Jellyfish Aurelia coerulea Using Hydroacoustic Methods off the Coast of Tongyeong, Korea," Korean Journal of Fisheries and Aquatic Sciences, **52**, 725–734. doi:10.5657/KFAS.2019.0725

Shrestha, K., Anderson, W., and Kuehl, J. (**2018**). "Langmuir Turbulence in Coastal Zones: Structure and Length Scales," Journal of Physical Oceanography, **48**, 1089–1115. doi:10.1175/JPO-D-17-0067.1

Stanton, T. (**1996**). "Acoustic scattering characteristics of several zooplankton groups," ICES Journal of Marine Science, **53**, 289–295. doi:10.1006/jmsc.1996.0037

Stanton, T. (**2000**). “Review and recommendations for the modelling of acoustic scattering by fluid-like elongated zooplankton: euphausiids and copepods,” ICES Journal of Marine Science, **57**, 793–807. doi:10.1006/jmsc.1999.0517

Stanton, T. K., and Chu, D. (**2000**). “Review and recommendations for the modelling of acoustic scattering by fluid-like elongated zooplankton: euphausiids and copepods,” ICES Journal of Marine Science, **57**, 793–807. doi:10.1006/jmsc.1999.0517

Stanton, T. K., and Chu, D. (**2004**). “On the acoustic diffraction by the edges of benthic shells,” The Journal of the Acoustical Society of America, **116**, 239–244. doi:10.1121/1.1675813

Stanton, T. K., Chu, D., and Wiebe, P. H. (**1998**). “Sound scattering by several zooplankton groups. II. Scattering models,” The Journal of the Acoustical Society of America, **103**, 236–253. doi:10.1121/1.421110

Stanton, T. K., Clay, C. S., and Chu, D. (**1993**). “Ray representation of sound scattering by weakly scattering deformed fluid cylinders: Simple physics and application to zooplankton,” The Journal of the Acoustical Society of America, **94**, 3454–3462. doi:10.1121/1.407199

Stanton, T. K., Reeder, D. B., and Jech, J. M. (**2003**). “Inferring fish orientation from broadband-acoustic echoes,” ICES Journal of Marine Science, **60**, 524–531. doi:10.1016/S1054-3139(03)00032-8

Stanton, T. K., Sellers, C. J., and Jech, J. M. (**2012**). “Resonance classification of mixed assemblages of fish with swimbladders using a modified commercial broadband acoustic echosounder at 1–6 kHz,” Can. J. Fish. Aquat. Sci., **69**, 854–868. doi:10.1139/f2012-013

Stanton, T. K., Wiebe, P. H., Chu, D., Benfield, M. C., Scanlon, L., Martin, L., and Eastwood, R. L. (**1994**). “On acoustic estimates of zooplankton biomass,” ICES Journal of Marine Science, **51**, 505–512. doi:10.1006/jmsc.1994.1051

Steffen, E. L., and D’Asaro, E. A. (**2002**). “Deep Convection in the Labrador Sea as Observed by Lagrangian Floats,” Journal of Physical Oceanography, **32**, 475–492. doi:10.1175/1520-0485(2002)032<0475:DCITLS>2.0.CO;2

Sthapit, P., Kim, M., Kang, D., and Kim, K. (**2020**). “Development of Scientific Fishery Biomass Estimator: System Design and Prototyping,” Sensors, **20**, 6095. doi:10.3390/s20216095

Talapatra, S., Sullivan, J., Katz, J., Twardowski, M., Czerski, H., Donaghay, P., Hong, J., et al. (**2012**). “Application of in-situ digital holography in the study of particles, organisms and bubbles within their natural environment,” Proceedings of SPIE - The International Society for Optical Engineering, **8372**, 4. doi:10.1117/12.920570

Terrill, E. J., and Melville, W. K. (**2000**). “A Broadband Acoustic Technique for Measuring Bubble Size Distributions: Laboratory and Shallow Water Measurements,” Journal of Atmospheric and Oceanic Technology, **17**, 220–239. doi:10.1175/1520-0426(2000)017<0220:ABATFM>2.0.CO;2

Terrill, E. J., Melville, W. K., and Stramski, D. (**2001**). “Bubble entrainment by breaking waves and their influence on optical scattering in the upper ocean,” Journal of Geophysical Research: Oceans, **106**, 16815–16823. doi:10.1029/2000JC000496

Thomson, J., Horner-Devine, A. R., Zippel, S., Rusch, C., and Geyer, W. (**2014**). “Wave breaking turbulence at the offshore front of the Columbia River Plume,” Geophysical Research Letters, **41**, 8987–8993. doi:10.1002/2014GL062274

Thorpe, S. A. (**1984**). “The effect of Langmuir circulation on the distribution of submerged bubbles caused by breaking wind waves,” Journal of Fluid Mechanics, **142**, 151–170. doi:10.1017/S0022112084001038

Thorpe, S. A. (**1992**). “Bubble clouds and the dynamics of the upper ocean,” Quarterly Journal of the Royal Meteorological Society, **118**, 1–22. doi:10.1002/qj.49711850302

Thorpe, S. A., Bowyer, P., and Woolf, D. K. (**1992**). “Some Factors Affecting the Size Distributions of Oceanic Bubbles,” Journal of Physical Oceanography, **22**, 382–389. doi:10.1175/1520-0485(1992)022<0382:SFATSD>2.0.CO;2

Thorpe, S. A., and Deacon (**1982**). "On the clouds of bubbles formed by breaking wind-waves in deep water, and their role in air-sea gas transfer," Philosophical Transactions of the Royal Society of London. Series A, Mathematical and Physical Sciences, **304**, 155–210. doi:10.1098/rsta.1982.0011

Tian, L., Loomis, N., Domínguez-Caballero, J. A., and Barbastathis, G. (**2010**). "Quantitative measurement of size and three-dimensional position of fast-moving bubbles in air–water mixture flows using digital holography," Optical Society of America, **49**, 1549–1554.

Ting, F. C. K., and Kirby, J. T. (**1995**). "Dynamics of surf-zone turbulence in a strong plunging breaker," Coastal Engineering, **24**, 177–204. doi:10.1016/0378-3839(94)00036-W

Trevorrow, M. V. (**2003**). "Measurements of near-surface bubble plumes in the open ocean with implications for high-frequency sonar performance," J. Acoust. Soc. Am., **114**, 2672. doi:10.1121/1.1621008

Ullah, I., Baloch, M. K., Niaz, S., Sultan, A., and Ullah, I. (**2019**). "Solubilizing Potential of Ionic, Zwitterionic and Nonionic Surfactants Towards Water Insoluble Drug Flurbiprofen," J Solution Chem, **48**, 1603–1616. doi:10.1007/s10953-019-00938-3

Urick, R. J. (**1983**). *Principles of underwater sound*, McGraw-Hill Book Co.

Vagle, S., and Farmer, D. (**1992**). "The Measurement of Bubble Size Distributions by Acoustic Backscatter," Journal of Atmospheric and Oceanic Technology, **9**, 630–644. doi:10.1175/1520-0426(1992)009<0630:TMOBSD>2.0.CO;2

Vagle, S., and Farmer, D. M. (**1998a**). "A comparison of four methods for bubble size and void fraction measurements," IEEE Journal of Oceanic Engineering, **23**, 211–222. Presented at the IEEE Journal of Oceanic Engineering. doi:10.1109/48.701193

Vagle, S., and Farmer, D. M. (**1998b**). "A comparison of four methods for bubble size and void fraction measurements," IEEE Journal of Oceanic Engineering, **23**, 211–222. Presented at the IEEE Journal of Oceanic Engineering. doi:10.1109/48.701193

Vagle, S., Foote, K. G., Trevorrow, M. V., and Farmer, D. M. (**1996**). "A technique for calibration of monostatic echosounder systems," IEEE Journal of Oceanic Engineering, **21**, 298–305. Presented at the IEEE Journal of Oceanic Engineering. doi:10.1109/48.508160

Vasile, G., d'Urso, G., Goarant, A., de Oliveira, E., and Lungu, E. (**2016**). "Potential of active ultrasound monitoring systems for jellyfish detection." Presented at the OCEANS 2016 MTS/IEEE Monterey. doi:10.1109/OCEANS.2016.7761078

Warren, J. D., and Smith, J. N. (**2007**). "Density and sound speed of two gelatinous zooplankton: ctenophore (Mnemiopsis leidyi) and lion's mane jellyfish (Cyanea capillata)," The Journal of the Acoustical Society of America, **122**, 574–580. doi:10.1121/1.2739433

Winkel, E. S., Ceccio, S. L., Dowling, D. R., and Perlin, M. (**2004**). "Bubble-size distributions produced by wall injection of air into flowing freshwater, saltwater and surfactant solutions," Exp Fluids, **37**, 802–810. doi:10.1007/s00348-004-0850-y

Wright, L. D., and Coleman, J. M. (**1971**). "Effluent expansion and interfacial mixing in the presence of a Salt Wedge, Mississippi River Delta," Journal of Geophysical Research (1896-1977), **76**, 8649–8661. doi:10.1029/JC076i036p08649

Yoon, E. A., Hwang, D. J., Hirose, M., Kim, E. H., Mukal, T., and Park, B. S. (**2010**). "Characteristics of Acoustic Scattering according to Pulsation of the Large Jellyfish Nemopilema nomurai," Korean Journal of Fisheries and Aquatic Sciences, **43**, 551–556. doi:10.5657/KFAS.2010.43.5.551

Yoon, E., Hwang, D., Miyuki, H., Sawada, K., Fukuda, Y., and Mukai, T. (**2015**). "Ex situ acoustic target strength by tilt angle and pulsation of moon jellyfish (Aurelia aurita) using frequency 70 kHz," J. Korean Soc. Fish. Technol., **51**, 295–301. doi:10.3796/KSFT.2015.51.3.295

Yoon, E.-A., Hwang, D.-J., Shin, H.-H., Gwa, D.-S., and Cha, C.-P. (**2012**). “In situ acoustic characteristics of the large jellyfish Nemopilema nomurai in the East China Sea,” Journal of the Korean Society of Fisheries and Ocean Technology, **48**, 256–268. doi:10.3796/KSFT.2012.48.3.256

Yoon, E.-A., Lee, K., Chae, J., Yoon, W., Han, C., Lee, H., Kim, P., et al. (**2019**). “Density Estimates of Moon Jellyfish (Aurelia coerulea) in the Yeongsan Estuary using Nets and Hydroacoustics,” Ocean Sci. J., **54**, 457–465. doi:10.1007/s12601-019-0022-x

Zedel, L., and Farmer, D. (**1991**). “Organized structures in subsurface bubble clouds: Langmuir circulation in the open ocean,” Journal of Geophysical Research: Oceans, **96**, 8889–8900. doi:10.1029/91JC00189

Zi, W., Yong, T., Yuanyuan, F., Wei, M., Shuai, W., and Xiaolin, L. (**2020**). “Monitoring of biomass at Cooling Water System of hongyanhe nuclear power plant by using acoustic methods,” (R. Weerasinghe, J. Wu, and C.-H. Weng, Eds.) E3S Web Conf., **194**, 01007. doi:10.1051/e3sconf/202019401007

Zikanov, O., Slinn, D. N., and Dhanak, M. R. (**2002**). “Turbulent convection driven by surface cooling in shallow water,” Journal of Fluid Mechanics, **464**, 81–111. doi:10.1017/S0022112002001015